Microfluidic tools for single-cell protein analysis

by

Kevin A Yamauchi

A dissertation submitted in partial satisfaction of the

requirements for the degree of

Joint Doctor of Philosophy
with University of California, San Francisco

in

Bioengineering

in the

Graduate Division

of the

University of California, Berkeley

Committee in charge:

Professor Amy E. Herr, Chair
Professor Todd McDevitt
Professor Ming Wu

Spring 2017

Microfluidic tools for single-cell protein analysis

Abstract

Microfluidic tools for single-cell protein analysis

by

Kevin A Yamauchi

Joint Doctor of Philosophy
with University of California, San Francisco in Bioengineering

University of California, Berkeley

Professor Amy E. Herr, Chair

Selective measurement of proteins from single cells is an important and challenging task in the study of cell biology. Protein signaling underlies many important cellular processes such as stem cell differentiation and tumor metastasis. However, due to the diversity of proteins and the subtlety of the chemical modifications that transduce the signals, it is challenging to selectively measure a specific protein from single cells. Further, determining the localization of proteins in individual cells is challenging due to the artifacts introduced by the chemical fixation required by current tools. To address each of these analytical gaps, we introduce two new single cell protein analysis platforms and two supporting technologies.

First, to eliminate fixation-induced artifacts in single-cell protein localization measurements, we developed the subcellular western blotting platform. We designed a set of buffers that enabled independent separations of the cytoplasmic and nuclear compartments of the same single cell. To enable buffer exchange without disturbing the intact cellular components, we developed a hydrogel-based lid for the delivery of lysis reagents purely by diffusion. We characterized the selectivity of the fractionation by assaying a panel of proteins with known localization and demonstrated the platform with an NF-κB translocation assay.

Next, to enhance the selectivity of single-cell protein analysis, introduced an assay for performing single-cell isoelectric focusing. Building upon the hydrogel lid based reagent delivery system, we developed a microfluidic device that integrates sample preparation, analyte separation, and detection. We characterized the theoretical performance of the device using a fluorescent ladder and purified proteins. Further, we used the single-cell isoelectric focusing assay to separate isoforms and TurboGFP and β-tubulin from single cells. Additionally, we extended the platform by designing a lid system that generates a rectangular array of pH gradients, increasing the potential throughput of the single-cell isoelectric focusing assay.

To enable the rapid analysis of arrayed microscale separation data, we developed a suite of image processing scripts. We wrote the scripts in a modular manner both reducing complexity and enabling facile development of new functionality. We user-tested the scripts with life science researchers with backgrounds ranging from statistics to biology. From the

user feedback, we identified the quality control step to be the most susceptible to user-to-user variance. Thus, on-going work aims to develop algorithms to automate the quality control process.

Finally, we report a method to prototype microscale separation devices. Polydimethylsiloxane is a common material used for rapid prototyping of microfludic devices. However, because it is oxygen permeable, it is not suitable for polyacrylamide gel electrophoresis since oxygen inhibits free radical polymerization. Thus, we developed a method to prevent oxygen inhibition and thus enable polymerization of polyacrylamide in PDMS microchannels. We characterized the separation performance of the resulting polyacrylamide hydrogels and demonstrated separation in reversibly sealed devices.

In summary, in this dissertation, we used our understanding of mass transport and microfabrication to design new platforms for selective single-cell protein analysis measurement. Future innovation may extend the sensitivity and multiplexing of these tools to enable highly specific measurement of all the key proteins in entire cellular signaling pathways.

To my family.

Contents

List of Figures

List of Tables

Acknowledgments

I have been fortunate to be surrounded by an extremely supportive community my whole life. My parents, Sandie and Dennis, my grandfather, my aunties and uncles, and my cousins have provided me with a nurturing environment to grow and (slowly) mature. Irrespective of what life had in store for us, I was always well-fed and cared for and my education always came first. I do not have any brothers by blood, but I have grown up with two outstanding men: Kevin and Erik. Our conversations under the stars have played a key role in shaping my view of the world. I am also grateful for Nicole, a more recent, but very important part of my life. Throughout our relationship, she has brought much-needed balance and compassion. I am forever grateful for the love and support of my family.

Before attending graduate school was a possibility I had even considered, Prof. Steve Klisch, Prof. Bob Sah, and Prof. Scott Hazelwood introduced me to the excitement of engineering research. I am grateful to them for taking a chance on me and for their patience as I discovered how challenging and intellectually rewarding research can be. Through their mentorship, I developed what I think will be a lifelong passion for research.

Prof. Amy Herr leads by example in fostering a rigorous and inclusive scientific community. I am thankful for how tirelessly she works to ensure that we have the intellectual, infrastructural, and financial resources to perform the best research we can. I am also grateful for the trust she has placed in me as a young researcher in her laboratory. Amy's continuous support has been a catalyst in my growth as an engineer.

My friends and colleagues in the Herr Lab are amongst the sharpest and most caring people I have worked with. I am grateful for the support I received when the going was tough and for the great memories from times of celebration. In particular, I would like to thank Julea, Augusto, and Ginny for the thought-provoking discussions and for pushing me to be an upstanding member of the scientific community. There were many moments of doubt during graduate school, but I never doubted my decision to join the Herr Lab.

I would also like to thank the members of my qualifying exam and dissertation committees: Prof. Dan Fletcher, Prof. Zev Gartner, Prof. Ming Wu, and Prof. Todd McDevitt. Their input and guidance was very helpful as I shaped my dissertation.

Finally, I would like to thank the organizations that financially supported our research. The National Science Foundation, the National Institutes of Health, the Siebel Foundation, the UC Berkeley Graduate division, and the Lloyd family. Without their financial support, the research we performed would not have been possible.

Chapter 1

Introduction

1.1 Motivation for single-cell protein analysis

Proteins are an important and dynamic signaling molecule in cells. Proteins are responsible for transducing intra- and extra-cellular signals and thus underlie many diseases. For example, isoforms of β-tubulin, a cytoskeletal protein have been implicated to resistance to chemotherapeutics in cancer. [1] Further, the expression of specific transcription factors have been shown to play a central role in returning differentiated cells to a pluripotent state. [2, 3] While central dogma suggests we can predict protein expression from RNA or DNA level data, recent work has shown a poor correlation between some protein and mRNA targets, potentially due to variability protein translation and degradation rates. [4–6] Moreover, important signaling events such as post-translational modifications are not represented in the transcriptome or genome. [7] Thus, directly measuring proteins is essential to understanding the role they play in cell biology.

Due to the complexity and diversity of the proteome, it is difficult to selectively measure proteins. [7, 8] Through events such as alternative splicing a single gene may be transcribed into several different mRNA, giving rise to related proteins known as isoforms. [7, 9] Further, once the mRNA are translated to proteins, they may be further modified through post-translational modifications, which are small chemical groups (e.g. phosphate or methyl groups) that have can marked effects on the proteins function (Figure 1.1). [7, 10, 11] In a remarkable, but specific example, a single phosphorylation ($\sim 0.5\%$ change in molecular mass) is a key step in the NF-κ pathway, which is involved in many important processes including inflammation and tumor metastasis. [12, 13] Since each final protein, or so-called proteoform has a distinct activity it is necessary to selectively measure specific proteoforms.
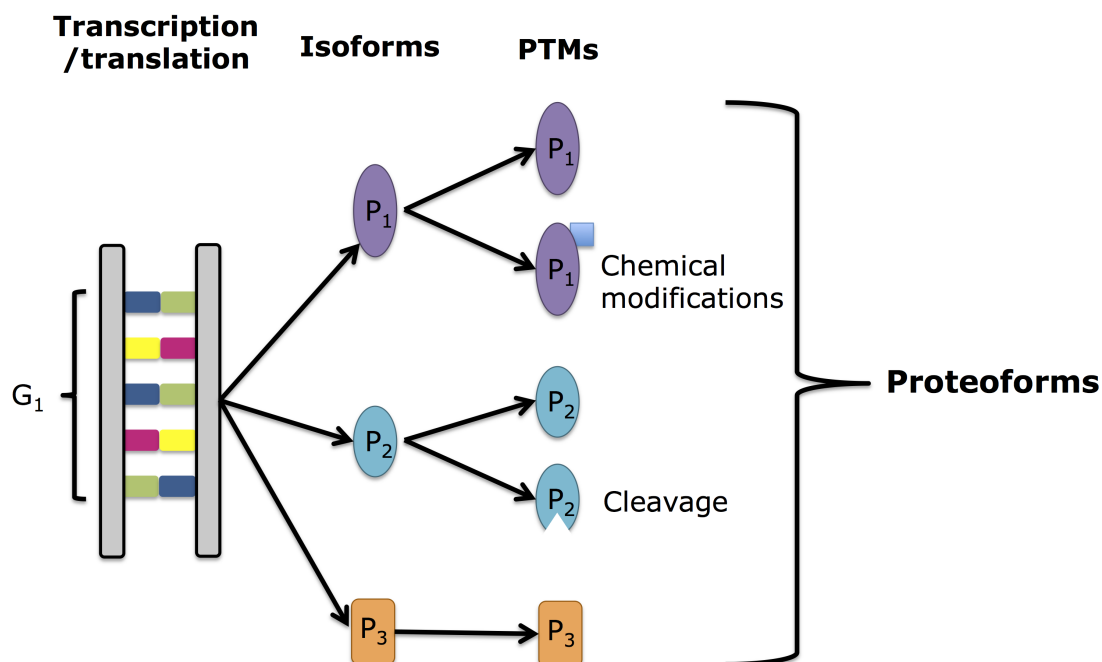
Figure 1.1: A diverse array of proteoforms can be produced by a single gene. First, multiple isoforms can be transcribed from a specific gene. Once the proteins are translated from the mRNA each one may receive a post-translation modification such as a phosphorylation or proteolytic cleavage. Each specific endpoint protein is referred to as a proteoform.

In addition to abundance, the localization of a protein can have a marked impact on its function. In a canonical example, a transcription factor NF-κB is inactive when in the cytoplasm of the cell. However, upon activation, NF-κB translocates to the nucleus of the cell where it binds to the DNA, instigating broad changes in transcription. NF-κB signaling is involved in many important processes such as immune response, cancer metastasis, and inflammation. [12–14] Determining protein localization provides important context to protein abundance measurements.

Single-cell protein measurements are essential to understanding the molecular underpinning of important biological phenomena such as cancer metastasis and stem cell differentiation. Deeper understanding of the composition and dynamics of the proteome will further our understanding of the inner workings of cells. Owing to the diversity of the protein state and intercellular heterogeneity, there is a need for tools capable of selectively measuring protein abundance and localization in single cells.

1.2 Measurement gap: the need for high selectivity single-cell protein analysis tools

Single-cell protein analysis tools play a critical role in understanding the molecular basis for disease and other biological phenomena. Due to the cell-to-cell variability, it is important to assay individual cells, as bulk measurements mask the intercellular heterogeneity. Further, the tools must be highly selective in order to measure specific proteoforms in spite of how subtle the chemical modifications can be that differentiate them. While challenging to design, single-cell analysis tools have played an essential role in understanding intracellular protein signaling.

Mass spectrometry is a powerful, commonly-used tool for proteomics. In shotgun or bottom-up mass spectrometry, the proteins in a complex mixture (e.g. cell lysate) are digested into small peptide fragments. [15] Doing so enables the identification of thousands of different proteins and post-translational modifications in a single sample. [16] However, since each initial protein is fragmented into many peptides, it is difficult to determine how the modified peptides map back to intact proteins and thus quantify the abundance of specific proteoforms. [17] To measure specific proteoforms, top-down mass spectrometry uses an upstream separation to simplifiy the complex mixture and then analyzes intact proteins. By analyzing intact proteins, top-down mass spectrometry can quantify abundances of specific proteoforms. [17] While powerful and quantitative, mass spectrometry currently lacks the sensitivity for single-cell analysis. [18]

Immunoassays are the workhorse tool for measuring proteins. Immunoassays detect proteins through the binding of antibodies to their target antigen. Using different labeling strategies ranging from fluorescence to mass, immunoassays can achieve a high degree of multiplexing (5+ targets for immunocytochemistry [19], 37 targets for mass cytometry [20, 21]). Impressively, using super resolution microscopy, immunocytochemistry can localize proteins in a mammalian cell with 20-30 nm resolution. [22] However, the selectivity of immunoassays is fundamentally limited by the specificity of antibodies and fixation artifacts. The specificity of antibodies is limited due to the high degree of similarity between proteoforms (e.g. NF-κB phosphorylation is a ¡1% change in mass). [23, 24] Further, the chemical fixation required to assay intracellular proteins results in abberant localization due to distortion of the cellular structures and non-uniformity in fixation timescales across the cell. [23, 25, 26]

Electrophoretic separations have been used upstream of immunoassays to enhance the specificity of immunoassays. Size based separations, commonly known as western blots, use a size-based electrophoretic separation followed by an immunoblot to report both a proteins size (molecular mass) and immunoaffinity. [27] The size-based separation enables the identification of isoforms of different size using a non-isoform-specific antibody. Isoelectric focusing, another prominent separation mode, has also been used upstream of immunoblots. Instead of separating analytes by size, isoelectric focusing separates analytes by their isoelectric point (i.e. the pH at which they have no net charge). [28] Thus, isoelectric focusing

is very sensitive to chemical modifications and has been used to selectively measure proteins with different post-translational modifications. [28, 29] Unfortunately, traditional bench-top separation methods are not sensitive enough for single-cell analysis and only report heterogeneity-masking bulk measurements. [29]

Microscale separation tools have enabled the analysis of proteins from unfixed individual cells. First demonstrated in microcapillaries, proteins from single cells were separated via an electrophoretic separation. [30, 31] More recently, the Herr Lab has leveraged favorable scaling to demonstrate western blotting of single cells. However, thus far, this has only been demonstrated for whole cells and has only separated proteins with a molecular mass difference of 28% and thus cannot resolve many important proteoforms (e.g. post-translational modification) and cannot report the localization of proteins. [32–34]

To understand how cells use translocation and chemical modifications of their proteome to transduce signals, there is a need for new tools capable of selectively measuring specific proteoforms and protein localization without chemical fixation.

1.3 Dissertation overview

In this dissertation, we report the development of two platforms for enhanced selectivity single-cell protein measurements and two supporting technologies. We sought to address two key limitations of current single-cell protein analysis tools: (1) fixation artifacts when measuring protein localization and (2) selectivity limited by antibody specificity (Figure 1.2).
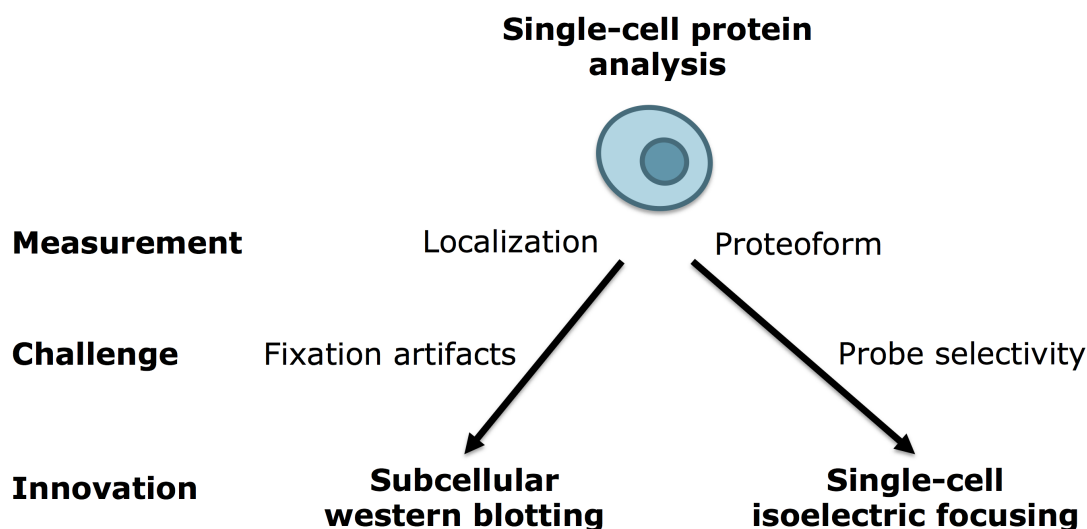
Figure 1.2: Dissertation overview. We sought to develop tools to improve single-cell protein analysis by eliminating fixation artifacts in protein localization and enhancing the selectivity of single-cell protein analysis.

In chapter 2, we present the design and characterization of an assay for measuring protein localization and expression in single cells without fixation-induced artifacts. To enable sub-cellular fractionation of single cells, we designed cytoplasm- and nucleus-specific lysis buffers that are compatible with electrophoresis. Further, we developed a method to exchange buffers without displacing the un-lysed organells (i.e. the nucleus) from the microwells. We characterized the selectivity of the fractionation with a panel of proteins with known localization and demonstrated the measurement on a dynamic system with a model NF-κB translocation assay.

In chapter 3, we enhance the selectivity of single-cell protein analysis with an isoelectric focusing assay capable of resolving single-charge difference isoforms from individual cells. Building upon the lid-based reagent delivery system developed in the $(sc)^2$WB, we designed a chemically patterned lid that enabled the integration of sample preparation and analyte separation. From simulation results, we hypothesize the primary mechanism for reducing protein losses during separation is the restorative electrophoresis and not the inclusion of the lid. We demonstrated both native and denatured separation of protein form individual cells. In denaturing conditions we achieve separation of two isoforms of endogenous β-tubulin and resolution of the three single charge difference isoforms of TurboGFP. In chapter 4, we extend the ability of the scIEF to generate gradient slopes and back-to-back pH gradients. Fine control over the gradient geometry allows for tuning of assay performance for separation resolution or throughput.

To support the analysis of arrayed separation data, we share the development of analysis scripts for processing images of arrayed separations in chapter 5. We defined a data structure to store the separation data in a standardized and easily-accessible way. Additionally, we discretized the task of analyzing the separations into modular functions that can easily be expanded upon or adapted to variations on the assay. Finally, we tested the script with users from varying life science research backgrounds.

In chapter 6, we detail a method for prototyping channel geometries for microscale electrophoresis. While PDMS is a commonly used material for prototyping microfluidic devices, it is less often used for devices requiring radical polymerization because PDMS is permeable to oxygen. To prevent oxygen from inhibiting the polymerization of polyacrylamide in PDMS microchannels, we developed a protocol for incorporating benzophenone into the walls of the PDMS. We characerized the separation performance of the resulting polyacrylamide channels and also demonstrated electrophoresis in a reversibly-sealed device. The ability to fabricate microscale gel electrophoresis devices in PDMS reduces the fabrication time from days to hours (as compared to traditional glass devices) and also enables integration with other PDMS-based microfluidic devices.

Finally, in chapter 7 we summarize the work and suggest directions for future work. The appendix includes protocols for the methods described in this dissertation.

1.4   Electrophoretic Separations

The work described in this dissertation leverages electrophoretic separations based on either size or isoelectric point to selectively assay specific proteoforms. Thus, the following section presents the underlying theory used to predict and quantify the types of electrophoretic separations used in this work.

Electrical double layer

First, we consider a charged planar surface in an electrolyte solution (Figure 1.3). Many of the devices used in microfluidics are made of PDMS or glass, which has a slight negative surface charge in aqueous solution. [35, 36] While the bulk of the solution (i.e. far from the charge surface) is a homogenous mixture of the various ion species, there is an accumulation of counter-ions (i.e. ions with an opposite charge of the surface). This region where the counter-ions have accumulated is known as the electrical double layer (EDL).
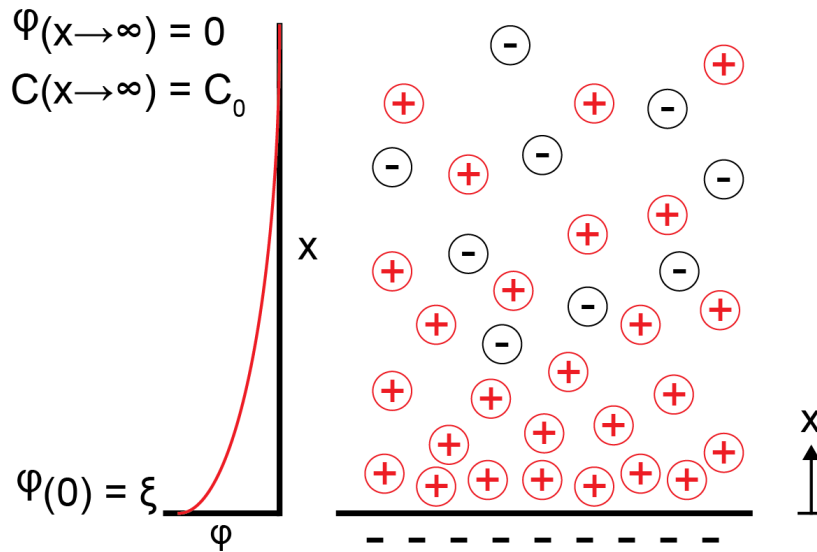
Figure 1.3: Formation of the electrical double layer over a charged plate. There is an accumulation of positive counter-ions near the surface of the negatively charged plate. The potential at the surface is $\phi(0) = \zeta$ and the potential in the bulk is $\phi(x \to \infty) = 0$.

Using symmetry, we can simplify our charged plate to a 1D system as shown in Figure 1.3. Further, we will assume the solutes do not interact with one another (i.e. the solution is "infinitely dilute"). We apply boundary conditions such that the potential at the surface is $\phi(0) = \zeta$ and the potential in the bulk is $\phi(x \to \infty) = 0$. Finally, the concentration in

the bulk is $C(x \to \infty) = C_0$. Using Boltzman statistics, we can write the concentration of species i as a function of the local potential ϕ as

$$c_i = c_i(x \to \infty) \exp\left(-\frac{z_i F \phi}{RT}\right) \tag{1.1}$$

where z_i is the valency of the ion, F is Faraday's constant, R is the universal gas constant and T is temperature. The charge density ρ_e is defined as

$$\rho_e = \sum_n c_i z_i F \tag{1.2}$$

Substituting equation 1.1 into equation 1.2 gives

$$\rho_e = \sum_n c_i(x \to \infty) z_i F \exp\left(-\frac{z_i F \phi}{RT}\right) \tag{1.3}$$

For a uniform permitivity ϵ, the Poission equation relates potential and local charge density as

$$\nabla^2 \phi = -\frac{\rho_e}{\epsilon} \tag{1.4}$$

We can derive the Poisson-Boltzman equation by substituting equation 1.3 into equation 1.4

$$\nabla^2 \phi = -\frac{F}{\epsilon} \sum_n c_i(x \to \infty) z_i F \exp\left(-\frac{z_i F \phi}{RT}\right) \tag{1.5}$$

Recalling that we have used symmetry to reduce the system to 1D and considering a simple solution with a pair of symmetric ionic species (i.e. $z_1 = -z_2 = z$, $c_1(x \to \infty) = c_2(x \to \infty) = C_0$), we can reduce equation 1.5 to

$$\frac{\partial^2 \phi}{\partial x^2} = \frac{F|z|}{\epsilon} C_0 \left[\exp\left(-\frac{|z| F \phi}{RT}\right) - \exp\left(\frac{|z| F \phi}{RT}\right)\right] \tag{1.6}$$

which can be rewritten as

$$\frac{\partial^2 \phi}{\partial x^2} = \frac{2 F|z| C_0}{\epsilon} sinh\left(\frac{|z| F \phi}{RT}\right) \tag{1.7}$$

For small surface charges where $\frac{|z| F \phi}{RT} \ll 1$, we can approximate the $sinh$ with the first order Taylor series expansion (the Debye-Huckel linear approximination) as

$$\frac{\partial^2 \phi}{\partial x^2} = \frac{2 F^2 |z|^2 C_0}{\epsilon RT} \phi \tag{1.8}$$

Integrating and applying the boundary conditions gives

$$\phi\left(x\right) = \zeta \exp\left(-\frac{2\,F^2\,|z|^2\,C_0}{\epsilon RT}x\right) \tag{1.9}$$

From this solution, we can group terms and define the characteristic length scale of the EDL or the Debye length λ_d as

$$\lambda_d = \left(\frac{\epsilon RT}{2\,F^2\,|z|^2\,C_0}\right)^2 \tag{1.10}$$

Electrophoresis

In this next section, we will introduce electrophoresis, the migration of charged particles in an applied electric field. First we will consider a charged sphere with radius a in a uniform electric field. Since the control volume should be net neutral, we know the charge in the EDL must be equal and opposite the charge of the particle. We can calclate the charge by taking the volume integral of the charge density ρ_E of the EDL in spherical coordinates.

$$q_{particle} = -q_{EDL} \tag{1.11}$$

$$q = q_{particle} = -\int_a^\infty \int_0^\pi \int_0^{2\pi} \rho_E \, sin\left(\psi\right) r^2 \, d\theta d\psi dr \tag{1.12}$$

We can now use the Poission equation (equation 1.4) in spherical coordinates to substitute potential ϕ for the charge density, which gives

$$q = -\int_a^\infty -\frac{\epsilon}{r^2}\frac{d}{dr}r^2\frac{d\phi}{dr}4\pi r^2 \, dr \tag{1.13}$$

$$q = \int_a^\infty 4\pi\epsilon\frac{d}{dr}\frac{d\phi}{dr}r^2 \, dr \tag{1.14}$$

$$q = 4\pi\epsilon a^2 \left(\frac{d\phi}{dr}\right)_{r=a} \tag{1.15}$$

We can solve for the electric field at the particle surface using the linearized Poisson-Boltzmann equation (equation 1.8) and the characteristic length scale of the EDL λ_D (equation 1.10) in spherical coordinates

$$\frac{1}{r^2}\frac{d}{dr}\left(r^2\frac{d\phi}{dr}\right) = \frac{\phi}{\lambda_D} \tag{1.16}$$

Integrating and applying the boundary conditions gives

$$\left(\frac{d\phi}{dr}\right)_{r=a} = -\zeta\left(\frac{1}{a} + \frac{1}{\lambda_D}\right) \tag{1.17}$$

We can determine the relationship between charge and zeta potential by substituting equation 1.17 into equation 1.15

$$\zeta_{sphere} = \left[\frac{q}{4\pi\epsilon a} - \frac{q}{4\pi\epsilon a \left(a + \lambda_D\right)} \right] \tag{1.18}$$

Here we see that the zeta potential of a particle is related to the size and charge of the particle

Next we will derive the relationship between the zeta potential and electrophoretic velocity of the particle. We consider the case where the EDL is much smaller than the radius of the particle ($\lambda_D \ll a$), allowing us to approximate the surface of the particle as planar and thus simply the system to 1D. The Navier-Stokes equation for a steady state, low-Reynolds number system with a unidirectional and uniform electric field $\bar{E}$ is

$$\mu\nabla^2\bar{u} + \rho_E\bar{E} = 0 \tag{1.19}$$

We can substitute the Poisson equation (equation 1.4) into equation 1.19, which gives

$$\mu\nabla^2\bar{u} - \epsilon\nabla^2\phi\bar{E} = 0 \tag{1.20}$$

For our 1D system, equation 1.20 becomes

$$\mu\frac{d^2u}{dr^2} = \epsilon\frac{d^2\phi}{dr^2}\bar{E} \tag{1.21}$$

Integrating and applying the boundary condition $u(r \rightarrow \infty) = 0$ (i.e. the bulk fluid is quiescent) and $\phi\left(r = a\right) = \zeta$ gives the following solution at the surface of the particle

$$u_{EP} = \frac{\epsilon\zeta}{\mu}\bar{E} \tag{1.22}$$

The coefficients are often grouped into the electrophoretic mobility $\mu_{EP} = \frac{\epsilon\zeta}{\mu}$. Thus the electrophoretic velocity is linearly related to the electrophoretic mobility

$$u_{EP} = \mu_{EP}\bar{E} \tag{1.23}$$

Polyacrylamide gel electrophoresis

Polyacrylamide gel electrophoresis (PAGE) is a separation technique often used with proteins where the proteins are sieved by a porous polyacrylamide hydrogel matrix during electrophoresis. While in free solution particles migrate with a velocity proportional to their zeta potential (equation 1.22), particles (i.e. proteins) migrate through the sieving matrix with a velocity related to their size. The physical mechanism of the sieving is an open area of research. However, Ferguson reported an empirical relationship [37]

$$\log\left(\mu_{EP,gel}\right) = \log\left(\mu_{EP,fs}\right) - K_RC_{PA} \tag{1.24}$$

where $\mu_{EP,gel}$ is the electrophoretic mobility of the particle through the gel, $\mu_{EP,fs}$ is electrophoretic mobility in free solution, K_R is the empirically-determined redardation coefficient that describes how much the sieving matrix reduces the electrophoretic mobility of the particle, and C_{PA} is the concentration (% w/v) of the monomer in the gel.

In native conditions, the electrophoretic mobility is a function of both the zeta potential of the protein and the retardation coefficient and thus separations are not purely based on size. However, native separations are useful, as they preserve the native conformation of the protein. Therefore, native separations can be used to assess protein binding and also enzymatic activity. [38–40] Further, sizing under native conditions has been achieved through pore limit electrophoresis where the proteins electromigrate through a polyacrylamide gel with a gradient in pore size (large to small) until they reach pores too small to continue migrating (i.e. their pore limit). [40, 41] While not innately useful for separation proteins by size, native separations remain used to assay proteins in their native conformation.

Protein sizing can be performed in a special case of PAGE where the proteins are denatured and coated with sodiumdocecyl sufate (SDS), an anionic detergent. This size-based separation is called SDS-PAGE or more commonly known as the western blot. [27] The SDS coats proteins at a constant stoichiometry (SDS:amino acid) conferring a constant mass-to-charge ratio and thus giving all proteins the same free solution electrophoretic mobility $\mu_{EP,fs}$. [42] From equation 1.24, we can see that the electrophoretic mobility in the gel $\mu_{EP,gel}$ is now just a function of the retardation coefficient K_R in a polyacrylamide gel with constant polyacrlamide concentration C_{PA}. When the proteins are denatured into linear chains, K_R only depends on their lenght. Therefore, using equation 1.24 in SDS-PAGE we can relate the electrophoretic mobility in the gel $\mu_{EP,gel}$ to the molecular mass of the protein with a log-linear relationship.

Isoelectric focusing

Isoelectric focusing is an equillibrium process that separates proteins by their isoelectric point, which is the pH at the protein has no net charge (Figure 1.4). The separation is achieved by aligning an electric field with a pH gradient such that when proteins are a pH away from their isoelectric point, the migrate towards their isoelectric point via electrophoresis. Thus, each protein species accumulates at its isoelectric point with a width that is a function of the restorative electrophoresis and diffusional broadening. [28, 43]
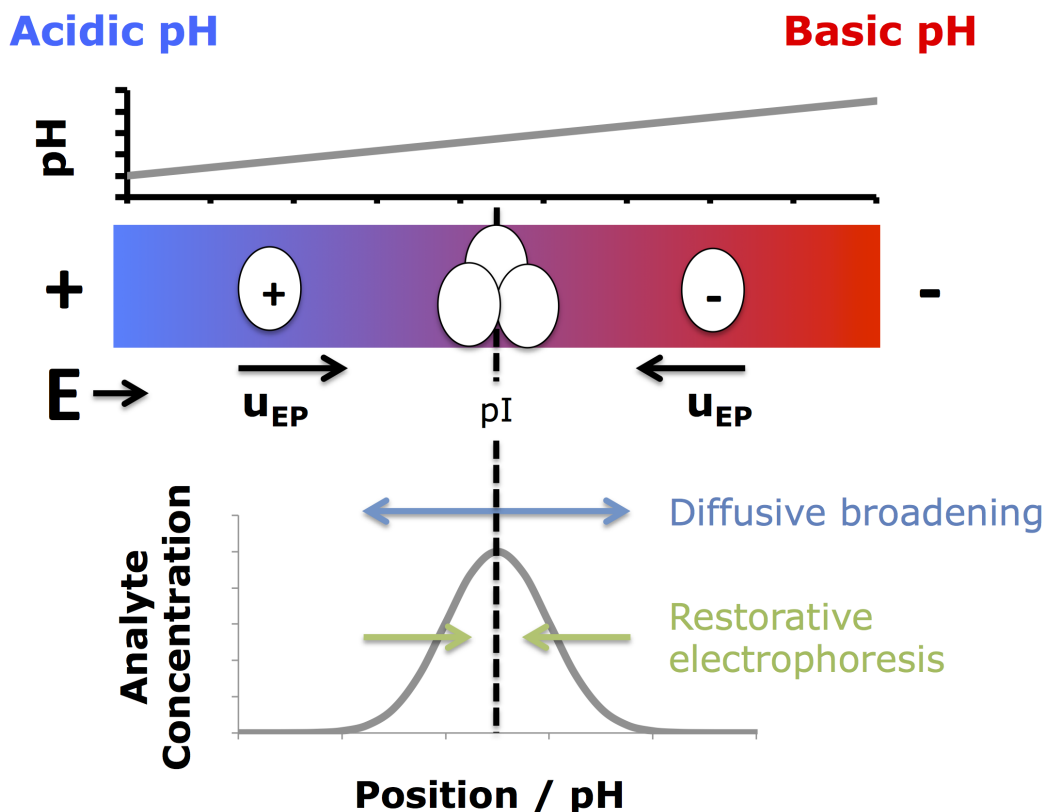
Figure 1.4: Isoelectric focusing enriches proteins at their isoelectric point. The pH gradient and electric field are aligned such that ss proteins migrate away from their pI, the electrophoretic mobility that arises from the proteins becoming protonated or deprotonated returns them to their isoelectric point (i.e. the pH at which they have no net charge). The balance between diffusional broadening and restorative electrophoresis results in a Gaussian concentration distribution about the isoelectric point.

To determine the shape of the focused zone, we consider the transport near the isoelectric point. The convection diffusion equation of a species with concentration C is

$$\frac{\partial C}{\partial t} = - \left(\bar{u} \cdot \nabla \right) C + D\nabla^2 C \tag{1.25}$$

To simplify the analysis, we will consider 1D transport and assume the system has reached equillibrium. Further, we assume that the electricfield E is steady and uniform. Finally, we will solve the equation near the isoelectric point such that the electrophoretic mobility μ_{EP} changes linearly with position. That is

$$-\frac{\partial \mu_{EP}}{\partial x} = \frac{\partial \mu_{EP}}{\partial pH} \frac{\partial pH}{\partial x} \tag{1.26}$$

becomes

$$-\frac{\partial \mu_{EP}}{\partial x} = m \tag{1.27}$$

where m is a scalar constant. The simplified convection-diffusion equation (equation 1.25) is

$$-m \left(x - x_0\right) E = D \frac{d^2 C}{dx^2} \tag{1.28}$$

where x_0 is the peak center (location of the isoelectric point). Integrating and solving equation 1.28 with the boundary conditions $C\left(x = 0\right) = C_0$ and $C\left(x \to \infty\right) = 0$ gives the solution

$$C\left(x\right) = C_0 \exp \left(\frac{\left(x - x_0\right)^2}{\frac{2D}{mE}} \right) \tag{1.29}$$

Thus, the focused zone has a Gaussian distributed concentration with $\sigma = \left(\frac{D}{mE}\right)^{0.5}$.

Separation metrics

To quantify separation performance we consider two key metrics: (1) how well two analytes are resolved and (2) the maximum number of analytes that can be resolved in a single separation axis. For the former, we define the separation resolution R_s, which is the ratio of the distance between two peak centers x_1 and x_2 and the average peak width 4σ [44]

$$R_s = \frac{x_1 - x_2}{0.5\left(4\sigma_1 + 4\sigma_2\right)} \tag{1.30}$$

Similarly, the maximum number of analytes that can be resolved is quantified by the peak capacity n_c. The peak capacity is defined as

$$n_c = \frac{l}{4\sigma} \tag{1.31}$$

where l is separation axis length and 4σ is the average peak width. [44]It is important to note that the peak capacity is a theoretical maximum that is rarely achieved because the species of interest may not be uniformly distributed along the separation axis and the peak width will vary from species to species. To make a conservative estimate, the widest observed peak with is typicall used for 4σ.

References

1. Orr, G. A., Verdier-Pinard, P., McDaid, H. & Horwitz, S. B. Mechanisms of Taxol resistance related to microtubules. *Oncogene* **22,** 7280–7295 (Oct. 2003).

2. Takahashi, K. *et al.* Induction of Pluripotent Stem Cells from Adult Human Fibroblasts by Defined Factors. *Cell* **131,** 861–872 (Nov. 2007).

3. Takahashi, K. & Yamanaka, S. Induction of Pluripotent Stem Cells from Mouse Embryonic and Adult Fibroblast Cultures by Defined Factors. *Cell* **126,** 663–676 (Aug. 2006).

4. Li, J. J., Bickel, P. J. & Biggin, M. D. System wide analyses have underestimated protein abundances and the importance of transcription in mammals. *PeerJ* **2,** e270 (2014).

5. Schwanhäusser, B. B. *et al.* Global quantification of mammalian gene expression control. *Nature* **473,** 337–342 (May 2011).

6. Darmanis, S., Gallant, C. J., Marinescu, V. D. & Niklasson, M. Simultaneous Multiplexed Measurement of RNA and Proteins in Single Cells. *Cell Reports* (2015).

7. Smith, L. M. & Kelleher, N. L. Proteoform: a single term describing protein complexity. *Nature Methods* **10,** 186–187 (Mar. 2013).

8. Gregorich, Z. R. & Ge, Y. Top-down proteomics in health and disease: Challenges and opportunities. *PROTEOMICS* **14,** 1195–1210 (May 2014).

9. Vogel, C. & Marcotte, E. M. Insights into the regulation of protein abundance from proteomic and transcriptomic analyses. *Nature Reviews Genetics* **13,** 227–232 (Mar. 2012).

10. Altelaar, A. F. M., Munoz, J. & Heck, A. J. R. Next-generation proteomics:towards an integrative view ofproteome dynamics. *Nature Reviews Genetics* **14,** 35–48 (Dec. 2012).

11. Tentori, A. M., Yamauchi, K. A. & Herr, A. E. Detection of Isoforms Differing by a Single Charge Unit in Individual Cells. *Angewandte Chemie International Edition* **55,** 12431–12435 (Sept. 2016).

12. Karin, M. How NF-kappaB is activated: the role of the IkappaB kinase (IKK) complex. *Oncogene* **18,** 6867–6874 (Nov. 1999).

13. Karin, M. & Greten, F. R. NF-κB: linking inflammation and immunity to cancer development and progression. *Nature Reviews Immunology* **5,** 749–759 (Sept. 2005).

14. Todeschini, A.-L., Georges, A. & Veitia, R. A. Transcription factors: specific DNA binding and specific gene regulation. *Trends in Genetics,* 1–9 (Apr. 2014).

15. Pandey, A. & Mann, M. Proteomics to study genes and genomes. *Nature* **405,** 837–846 (June 2000).

16. Sun, L. *et al.* Over 10000 Peptide Identifications from the HeLa Proteome by Using Single-Shot Capillary Zone Electrophoresis Combined with Tandem Mass Spectrometry. *Angewandte Chemie International Edition* **53,** 13931–13933 (Oct. 2014).

17. Kelleher, N. L., Thomas, P. M., Ntai, I., Compton, P. D. & LeDuc, R. D. Deep and quantitative top-down proteomics in clinical and translational research. *Expert Review of Proteomics* **11,** 649–651 (Oct. 2014).

18. Lesur, A. & Domon, B. Advances in high-resolution accurate mass spectrometry application to targeted proteomics. *PROTEOMICS* **15,** 880–890 (Feb. 2015).

19. Stack, E. C., Wang, C., Roman, K. A. & Hoyt, C. C. Multiplexed immunohistochemistry, imaging, and quantitation: A review, with an assessment of Tyramide signal amplification, multispectral imaging and multiplex analysis. *Methods* **70,** 46–58 (Nov. 2014).

20. Bendall, S. C., Nolan, G. P., Roederer, M. & Chattopadhyay, P. K. A deep profiler's guide to cytometry. *Trends in Immunology* **33,** 323–332 (July 2012).

21. Bodenmiller, B. *et al.* Multiplexed mass cytometry profiling of cellular states perturbed by small-molecule regulators. *Nature Biotechnology* **30,** 857–866 (Aug. 2012).

22. Huang, B., Wang, W., Bates, M. & Zhuang, X. Three-dimensional super-resolution imaging by stochastic optical reconstruction microscopy. *Science-AAAS-Weekly Paper Edition* **319,** 810–813 (Feb. 2008).

23. Schnell, U. U., Dijk, F. F., Sjollema, K. A. K. & Giepmans, B. N. G. B. Immunolabeling artifacts and the need for live-cell imaging. *Nature Methods* **9,** 152–158 (Jan. 2012).

24. Stadler, C. *et al.* Immunofluorescence and fluorescent-protein tagging show high correlation for protein localization in mammalian cells. *Nature Methods* **10,** 315–323 (Feb. 2013).

25. Teves, S. S. *et al. A Dynamic Mode of Mitotic Bookmarking by Transcription Factors* tech. rep. (July 2016).

26. Melan, M. A. & Sluder, G. Redistribution and differential extraction of soluble proteins in permeabilized cultured cells. Implications for immunofluorescence microscopy. *Journal of Cell Science* **101 (Pt 4),** 731–743 (Apr. 1992).

27. Burnette, W. N. "Western blotting": electrophoretic transfer of proteins from sodium dodecyl sulfate-polyacrylamide gels to unmodified nitrocellulose and radiographic detection with ... *Analytical Biochemistry* **112,** 195–203 (1981).

28. Bjellqvist, B. *et al.* Isoelectric focusing in immobilized pH gradients: principle, methodology and some applications. *Journal of biochemical and biophysical methods* **6,** 317–339 (Sept. 1982).

29. O'Neill, R. A. *et al.* Isoelectric focusing technology quantifies protein signaling in 25 cells. *Proceedings of the National Academy of Sciences of the United States of America* **103,** 16153–16158 (Oct. 2006).

30. Kennedy, R. T., Oates, M. D., Cooper, B. R. & Nickerson, B. Microcolumn separations and the analysis of single cells. *Science* (1989).

31. Hu, S., Zhang, L., Cook, L. M. & Dovichi, N. J. Capillary sodium dodecyl sulfate-DALT electrophoresis of proteins in a single human cancer cell. *ELECTROPHORESIS* **22,** 3677–3682 (Oct. 2001).

32. Kang, C.-C., Lin, J.-M. G., Xu, Z., Kumar, S. & Herr, A. E. Single-Cell Western Blotting after Whole-Cell Imaging to Assess Cancer Chemotherapeutic Response. *Analytical Chemistry* **86,** 10429–10436 (Oct. 2014).

33. Kang, C.-C., Yamauchi, K. A., Vlassakis, J. & Sinkala, E. Single cell-resolution western blotting. *Nature Protocols* (2016).

34. Blazek, M., Santisteban, T. S., Zengerle, R. & Meier, M. Lab on a Chip. *Lab on a Chip* **15,** 726–734 (Jan. 2015).

35. Kirby, B. J. & Hasselbrink, E. F. Zeta potential of microfluidic substrates: 2. Data for polymers. *ELECTROPHORESIS* **25,** 203–213 (Jan. 2004).

36. Kirby, B. J. & Hasselbrink, E. F. Zeta potential of microfluidic substrates: 1. Theory, experimental techniques, and effects on separations. *ELECTROPHORESIS* **25,** 187–202 (Jan. 2004).

37. Ferguson, K. A. Starch-gel electrophoresis—Application to the classification of pituitary proteins and polypeptides. *Metabolism* **13,** 985–1002 (Oct. 1964).

38. Schägger, H. Blue-native gels to isolate protein complexes from mitochondria. *Methods in cell biology* **65,** 231–244 (2001).

39. Silva, A. J. d. *et al.* Blue native-PAGE analysis of Trichoderma harzianum secretome reveals cellulases and hemicellulases working as multienzymatic complexes. *PROTEOMICS* **12,** 2729–2738 (Aug. 2012).

40. Hughes, A. J. & Herr, A. E. Quantitative Enzyme Activity Determination with Zeptomole Sensitivity by Microfluidic Gradient-Gel Zymography. *Analytical Chemistry* **82,** 3803–3811 (May 2010).

41. Tentori, A. M., Hughes, A. J. & Herr, A. E. Microchamber Integration Unifies Distinct Separation Modes for Two-Dimensional Electrophoresis. *Analytical Chemistry* **85,** 4538–4545 (May 2013).

42. Bischoff, K. M., Shi, L. & Kennelly, P. J. The detection of enzyme activity following sodium dodecyl sulfate-polyacrylamide gel electrophoresis. *Analytical Biochemistry* **260,** 1–17 (June 1998).

43. Righetti, P. & Drysdale, J. W. Isoelectric focusing in polyacrylamide gels. *Biochimica et biophysica acta* **236,** 17–28 (Apr. 1971).

44. Giddings, J. C. *et al. Unified separation science* (Wiley New York etc, 1991).

Chapter 2

Subcellular western blotting of single cells

2.1 Introduction

Cellular characteristics can vary widely among a population of cells.[1, 2] Among such characteristics, the subcellular location of a protein is inexorably linked to its function. In a canonical example, transcription factors can be inactive while in the cytoplasm but active once localized to the nucleus where these proteins then regulate transcription.[3, 4] As such, simultaneously ascertaining protein identity and subcellular location yields insight into function and signaling state.

Transfection of fluorescently labeled proteins combined with fluorescence microscopy reports protein dynamics in single cells with high temporal resolution. For example, fluorescent proteins fused to the transcription factor NF-κB have been used to study the dynamics of the translocation of NF-κB from the cytoplasm to the nucleus in response to biochemical stimulus with $\sim$5 min temporal resolution.[5, 6] More recently, embryonic stem cells with fluorescently tagged Sox2 were imaged to quantify transcription factor-binding kinetics with residence times of 1 s.[7] While enabling the measurement of translocation dynamics of proteins with high temporal resolution, fluorescent fusion proteins inherently require transfection of the cells of interest and thus do not allow for the analysis of unaltered, endogenous proteins, which is the focus of the present study.

The *de facto* standard for determining subcellular location of unmodified endogenous proteins in single cells is immunocytochemistry (ICC; or immunofluorescence). Although broadly useful, quantitative ICC is fraught with challenges. Nonspecific background signal is problematic and arises from numerous sources, including antibody cross-reactivity and the fixation method.[8, 9] To demarcate individual cells in micrographs, image analysis al-

gorithms are employed but yield variable results when cell morphologies are diverse and the borders between cells are low-contrast.[10, 11] Enhanced selectivity and throughput would bolster our ability to determine protein subcellular location in individual cells.

To enhance selectivity, western blotting combined with differential detergent fractionation (DDF) has been a mainstay.[12] The selectivity of western blots exceeds that of simple immunoassays by correlating the molecular mass (determined by an upstream electrophoretic separation) with a downstream immunoassay. To report subcellular localization, DDF western blotting uses a pair of specialized cell lysis buffers and two conventional slab-gel western blotting systems. The first lysis buffer lyses only the cytoplasmic compartment of the cells, intact nuclei are fractionated out, and then the pooled cytoplasm is assayed by western blotting. The second lysis buffer lyses the pooled nuclei and the resulting lysate is then subjected to a separate slab-gel western blot13,14.[13, 14] Although more selective than ICC, DDF western blotting lacks the detection sensitivity needed for single-cell resolution.

Single-cell protein analyses have benefited from microfluidic tools.[15, 16] A glass capillary interfaced to an individual cell makes capillary electrophoresis separations possible [17–20], with these "chemical cytometry" approaches primarily focused on metabolomics and enzyme-based reaction monitoring. Electrophoretic analysis of whole cells has benefited from microfluidic systems that locate and lyse each cell at the head of a separation channel. [20, 21] Microchip electrophoresis has been used to count low-copy number proteins [22] and to measure cytoplasmic RNA and genomic DNA from single cells, both with a throughput of ∼10 cells per experimental group.[23] To ensure adequate population sampling of tens to thousands of whole cells, single-cell lysate separations have been reported by forming cell-isolation microwells directly in separation media.[24–29]

To map the cytoplasmic protein profile to the nuclear protein profile in each of hundreds of individual cells, we introduce a subcellular single-cell western blot assay ((sc)^{2}WB). Using a multilayered microfluidic device and an optimized DDF buffer system, we sequentially lyse and western blot the cytoplasm and then the nucleus of hundreds of individual mammalian cells. Lysis reagents are diffusively delivered from a lid layer to individual cells isolated in microwells, thus precisely controlling the serial application of reagents. In the polyacrylamide base layer, we spatially segregate analysis of each compartment to a distinct region of the separation axis in a new bi-directional electrophorsis format. The three-dimensional device and multistage assay are designed for straightforward operation in well-equipped life science laboratories.

2.2   Materials and Methods

Chemicals

Hoechst 33342 (B2261), digitonin (D141), Triton X-100 (100x), sodium dodecyl sulfate (SDS, L4509), sodium deoxycholate (D6750), lipopolysaccharides (LPS) from Escherichia coli (L4524), tetramethylethylenediamine (TEMED, T9281), ammonium persulfate (APS,

A3678), β-mercaptoethanol (M3148), and 30%T, 3.3%C acrylamide/bis-acrylamide (29:1; A3574) were purchased from Sigma-Aldrich (St Louis, MO, USA). In addition, 10x tris-glycine electrophoresis buffer (25 mM Tris, 192 mM glycine, pH 8.3 at 1x) was purchased from Bio-Rad (Hercules, CA, USA) and 20 Tris-buffered saline with Tween 20 (sc-362196) was purchased from Santa Cruz Biotechnology (Dallas, TX, USA). Deionized water (18.2 MΩ) water was obtained from a Millipore Ultrapure water purification system (Billerica, MA, USA). N-[3-[(3-benzoylphenyl) formamido]propyl] meth-acrylamide (BPMAC) was synthesized by Pharm-Agra Laboratories (Brevard, NC, USA). [25, 26] Paraformaldehyde (157-4) was obtained from Electron Microscopy Services (Hatfield, PA, USA).

Antibodies

Antibodies include rabbit anti-turboGFP (1:35, PA5-22688, Pierce Antibody Products, Waltham, MA, USA, with AlexaFluor 647-conjugated anti-rabbit secondary antibody), rabbit anti-β-tubulin (1:10, ab6046, Abcam, Cambridge, MA, USA, with AlexaFluor 647-conjugated anti-rabbit secondary antibody), rabbit anti-SFPQ (1:10, ab38148, Abcam, with AlexaFluor 647-conjugated anti-rabbit secondary antibody), mouse anti-PTBP1 (1:10, H00005725-M01, Abnova, Taipei City, Taiwan, China, with AlexaFluor 555-conjugated anti-mouse secondary antibody), rabbit anti-calnexin (1:10, ADI-SPA-865, Enzo, Farmingdale, NY, USA, with AlexaFluor 647-conjugated anti-rabbit secondary antibody), mouse anti-GRP-75 (1:10, ab82591, Abcam, with AlexaFluor 555-conjugated anti-mouse secondary antibody), and rabbit NF-κB (1:30, 8242, Cell Signaling, Danvers, MA, USA, AlexaFluor 647-conjugated anti-rabbit secondary antibody).

Cell culture

U373 MG human glioblastoma cells were obtained from the UC Berkeley Tissue Culture Facility via the American Type Culture Collection. Green fluorescent protein (GFP)-expressing U373 cells were stably transduced with TurboGFP via lentiviral infection (multiplicity of infection = 10). The U373 MG cells have been discovered to share a common origin with the U251 human glioblastoma cell line. However, the cells have since diverged into distinct karyotypes. [30] Mouse embryonic fibroblasts expressing mitochondria-targeted enhanced GFP (EGFP) [31] were gifted by Dr. Suzanne Wolff and Dr. Brendan Battersby.

All cells were cultured in high-glucose Dulbeccos modified eagle medium (DMEM) (11965, Life Technologies, Carlsbad, CA, USA) supplemented with 1 MEM nonessential amino acids (11140050, Life Technologies), 100 U mL^{-1} penicillin-streptomycin (15140-122, Life Technologies), 1 mM sodium pyruvate (11360-070), and 10% fetal bovine serum (JR Scientific, Woodland, CA, USA) in an incubator at 37 °C with humidified 5% CO_2 air.

SU8 wafer and (sc)^{2}WB fabrication

The SU8 wafers and scWB devices were fabricated as previously reported. [25, 26] The microwells were 32 μm in diameter and 40 μm deep. The well spacing was 1 mm along the separation axis and 0.25 mm transverse to the separation axis. The polyacrylamide gel precursor (8%T acrylamide/bis-acrylamide, 3 mM BPMAC) was polymerized with 0.08% APS and 0.08% TEMED. The polyacrylamide lids were fabricated using previously reported photopatterning methods32. The precursor (15% 29:1 acrylamide/bis-acrylamide, 1% VA-086 in water) was polymerized for 45 s at 20 mW cm^{-2}. The lids measured 50 x 70 x 0.5 mm.

Hydrogel lid fabrication

The polyacrylamide lids were fabricated using previously reported photopatterning methods32. Briefly, the polyacrylamide precursor (15% 29:1 acrylamide/bis-acrylamide, 1% VA-086 in water) was introduced between two hydrophobic glass plates (coated with Gel Slick) separated by 500 μm tall spacers. The glass plates were then placed on top of a photomask containing the pattern for the lids (rectangle measuring 50 x 70 mm), and the polyacrylamide was polymerized with ultraviolet light ($\lambda = 365$ nm) for 45 s at 20 mW cm^{-2}. The completed lids measured 50700.5mm. Following fabrication, the lids were soaked in the appropriate buffer for 1 hour.

(sc)^{2}WB operation

First, cells suspended in phosphate-buffered saline (PBS; 500 000 cells per mL) were pipetted on top of the base layer of the (sc)^{2}WB. The cells were allowed to settle into the microwells for 10 min via sedimentation at 4 °C. Next, the excess cell suspension was washed off of the surface of the base layer of the (sc)^{2}WB with PBS, leaving only the cells in the microwells. The PBS was exchanged out of the base layer by incubating in 1x Tris-glycine for 20 s. The cell-containing base layer was transferred to the electrophoresis chamber. The lid containing the cytoplasm-specific buffer (Table 2.1) was placed on top of the base layer, initiating lysis. After the completion of lysis (Table 2.2), the electric field was activated (40 V cm $^{-1}$) and polyacrylamide gel electrophoresis (PAGE) was performed on the cytoplasmic fraction (Table 2.2). Immediately following the cytoplasmic PAGE, the proteins were immobilized by exciting the benzophenone in the polyacrylamide gel with ultraviolet light for 45 s. Next, the lid containing the cytoplasm-specific buffer was removed and replaced with the lid containing the nucleus-specific buffer (Table 2.1), initiating lysis of the intact nuclei retained in the microwells. After completion of the nuclear lysis, PAGE on the nuclear fraction was performed by applying an electric field in the opposite polarity of the cytoplasmic PAGE step (Table 2.2). Following the completion of the nuclear PAGE step, the nuclear proteins were immobilized by exposing the (sc)^{2}WB device to ultraviolet light for 45 s. Finally, the immobilized proteins were immunoprobed as previously described. [25]

Table 2.1: Formulation of the cytoplasm- and nucleus-specific lysis buffers.

	Cytoplasm-specific buffer	Nucleus-specific buffer
Sodium dodecyl sulfate	—	10 mg mL^{-1}
Sodium deoxycholate	—	5 mg mL^{-1}
Triton X-100	1% v/v	0.1% v/v
Digitonin	0.125 mg mL^{-1}	—
Tris-glycine	0.5x	0.5x

Table 2.2: Lysis and electrophoresis conditions used in (sc)^{2}WB.

Targets	Figure	Cell	Cytoplasm			Nucleus		
			t_{lysis} [s]	t_{EP} [s]	E [V/cm]	t_{lysis}	t_{EP}	E [V/cm]
TurboGFP, Lamin A/C	1B	TurboGFP-U373	25	17	40	20	20	40
TurboGFP, β-tubulin, PTBP1, SFPQ, HSP90, Erk	1F	TurboGFP-U373	25	16	40	20	35	40
TurboGFP, β-tubulin, Lamin A/C	2	TurboGFP-U373	25	17	40	20	20	40
mtGFP, GRP75, Calnexin	2	Mouse embryonic fibroblasts	25	8	66.67	20	12	66.67
TurboGFP, H3	2	TurboGFP-U373	25	15	66.67	20	15	66.67
TurboGFP, β-tubulin, PTBP1, SFPQ,	3	TurboGFP-U373	25	16	40	20	35	40
NF-κB	4	U373	25	35	100	25	10	66.67

t_{lysis} is the duration of lysis, t_{EP} is the duration of PAGE, and E is the magnitude of the electric field.

(sc)^{2}WB quantification

Fluorescence was measured using a Genepix 4300A (Molecular Devices, Sunnyvale, CA, USA) and appropriate laser and filter sets. Image processing was performed using a custom MATLAB script. Briefly, the image was segmented in separation lanes. Gaussian distributions were fit to the protein bands. Signal-to-noise ratio (SNR) > 3 and $R^2 > 0.7$ were used as thresholds for peak calling. The peak widths for the area under the curve analysis were 4σ.

Immunocytochemistry

The cells were settled on glass coverslips at a density of 5 x 10^5 cells per cm^2 and then were cultured and fixed with 4°C paraformaldehyde for 15 min. The fixed cells were washed three times (5 minutes each) in PBS and then were blocked and permeabilized in staining buffer (5% donkey serum, 0.3% Triton X-100, in TBST). The cells were incubated with primary antibody (1:200, anti-NF-κB) diluted in staining buffer for 12 h at 4 °C and then were washed three times (5 minutes each) in staining buffer. Cells were incubated in secondary antibody (1:300, AF647-labeled anti-rabbit) for 1 h at 20 °C, washed three times (5 minutes each) and counterstained with Hoechst 33342 (1 g mL $^{-1}$). The cells were imaged as described below with fluorescence quantified using CellProfiler. [11]

2.3 Results and Discussion

Fundamental considerations for the (sc)^{2}WB assay and device designs

The subcellular single-cell western blot assay or (sc)^{2}WB isolates single cells in microwells and uses microfluidic control of DDF buffer pairs to lyse, solubilize, and electrophoretically analyze proteins from the cytoplasm and subsequently the nucleus of each isolated cell (Figure 2.1). Importantly, both the cytoplasmic western blot assay and the nuclear western blot assay are indexed to the originating microwell, thus allowing direct correlation between the cytoplasmic and nuclear protein profiles of each cell analyzed. The indexing is achieved by "bi-directional" western blotting. In bi-directional western blotting, each interspersed PAGE assay is performed along the same separation axis; however, the protein solubilized from each subcellular compartment is electrophoresed in the opposite direction (that is, "east" of the originating microwell for the cytoplasmic lysate and "west" for the nuclear lysate).

Thus, the (sc)^{2}WB consists of three stages (Figure 2.1). Stage 1, cytoplasmic protein separation: chemical lysis of the cytoplasm only, PAGE of solubilized cytoplasmic proteins while each intact nucleus is retained in the microwell, and blotting (photoimmobilization) of separated proteins to the hydrogel via ultraviolet (UV) activation of the photoactive gel. Stage 2, nuclear protein separation: chemical lysis of the intact nuclei, PAGE of solubilized nuclear proteins, and UV-based blotting of proteins to the hydrogel. And Stage 3, probing of both protein separations: probing and imaging of the immobilized proteins from each subcellular compartment with fluorescently labeled antibodies. Throughput of the microwell array can reach up to ~7000 cells per device [25]. However, the number of microwells with single-cell occupancy is cell-type-dependent (for example, depending on the density and morphology). [25, 26] For the cells studied here, a microwell occupancy of one was achieved for on the order of 100 cells per device.

The small length scales of both the sample (cells) and device features make diffusion a dominant mass transport mechanism. While the protein concentrations are high within an intact, whole cell (nM to μM) [32], the small dimensions of the subcellular compartments ($l_{nuc} \sim 15\mu m$; $l_{cyt} \sim 30\mu m$) lead to rapid dilution by diffusion after lysis (Figure 2.2). To estimate the dilution effects in the (sc)^{2}WB, we consider lysis of GFP from a single cell (molecular mass: 27 kDa; D = 88 μm^2 s^{-1}) [25]. Using a diffusion timescale of $\tau = \frac{x^2}{2D}$, where x is the diffusion length and D is the diffusivity of the species, the characteristic time for GFP to diffuse 10 μm to the open top of the microwell is ~0.6 s. On the other hand, the delivery of reagents over short distances is efficient. Using similar scaling, we estimate the time required for diffusive transport of lysis buffer components (D = 80 μm^2 s^{-1} for Triton X-100 micelles [33]) from the top of a microwell to the cell to be $\sim$ 0.7 s.

Consequently, we sought to design the (sc)^{2}WB microdevice to diffusively control reagent transport and allow the following: (i) selective lysis and protein solubilization of each cellular compartment using diffusion-based delivery of the DDF buffer pairs and (ii) rapid, near lossless transition to PAGE of both the 14 pL cytoplasmic and 2 pL nuclear compartments
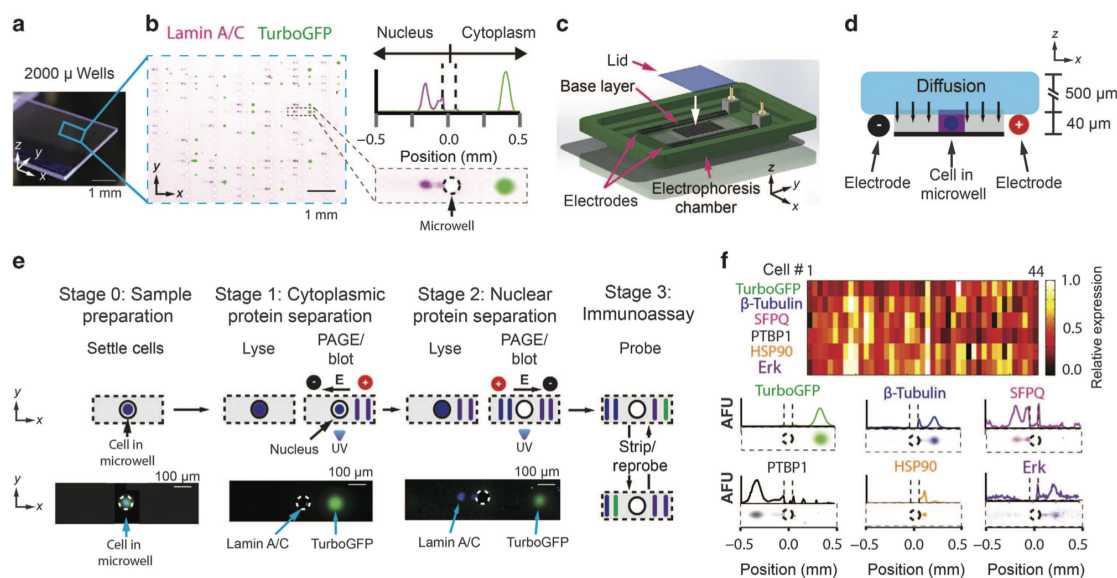
Figure 2.1: Microfluidic subcellular western blotting reports protein localization to the cytoplasmic or nuclear compartment of single cells. (**a**) Photograph of the base layer and microwell array of the (sc)^{2}WB device, with (**b**) insets showing the fluorescence micrograph of the subcellular western blot array (56 U373 cells) for lamin A/C (magenta) and TurboGFP (green) and for a single U373 cell with a companion intensity profile plot. (**c**) Rendering of the assembled (sc)^{2}WB device. (**d**) Schematic cross-section in the xz plane of (**c**). When placed atop the base layer, the 500 m-thick hydrogel lid simultaneously delivers the lysis reagents via diffusion and electrically addresses the base layer for rapid transition between the lysis and electrophoresis stages. (**e**) Schematic of the (sc)^{2}WB workflow: (Stage 0) Settle single cells into microwells via sedimentation; (Stage 1) cytoplasm-specific lysis buffer is diffusively applied from the lid, PAGE is performed on solubilized cytoplasmic proteins along the separation axis to the "'east" of the microwell, and the cytoplasmic proteins are photo-immobilized to the gel; (Stage 2) nucleus-specific lysis buffer is diffusively applied from the lid, PAGE is performed on solubilized nuclear proteins along the separation axis to the "west" of the microwell, and nuclear proteins are photo-immobilized to the gel; (Stage 3) in-gel immunoprobing and image fluorescence are performed. At bottom: (Step 0) false-color fluorescence micrographs of an intact cell in a microwell; (Step 1) PAGE of cytoplasmic GFP (E = 40 V cm^{-1}; Δt = 10 s) with the nucleus retained in the microwell; (Step 2) western blotting after bi-directional PAGE with cytoplasmic protein east and nuclear protein west of the microwell. The microwells are encircled with a white dashed line for clarity; TurboGFP (green) and Hoechst DNA stain (blue). (**f**) Stripping and reprobing for the expression and localization of six protein targets from one mammalian cell. The relative expression (AUC/AUC$_{max}$) is reported for n = 44 U373 cells. GFP, green fluorescent protein; PAGE, polyacrylamide gel electrophoresis.
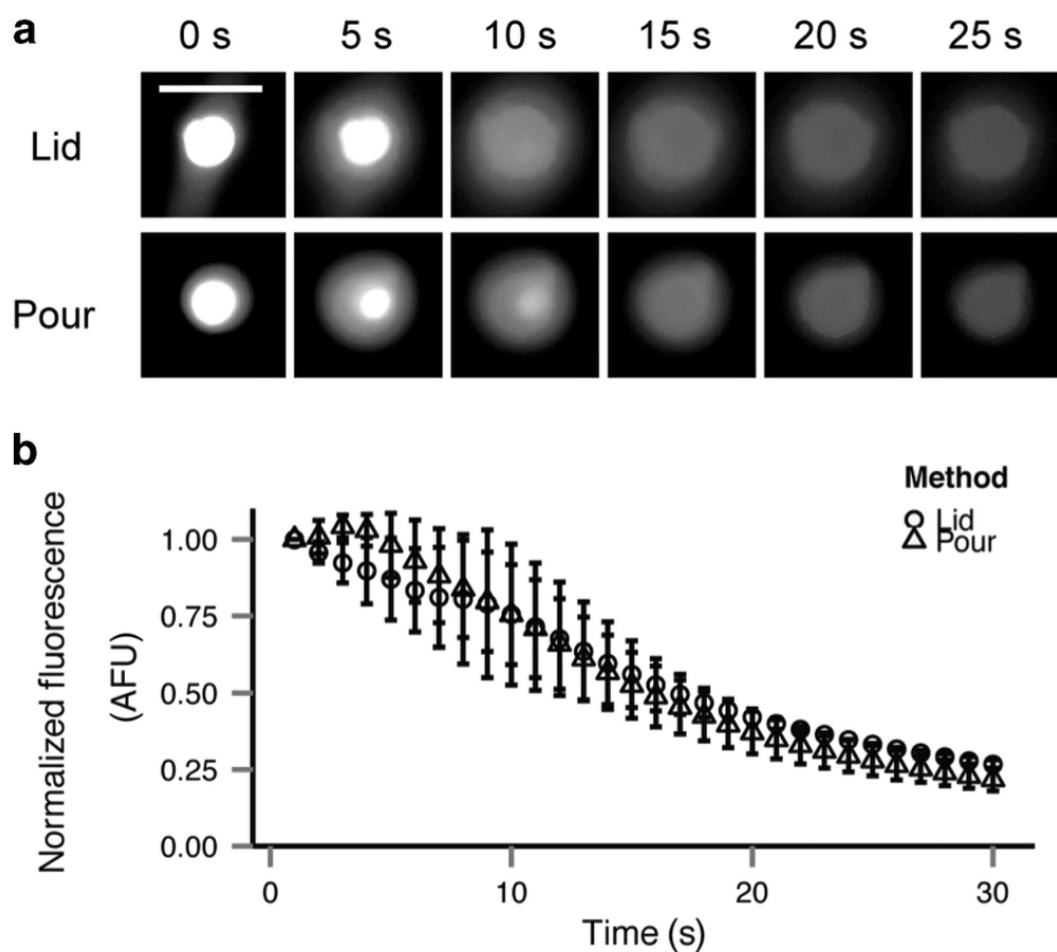
Figure 2.2: Comparison of diffusive (lid-based) and advective (pour-based) lysis buffer delivery. (**a**) Micrographs of TurboGFP-expressing U373 cells lysing after lid-based and pour-based delivery of the cytoplasm-specific lysis and electrophoresis buffer. (**b**) Normalized fluorescence (AFUcurrent/AFUinitial) of TurboGFP during lysis of single TurboGFP-expressing U373 cells (n = 3). After 30 s, only $21.8 \pm 3.70\%$ of the TurboGFP remained after pouring buffer over the array and $26.7 \pm 1.43\%$ remained with the hydrogel lid delivery. Error bars are $\pm$ 1 standard deviation.

(Figures 2.1c and d). To afford both capabilities, we arrived at a multilayer device design consisting of a thin hydrogel "base" layer (40 μm thick, on a microscope slide) stippled with cell-isolating microwells that is capped by thick buffer-soaked hydrogel "lid" layers (500 μm thick).

First, to afford the rapid, sequential delivery of the DDF buffers, a sequence of the buffer-soaked hydrogel "lids" is used. Once in direct fluidic contact, the lids diffusively deliver lysis buffer constituents into the microwells. An essential aspect of the lid design is the elimination of the convective delivery of reagents (pouring) because we have observed ∼40% lysate loss when whole-cell lysis buffer is gently poured over the array. [25] Each buffer-soaked lid is 100x the volume of the base layer to approximate an infinite buffer source (that is, the lid volume is orders of magnitude greater than the base layer volume). The 500 μm thick (15%T polyacrylamide (PA) gel) lids are compliant and conform readily to the planar base layer. The lids remain hydrated over the duration of the assay due to their relatively large volume (∼10 x greater than the bottom layer) and the rapid ($\leq$ 35 s) electrophoresis steps. Furthermore, the lids synchronize the delivery of each DDF lysis buffer to the microwells and allow the serial application of the two buffers by simply exchanging the lid containing the cytoplasm-specific buffer for the lid containing the nucleus-specific buffer. Second, we directly molded the microwells into the PAGE sieving matrix, providing nearly instantaneous switching from lysis to PAGE by simply applying an electric field across the entire base layer.

Establishing the orthogonality of the microfluidic DDF system

We sought to empirically validate the orthogonality of the cytoplasmic and nuclear DDF lysis. The cytoplasm-specific lysis buffer comprises non-ionic detergents (digitonin, Triton X-100), which present a bulky head group that solubilizes the cell membrane but do not disrupt the nuclear lamina structure (formed by proteinprotein interactions), thus leaving the nucleus intact. [13, 34] The nucleus-specific lysis buffer comprises anionic detergents (SDS, sodium deoxycholate) that disrupt the nucleus and solubilize nuclear proteins. [13, 34] All detergents are above their critical micelle concentration for effective protein solubilization. [34] To ensure sufficient electrophoretic mobility, both DDF lysis buffers are buffered to pH 8.3 with Tris-glycine [25] (Table 2.1). Because most cytoplasmic proteins have an isoelectric point below pH 8.3, the Tris-glycine-buffered cytoplasm-specific lysis buffer confers a negative charge and thus an electrophoretic mobility toward the anode. [35] Due to native conditions, the cytoplasmic electrophoretic separation occurs on the basis of both the shape and charge of the proteins. [36] Interestingly, the mild, non-ionic detergents retain protein-protein interactions, as suggested through our observations of an intact lamina structure (Figure 2.1e) and as corroborated by observations from other groups. [13, 34] Such observations suggest that the (sc)^{2}WB may be optimized to specifically interrogate cytoplasmic proteinprotein interactions and potentially enzymatic activity. [34]

To first empirically validate the cytoplasm-specific DDF buffer, we settled human glioblastoma cells (U373) expressing TurboGFP into the microwell array. To concurrently visualize the cytoplasm (GFP, green) and nucleus of each cell, we stained the DNA with Hoechst

33342 (blue). We applied the cytoplasm-specific DDF buffer lid to the array in o1s (Figure 2.1e). During and after the application of the cytoplasm-specific DDF lid, we monitored the solubilization and electrophoresis of TurboGFP via time-lapse microscopy.

Upon application of the DDF lid, we observed cell lysis within 1 s (n = 3) with the TurboGFP signal filling the microwell. At 25 s of elapsed lysis time, we applied an electrical potential across the base layer (40 V cm^{-1}) and observed synchronized electromigration of TurboGFP out of the microwell (Figure 2.3). To quantify the uniformity of the electromigration, we measured the migration distance of TurboGFP across the array and found a coefficient of variance, CV = 6.4% (n = 187 cells).

To verify that the cytoplasmic indicator protein (TurboGFP) was localized to the PAGE gel region and that the nuclear proteins remained localized to the microwells, we immobilized protein in the base layer via UV activation of the benzophenone groups (45 s) in the gel after 14 s of PAGE. [25, 26, 37] As expected, we did not observe detectable green signal (GFP) within the microwells (n = 3, SNR > 3). As a proxy for the maintenance of the nuclear structure after cytoplasmic PAGE, we imaged Hoechst-stained DNA and observed retention of the DNA in each microwell (n = 3). To inspect the state of the nuclear proteins, we immunoprobed for lamin A/C, a nuclear envelope protein (Figure 2.1e, Stage 1). Using end point fluorescence imaging, we observed the GFP signal localized to the PAGE regions of the gel base layer and lamin A/C signals localized to the microwells (Figure 2.1e).

After the cytoplasmic PAGE step (Figure 2.1e, Stage 1), visual inspection of cell-laden microwells revealed both a stained DNA signal and a lamin A/C signal. The positive signals indicate that the non-ionic detergents comprising the cytoplasmic lysis buffer maintained intact nuclei in each microwell, corroborating literature observations. [38, 39] On the basis of similar observations from bulk (pooled cell) DDF, we anticipate that the intact nucleus retains most nuclear proteins. [13, 14, 38] Nevertheless, careful validation of bulk and single-cell DDF western blotting should be conducted when macromolecular targets are > 50 kDa, especially when not bound to DNA, as these smaller species may diffuse out of the intact nucleus within minutes, through nuclear pores. [40, 41] As the proteins considered here are retained in the intact nuclei, the molecular targets should be sheltered from any advection generated during lid exchange of the cytoplasmic to nuclear DDF buffers. Further, during lid exchange, visual inspection of the intact nuclei in each microwell did not report the loss of nuclei for any cell analyzed in this study.

We next scrutinized a range of proteins with accepted and well-characterized single-compartment localization (Supplementary Table 2.3). For targets localized to a single compartment, we report a 100% localization to that specific compartment (for example, 100% cytoplasmic localization with 0% nuclear localization). An important performance metric relevant to assigning the localization fraction is the limit of detection of the (sc)^{2}WB in-gel immunoassay, which is ~45 zeptomoles. [25] For the nucleus-specific targets, we observed $100.0 \pm 0.0\%$ (n = 32) of the lamin A/C signal localized to the region west of the microwells (Figure 2.4a). To increase confidence in the nuclear analysis, we also probed for histone 3, a nucleus-specific protein (Figures 2.4c and d), and observed $100.0 \pm 0.0\%$ (n = 22) of the histone 3 signal in the nuclear fraction. Next, in assessing the cytoplasm-specific protein

Figure 2.3: Characterization of electromigration uniformity. Inverted micrograph of TurboGFP-expressing U373 cells assayed with the $(sc)^2WB$ for TurboGFP after cytoplasm-specific lysis. TurboGFP-expressing U373 cells were settled into the $(sc)^2WB$ device. The cytoplasmic lysis buffer was applied for 25 s. An electric field (40 V cm^{-1}) was applied for 17 s immediately following the completion of lysis. The TurboGFP average peak center location x $= 397.0 \pm 25.4$ μm (n $= 187$), which yields a coefficient of variation, CV $= 6.4\%$.

panel, we observed $100.0 \pm 0.0\%$ (n = 32) of the TurboGFP and $100.0 \pm 0.0\%$ (n = 32) of the β-tubulin localized to the gel region "east" of each microwell. These findings suggest that the microfluidic DDF system successfully performs rapid compartment-specific lysis of single cells, for $\sim$30 cells concurrently. The buffer formulations and technique provide nuclear selectivity, even during cytoplasmic lysis and PAGE analysis of the cytoplasmic lysate.

Table 2.3: Single compartment targets assayed by $(\text{sc})^2\text{WB}$

Target	Cell type	Localization
TurboGFP	U373	Cytoplasm
β-tubulin	U373	Cytoplasm[1]
GRP75	mtGFP-expressing mouse embryonic fibroblast	Mitochondria[2]
Calnexin	mtGFP-expressing mouse embryonic fibroblast	Endoplasmic reticulum[3]
mtGFP	mtGFP-expressing mouse embryonic fibroblast	Mitochondria[4]
Lamin A/C	U373	Nucleus[5]
H3	U373	Nucleus[6]
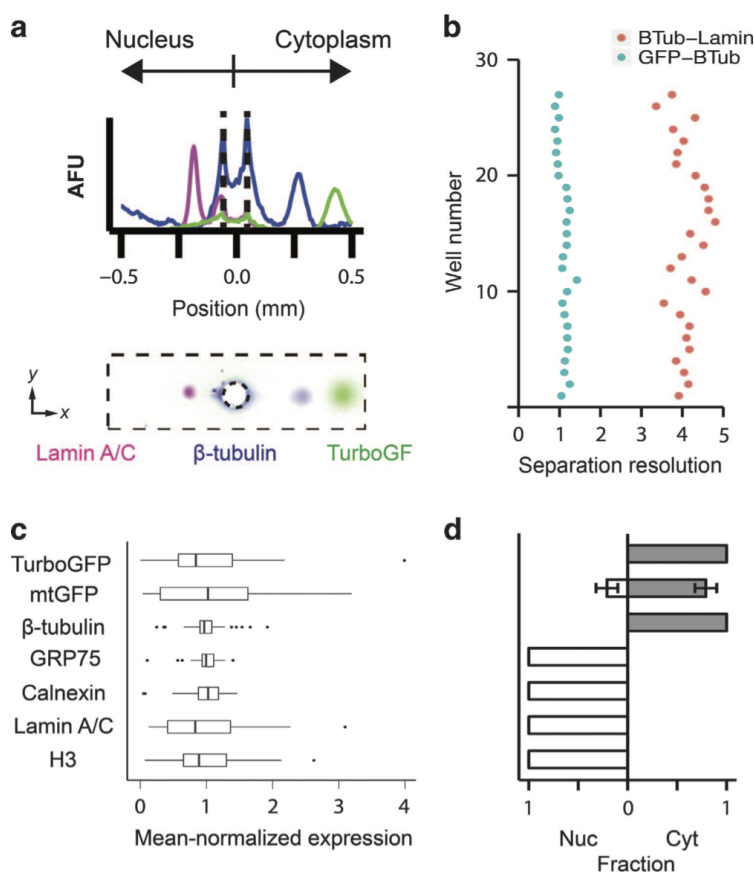
Figure 2.4: The (sc)^{2}WB assay detects a panel of well-described protein targets, thus validating target and localization selectivity. (**a**) Intensity profile and false-color fluorescence for a representative (sc)^{2}WB assay (TurboGFP, green signal; β-tubulin, blue signal; lamin A/C, magenta signal; U373-GFP cells; lysis duration: 25s; PAGE duration: 17 s at E = 40 V cm^{-1}). Dashed lines in the intensity profile denote the microwell border. Cytoplasmic proteins are to the right (west) of the microwell and nuclear proteins are to the left (east). (**b**) Separation resolution of a 1-mm PAGE separation distance (n = 27 cells). (**c**) Mean-normalized expression (AUC/AUC$_{mean}$) and (**d**) subcellular localization (Nuc = AUC$_{nuclear}$/AUC$_{total}$, Cyt = AUC$_{cytoplasm}$/AUC$_{total}$) as determined by the (sc)^{2}WB for membranous organelles: mitochondria-targeted GFP, Calnexin (ER), and GRP-75 (mitochondrial matrix), cytoplasmic (TurboGFP, β-tubulin), and nuclear (lamin A/C, H3) targets. Error bars are ± 1 s.d. ER, endoplasmic reticulum; GFP, green fluorescent protein; PAGE, polyacrylamide gel electrophoresis; s.d., standard deviation.

In seeking to assess the suitability of the cytoplasm-specific lysis buffer for organelle-associated proteins, we assayed mouse embryonic fibroblasts for mitochondria-targeted EGFP (mtGFP), GRP-75 (mitochondrial matrix protein), and calnexin (an endoplasmic reticulum-localized protein). End point fluorescence imaging reported 79 ± 11% (n = 103) of the

mtGFP in the cytoplasmic fraction, whereas the GRP-75 and calnexin were found entirely in the nuclear fraction (Figures 2.4c and d). Although conventional DDF western blots using the same cytoplasmic lysis buffer detergent formulation have successfully solubilized and extracted proteins from membranous organelles in mammalian cells [13], we hypothesize that the short lysis durations of the $(sc)^2WB$ (1030s versus 1800s with conventional DDF) may not fully solubilize this subset of targets (that is, mitochondria-targeted GFP and endoplasmic reticulum protein) [13]. The timescale of diffusive losses from the microwells limits the maximum duration of the lysis step (Supplementary Figure 2.2). The minimum lysis time is set by the time to solubilize targets of interest and the time for the lysis reagents to diffuse into the microwell ($\tau_{diff.} < 10s$ [29]). Design modifications optimized to mitigate diffusive protein losses should extend the maximum attainable lysis duration, with the possibility of fully solubilizing difficult-to-solubilize compartments (for example, mitochondrial and endoplasmic reticulum proteins).

Next, using the protein panel, we assessed the separation resolution and peak capacity of the bi-directional PAGE (that is, TurboGFP, β-tubulin, and lamin A/C from GFP-expressing U373 cells, Figure 2.4a). The total separation length was 1 mm, with 0.5 mm in the direction east and west of the indexed microwell. After PAGE and blotting in uniform 8%T gels, we fit Gaussian distributions to the fluorescence signal from each of the immunoprobed protein peaks to extract peak center (x) and shape (σ, standard deviation (s.d.); where peak width w = 4σ). The separation resolution (R_S) is defined as $R_S = \frac{x_1 - x_2}{0.5(w_1 + w_2)}$, where the subscripts describe each of the adjacent peaks. From each of the 17 s duration PAGE separations, all peak pairs were fully resolved with the separation resolution between lamin A/C and β-tubulin at 4.27 ± 0.53 and between β-tubulin and TurboGFP at 1.14 ± 0.07 (n=32, Figure 2.4b). Thus, in the $(sc)^2WB$, the cytoplasmic and nuclear fractions of the proteome are spatially separated. Owing to advances in microscopy, ICC can resolve the localization of proteins with 2030 nm resolution but requires the use of image processing to correlate localization with subcellular features. [42] By spatially separating the cytoplasmic and nuclear compartments, the $(sc)^2WB$ eliminates the need for the challenging cell segmentation algorithms used in ICC. [10, 11]

For a conservative estimate of peak capacity ($n_c = L/w$, where L is the length of the separation axis) [43], we used the widest protein peak and estimated an $n_c = 10.37 \pm 0.5$ (n = 32). This n_c places the multiplexing capability the $(sc)^2WB$ on par with state-of-the-art single-cell protein analysis tools. Antibody barcode assays report 11 protein targets per cell [44] and ICC reports four to five targets per cell. [45] This novel bi-directional PAGE assay reports a true nucleocytoplasmic profile for each cell, with multiplexing demonstrated up to six protein targets spanning both the cytoplasmic and nuclear compartments of one cell (Figure 2.1f).

Spliceosome-associated proteins

The link between nucleocytoplasmic distribution of spliceosome proteins and disease is not fully understood. The spliceosome is a large molecular machine (composed of nuclear RNA

and protein complexes) that removes introns from transcribed pre-mRNA in eukaryotic cells47 and can generate alternate proteins (splicing), a phenomenon of growing interest in cancer therapy. [46] Two important spliceosome proteins are SFPQ (namely PSF) and PTBP1 [47, 48]; both are thought to promote aggressive cancer phenotypes with SFPQ aberrantly localized to the cytoplasm in Alzheimers disease. [46, 49, 50] Importantly, assaying spliceosome-associated proteins is challenging due to the promiscuity of the proteins involved and the importance of localization to function. [47, 51]

Here, we sought to measure the expression and localization of four protein targets using the $(sc)^2WB$ two cytoplasmic proteins (β-tubulin, 50 kDa, and TurboGFP, 27 kDa) and two nuclear proteins (PTBP1, 57 kDa, and SFPQ, 76 kDa; Figure 2.5a) in GFP-expressing U373 cells. Across an array of 44 cells (Supplementary Figure 2.6), the multiparameter $(sc)^2WB$ resolved all four proteins (Supplementary Table S5) with the anticipated compartment localization (Figure 2.5d). SFPQ had the largest interquartile range (IQR = Q3 Q1, where Q1 and Q3 are the first and third quartiles, respectively) in mean-normalized expression (IQR_{SFPQ}=0.68). Furthermore, the SFPQ and β-tubulin proteins exceeded baseline resolution ($R_s = 3.33 \pm 0.35$), even with a small 12.3% molecular mass difference between the pair. To our knowledge, the baseline resolution of two proteins differing by just 7 kDa is the smallest resolved peak pair to date for an immunoprobed single-cell electrophoretic separation of endogenous proteins. Our previously reported whole-cell scWB could not resolve SFPQ and β-tubulin within a uni-directional 1 mm PAGE separation distance (Figure 2.5b), thus underscoring the utility of bi-directional PAGE in subcellular analyses.
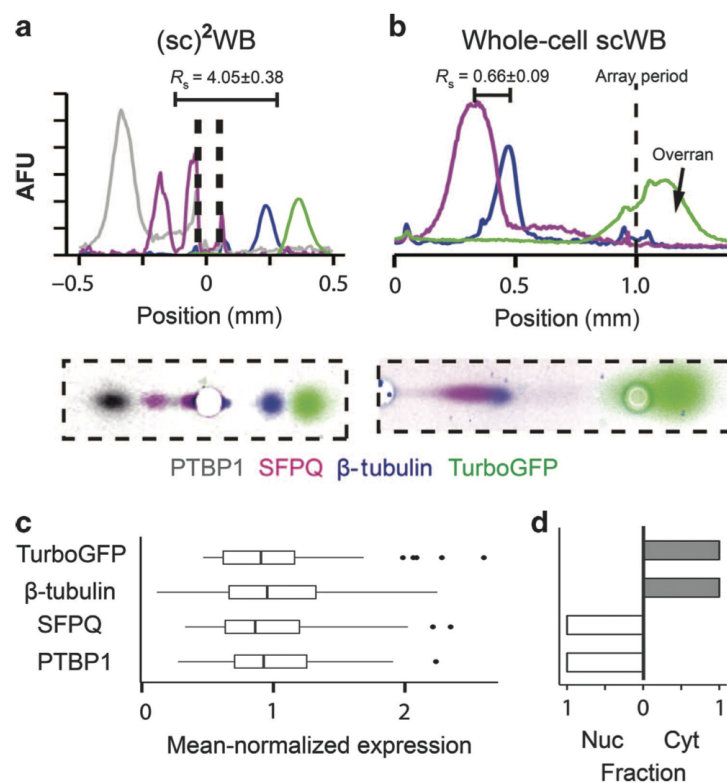
Figure 2.5: Spliceosome protein localization and expression in single mammalian cells. (**a**) The (sc)²WB assigns subcellular localization to cytoplasmic (TurboGFP, green; β-tubulin, blue) and nuclear (SFPQ, magenta; PTBP1, gray) proteins, even when the targets are components of large molecular machines. The dashed line is the microwell border. A representative intensity profile and false-color micrograph are shown here. A dashed line denotes the microwell border in the intensity profile. (**b**) Bi-directional PAGE enhances selectivity because uni-directional PAGE cannot resolve β-tubulin and SFPQ. The dashed line indicates the position of the next row of microwells (array period). Note that in the whole-cell scWB, the TurboGFP band has overrun into the next separation lane. (**c**) Mean-normalized expression ($\mathrm{AUC}/\mathrm{AUC}_{mean}$) and (**d**) subcellular localization (Nuc = $\mathrm{AUC}_{nuclear}/\mathrm{AUC}_{total}$, Cyt = $\mathrm{AUC}_{cytoplasm}/\mathrm{AUC}_{total}$) of TurboGFP, β-tubulin, SFPQ, and PTBP1 (n=44 cells). Error bars are $\pm$ 1 s.d. GFP, green fluorescent protein; PAGE, polyacrylamide gel electrophoresis; s.d., standard deviation.
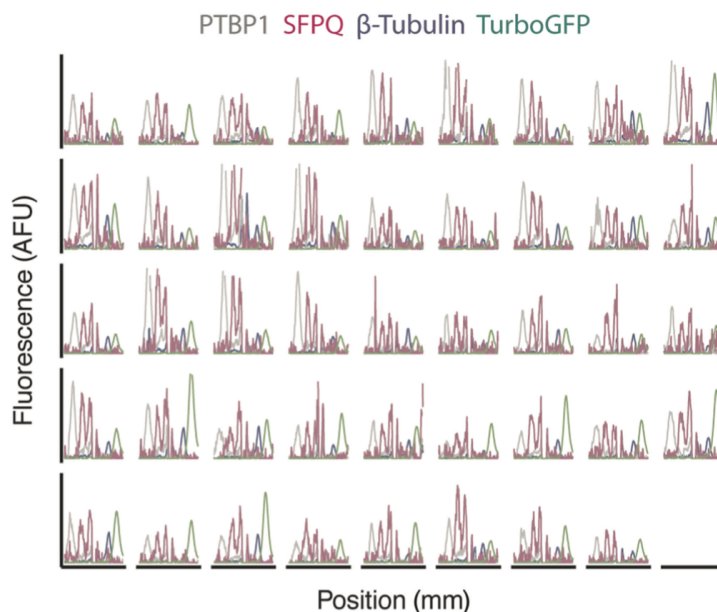
Figure 2.6: Montage of fluorescence intensity distributions for spliceosome protein targets from concurrent analysis of 44 TurboGFP-expressing U373 cells.

NF-κB translocation dynamics

Protein subcellular localization is dynamic. In one established example, stimulation of mammalian cells by LPS found in the outer membrane of Gram-negative bacteria is known to elicit a strong translocation response from the transcription factor family nuclear factor NF-κB. [52] A wide range of downstream processes (for example, cancer progression, inflammation response, and the interplay between innate and adaptive immune systems) are influenced by NF-κB signaling state. [53, 54]

To monitor NF-κB signaling during LPS stimulation without artifact-inducing fixation8,9, we stimulated naive U373 cells with LPS (5 g mL^{-1} for 0120 min) and measured the nucleocytoplasmic distribution of NF-κB in each cell using both the (sc)^{2}WB and ICC. We observed an increase in nuclear NF-κB upon stimulation with LPS (Figures 2.7a and b) with a time-to-peak of 60 min as determined by the (sc)^{2}WB and corroborated by gold-standard ICC assays. Furthermore, we calculated the correlation between the median of the NF-κB distribution medians measured by the (sc)^{2}WB and ICC and found appreciable correlation at every time point ($\rho = 0.90$, Figure 2.7b). The deviation of the fit line from a slope of 1.0 and a y-intercept at the origin is consistent with the skew toward nuclear localization measured by the (sc)^{2}WB (Figure 2.7f). Further investigation of the nuclear skew of the distribution is ongoing. Whereas the dynamics of NF-κB translocation are LPS preparation-dependent, the behavior reported by the (sc)^{2}WB agrees with the dynamics reported in the literature (Figures 2.7c and d)6. Using the 6-h (sc)^{2}WB assay, we monitored NF-κB translocation

in 1247 individual cells, roughly double the number of cells measured using an overnight ICC assay (Figure 2.7e). Ready scale-up of single-cell protein assays to large populations of cells is important because the measurement throughput establishes statistical confidence by enhancing confidence in distribution estimators.
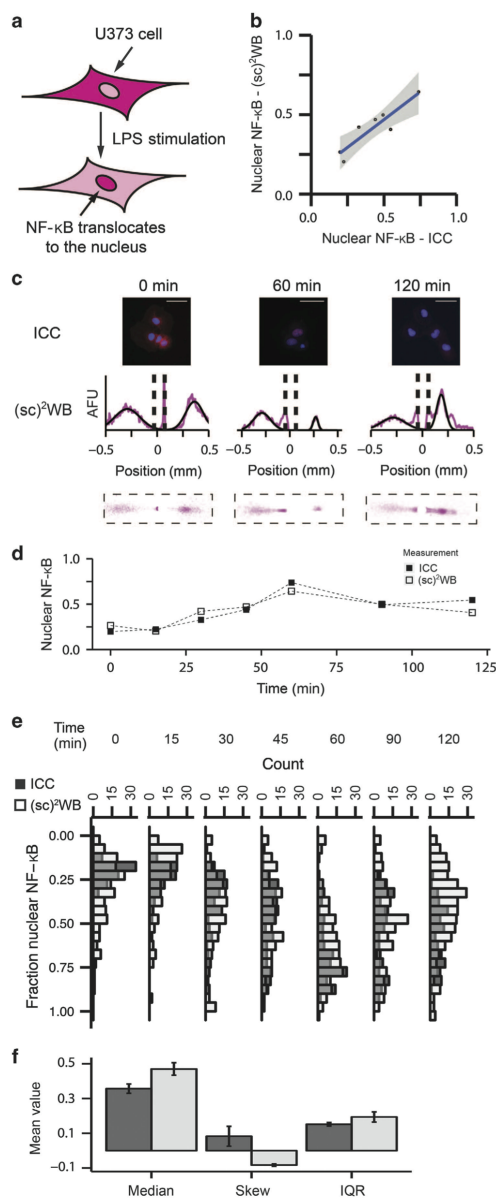
Figure 2.7: Monitoring dynamic changes in NF-κB localization using the (sc)^{2}WB. (**a**) The nucleocytoplasmic distribution of NF-κB changes in response to stimulation with LPS. (**b**) The median localization of NF-κB for each time point as measured by ICC (x axis) and the (sc)^{2}WB (y axis) correlate with $\rho = 0.90$. Nuclear NF-κB=AUC$_{nuc}$/AUC$_{total}$. The gray region indicates the 95% confidence interval. (**c**) False-color fluorescence micrographs from ICC and (sc)^{2}WB analysis of U373 cells at different times after LPS stimulation (U373 cells, 5 g mL^{-1} LPS). Magenta traces on the (sc)^{2}WB intensity profiles are the raw signal and the black traces are the Gaussian fits. Dashed lines denote the microwell border. (**d**) The median fluorescence signal (AUC) from NF-κB in the nucleus is determined by ICC and (sc)^{2}WB, and reports a similar time-to-peak and translocation trend. (**e**) Histograms of nuclear NF-κB expression over the time course by both ICC and (sc)^{2}WB. (**f**) Localization distribution parameters from ICC (n=4 wells) and (sc)^{2}WB (n=3 devices). Error bars are ± 1 s.d. ICC, immunocytochemistry; LPS, lipopolysaccharide; s.d., standard deviation

We next sought to estimate the technical variation in the (sc)^{2}WB assay using the NF-κB model system. Establishing sources of variance is particularly difficult in end point single-cell measurements because the same cell cannot be assayed multiple times (that is, no true technical replicates). Thus, we performed (sc)^{2}WB replicates on cells sampled from the same starting population and compared with ICC. In comparing with ICC we considered three metrics: median, nonparametric skew, and IQR for the (sc)^{2}WB-reported NF-κB expression and localization distribution (Figure 2.7f). These distribution metrics are nonparametric; thus, they do not assume a specific form of the NF-κB expression or localization distribution. In the first metric, the CV of the distribution median indicates how reproducibly the assay reports the center of the expression distribution, with the (sc)^{2}WB reporting a value within 3% of ICC.

As a second metric, the nonparametric skew, S, provides a measure of the asymmetry of a distribution, where $S = (\mu - \nu)/\sigma$ where μ is the mean, ν is the median, and σ is the s.d. We observed the skew of the NF-kB distribution by (sc)^{2}WB to be: (i) more negative than ICC ($S_{ICC} = 0.0835 \pm 0.0569$, n = 4 wells, $S_{(sc)2WB} = 0.0840 \pm 0.077$, n = 3 devices) and (ii) less variable than ICC ($CV_{ICC} = 68.1\%$, n = 4 wells, $CV_{(sc)2WB} = 9.14\%$, n = 3 devices). A more negative skew (toward the nuclear proteins) suggests predominantly nuclear localization, whereas a more positive skew suggests more cytoplasmic localization. We do not attribute the more nuclear skew to the localization to poor solubilization of the cytoplasmic NF-κB because we did not observe cross- contamination of proteins in the cytosol (that is, TurboGFP and β-tubulin). Thus, the (sc)^{2}WB may reduce technical variance by spatially separating the subcellular fractions, eliminating the need for fixation and separating out confounding background signals. Furthermore, the (sc)^{2}WB may enhance access to nuclear proteins (Figure 2.7f), perhaps owing to a reduction in fixation-induced artifacts. [8] In ICC, observed localization is dependent on both the fixation method [55] (that is, concentration and choice of fixative) and permeabilization method. [8] In addition, fixation is known to dehydrate cellular proteins and impart structural alternations. [56, 57] Further, antibody cross-reactivity leads to spurious localization. [9] The (sc)^{2}WB circumvents localization artifacts caused by the fixation and permeabilization in ICC by spatially separating the subcellular compartments through DDF and PAGE, thus providing a higher-fidelity measurement of the nucleocytoplasmic distribution of proteins in single cells.

Comparing the IQR of the ICC and (sc)^{2}WB compares the measured heterogeneity in the same cell population; with a larger IQR, the cell population is more heterogeneous. The (sc)^{2}WB reported an IQR 20% larger than ICC ($IQR_{(sc)2WB} = 19.4\%$ and $IQR_{ICC} = 15.2\%$). The larger measured IQR in the (sc)^{2}WB could be due to the larger number of samples ($n_{(sc)2WB} = 1093$, $n_{ICC} = 676$) enabled by the rapid, parallel nature of the assay, allowing the detection of rare events.

Using NF-κB as a model system, (sc)^{2}WB measured the dynamic translocation of NF-κB from the cytoplasm to the nucleus at 15min intervals. Furthermore, the (sc)^{2}WB exhibited reduced technical variation in the measured distribution while measuring 61.7% more cells than ICC. We hypothesize that the reduced technical variation is due to the elimination of fixation and the electrophoretic separation of our target analyte (NF-κB) from the back-

ground signal. By reducing technical variation, improving accessibility to nuclear proteins, and increasing throughput, the $(sc)^2WB$ enables measurement of smaller differences in the nucleocytoplasmic distribution of proteins in single cells, a critical parameter in understanding protein signaling. While reducing technical variation, the fractionation strategy implemented in the $(sc)^2WB$ is optimized to resolve protein localization to the cytoplasmic and nuclear compartments. Future work will refine the lysis buffers to increase the resolution of the fractionation. The increased throughput and reduced technical variance of the $(sc)^2WB$ enables the detection of more subtle and rare events in heterogeneous cell populations.

2.4 Conclusions

The subcellular localization of proteins can markedly impact cellular function. Although single-cell immunoassays do exist, detection selectivity and throughput remain analytical challenges. The studies detailed here introduce a subcellular resolution western blot assay that confers detection selectivity beyond that of simple immunoassays with a throughput of 103 cells per 6 h assay. Precise microfluidic control of mass transport allows the detection of proteins in the cytoplasm and nucleus in each cell assayed. Immunoblotting and western blots derive detection selectivity enhancements from the integration of a separation stage before the antibody-based detection stage. Here, in the subcellular western blot assay, the two-parameter assay acts to spatially segregate the confounding background signal from the target signal (which has an impact on target multiplexing in ICC) and translates into robust signal analysis using objective peak detection and not complex image segmentation algorithms that require subjective manual input.

Three distinguishing technology contributions make single-cell western blotting with subcellular resolution possible: (1) the development and validation of a pair of orthogonal lysis buffers to differentially lyse the cytoplasm and then the nucleus of each cell while also functioning as an electrophoresis buffer (that is, optimized detergent concentration for rapid solubilization while minimizing conductivity and selected buffering species offering low conductivity and high protein mobility); (2) the design and fabrication of a multilayer device for serial and synchronized, quiescent diffusion-based application of lysis buffers across a large microwell array; and (3) the design and validation of a bi-directional PAGE assay designed to independently measure and spatially segregate target protein expression in the cytoplasmic and then the nuclear fraction. To ensure broad relevance, we validated the tool on a well-characterized panel of protein targets with known subcellular distributions and then applied the tool to analyze a large proteinRNA complex (spliceosome) and a dynamic translocation (NF-κB).

By harnessing the physics available in miniaturized systems, this is (to our knowledge) the first report of protein separations on multiple subcellular compartments of the same single cell. Compared with existing single-cell protein separations, the subcellular western blot assay surpasses peak capacities, resolving power, and throughput. The bi-directional PAGE format enhances both the peak capacity and resolving power with three fully resolved

proteins blotted in a 1 mm separation distance including the resolution of a 7 kDa mass difference (β-tubulin and PTBP1; 12% mass difference).

Furthermore, using an electrophoretic separation to spatially segregate the cytoplasmic and nuclear compartments enhances selectivity over single-stage immunoassays, including ICC. Separating the subcellular compartments obviates the need for fixation and image segmentation algorithms, both sources of variance and potentially spurious results. In addition, the electrophoretic protein separation identifies targets by both electrophoretic mobility and immunoaffinity. As hypothesized and supported by the technical variance analysis described here, the $(\text{sc})^2\text{WB}$ appears less sensitive to both off-target background signal and cell fixation conditions (having no fixation in the microfluidic assay) than ICC. In reducing the technical variance and eliminating fixation artifacts, the $(\text{sc})^2\text{WB}$ should more accurately measure the nucleocytoplasmic distribution of proteins in single cells than ICC.

Looking forward, we envision integrating the phenotypic characterization of each cell with the end point nucleocytoplasmic protein-profiling assays described here. Ongoing research is being conducted on both diversifying and optimizing the DDF lysis buffer chemistries to scrutinize an even wider range of subcellular compartments and organelles. Active settling methods, such as the convection driven seating of microparticles into porous microwells [58], may increase the throughput of the $(\text{sc})^2\text{WB}$, allowing for the detection of rare cells. Further increasing the subcellular resolution of the $(\text{sc})^2\text{WB}$ will deepen our understanding of how protein translocation drives protein signaling in processes such as cancer metastasis and stem cell differentiation.

References

1. Durmus, N. G. *et al.* Magnetic levitation of single cells. *Proceedings of the National Academy of Sciences* **112,** E3661–E3668 (July 2015).

2. Ribeiro, A. J. S. *et al.* Contractility of single cardiomyocytes differentiated from pluripotent stem cells depends on physiological shape and substrate stiffness. *Proceedings of the National Academy of Sciences* **112,** 12705–12710 (Oct. 2015).

3. Karin, M. How NF-kappaB is activated: the role of the IkappaB kinase (IKK) complex. *Oncogene* **18,** 6867–6874 (Nov. 1999).

4. Barry, E. R. & Camargo, F. D. The Hippo superhighway: signaling crossroads converging on the Hippo/Yap pathway in stem cells and development. *Current Opinion in Cell Biology* **25,** 247–253 (Apr. 2013).

5. Tay, S. *et al.* Single-cell NF-κB dynamics reveal digital activation and analogue information processing. *Nature* **466,** 267–271 (Aug. 2010).

6. Gutschow, M. V. *et al.* Single-Cell and Population NF-κB Dynamic Responses Depend on Lipopolysaccharide Preparation. *PLoS One* **8,** e53222 (Jan. 2013).

7. Chen, J. *et al.* Single-Molecule Dynamics of Enhanceosome Assembly in Embryonic Stem Cells. *Cell* **156,** 1274–1285 (Mar. 2014).

8. Schnell, U. U., Dijk, F. F., Sjollema, K. A. K. & Giepmans, B. N. G. B. Immunolabeling artifacts and the need for live-cell imaging. *Nature Methods* **9,** 152–158 (Jan. 2012).

9. Stadler, C. *et al.* Immunofluorescence and fluorescent-protein tagging show high correlation for protein localization in mammalian cells. *Nature Methods* **10,** 315–323 (Feb. 2013).

10. Chalfoun, J. *et al.* FogBank: a single cell segmentation across multiple cell lines and image modalities. *BMC bioinformatics* **15,** 431 (2014).

11. Carpenter, A. E. *et al.* CellProfiler: image analysis software for identifying and quantifying cell phenotypes. *Genome biology* **7,** R100–R100 (Jan. 2006).

12. Drissi, R., Dubois, M.-L. & Boisvert, F.-M. Proteomics methods for subcellular proteome analysis. *FEBS Journal* **280,** 5626–5634 (Sept. 2013).

13. Ramsby, M. & Makowski, G. Differential detergent fractionation of eukaryotic cells. *Cold Spring Harbor Protocols* **2011,** prot5592 (Mar. 2011).

14. Kirkpatrick, F. H., Gordesky, S. E. & Marinetti, G. V. Differential solubilization of proteins, phospholipids, and cholesterol of erythrocyte membranes by detergents. *Biochimica et Biophysica Acta (BBA) - Biomembranes* **345,** 154–161 (1974).

15. Lee, J. K., Kim, S., Nam, H. G. & Zare, R. N. Microdroplet fusion mass spectrometry for fast reaction kinetics. *Proceedings of the National Academy of Sciences* **112,** 3898–3903 (Mar. 2015).

16. Fu, Y. *et al.* Uniform and accurate single-cell sequencing based on emulsion whole-genome amplification. *Proceedings of the National Academy of Sciences* **112,** 11923–11928 (Sept. 2015).

17. Hu, S., Zhang, L., Cook, L. M. & Dovichi, N. J. Capillary sodium dodecyl sulfate-DALT electrophoresis of proteins in a single human cancer cell. *ELECTROPHORESIS* **22,** 3677–3682 (Oct. 2001).

18. Kennedy, R. T., Oates, M. D., Cooper, B. R. & Nickerson, B. Microcolumn separations and the analysis of single cells. *Science* (1989).

19. Cruz, L., Moroz, L. L., Gillette, R. & Sweedler, J. V. Nitrite and nitrate levels in individual molluscan neurons: single-cell capillary electrophoresis analysis. *Journal of neurochemistry* **69,** 110–115 (July 1997).

20. Dickinson, A. J., Armistead, P. M. & Allbritton, N. L. Automated Capillary Electrophoresis System for Fast Single-Cell Analysis. *Analytical Chemistry,* 130409154751001 (Apr. 2013).

21. Mellors, J. S., Jorabchi, K., Smith, L. M. & Ramsey, J. M. Integrated Microfluidic Device for Automated Single Cell Analysis Using Electrophoretic Separation and Electrospray Ionization Mass Spectrometry. *Analytical Chemistry* **82,** 967–973 (Feb. 2010).

22. Huang, B. *et al.* Counting low-copy number proteins in a single cell. *Science* **315,** 81–84 (Jan. 2007).

23. Kuriyama, K., Shintaku, H. & Santiago, J. G. Isotachophoresis for fractionation and recovery of cytoplasmic RNA and nucleus from single cells. *ELECTROPHORESIS* **36,** 1658–1662 (May 2015).

24. Wood, D. K., Weingeist, D. M. & Bhatia, S. N. *Single cell trapping and DNA damage analysis using microwell arrays* in *Proceedings of the National Academy of Sciences of the United States of America* (2010).

25. Hughes, A. J. *et al.* Single-cell western blotting. *Nature Methods* **11,** 749–755 (June 2014).

26. Kang, C.-C., Lin, J.-M. G., Xu, Z., Kumar, S. & Herr, A. E. Single-Cell Western Blotting after Whole-Cell Imaging to Assess Cancer Chemotherapeutic Response. *Analytical Chemistry* **86,** 10429–10436 (Oct. 2014).

27. Kang, C.-C., Yamauchi, K. A., Vlassakis, J. & Sinkala, E. Single cell-resolution western blotting. *Nature Protocols* (2016).

28. Duncombe, T. A., Kang, C.-C., Maity, S. & Ward, T. M. Hydrogel Pore-Size Modulation for Enhanced Single-Cell Western Blotting. *Advanced . . .* (2016).

29. Tentori, A. M., Yamauchi, K. A. & Herr, A. E. Detection of Isoforms Differing by a Single Charge Unit in Individual Cells. *Angewandte Chemie International Edition* **55,** 12431–12435 (Sept. 2016).

30. Stepanenko, A. A. & Kavsan, V. M. Karyotypically distinct U251, U373, and SNB19 glioma cell lines are of the same origin but have different drug treatment sensitivities. *Gene* **540,** 263–265 (May 2014).

31. Song, Z., Ghochani, M., McCaffery, J. M., Frey, T. G. & Chan, D. C. Mitofusins and OPA1 mediate sequential steps in mitochondrial membrane fusion. *Molecular Biology of the Cell* **20,** 3525–3532 (Aug. 2009).

32. Li, J. J., Bickel, P. J. & Biggin, M. D. System wide analyses have underestimated protein abundances and the importance of transcription in mammals. *PeerJ* **2,** e270 (2014).

33. Leaist, D. G. A moving-boundary technique for the measurement of diffusion in liquids. triton X-100 in water. *Journal of solution chemistry* (1991).

34. Linke, D. Detergents: an overview. *Methods in enzymology* **463,** 603–617 (2009).

35. Schwartz, R., Ting, C. S. & King, J. Whole proteome pI values correlate with subcellular localizations of proteins for organisms within the three domains of life. *Genome Research* **11,** 703–709 (Apr. 2001).

36. Niepmann, M. & Zheng, J. Discontinuous native protein gel electrophoresis. *ELEC-TROPHORESIS* **27,** 3949–3951 (Oct. 2006).

37. Hughes, A. J., Lin, R. K., Peehl, D. M. & Herr, A. E. Microfluidic integration for automated targeted proteomic assays. *Proceedings of the National Academy of Sciences of the United States of America* **109,** 5972–5977 (2012).

38. Berezney, R. & Coffey, D. S. Nuclear matrix. Isolation and characterization of a framework structure from rat liver nuclei. *Journal of Cell Biology* **73,** 616–637 (June 1977).

39. Aaronson, R. P. & Blobel, G. Isolation of nuclear pore complexes in association with a lamina. *Proceedings of the National Academy of Sciences of the United States of America* **72,** 1007–1011 (Mar. 1975).

40. Talcott, B. & Moore, M. S. Getting across the nuclear pore complex. *Trends in Cell Biology* **9,** 312–318 (Aug. 1999).

41. Peters, R. Fluorescence microphotolysis to measure nucleocytoplasmic transport and intracellular mobility. *Biochimica et biophysica acta* **864,** 305–359 (Dec. 1986).

42. Huang, B., Wang, W., Bates, M. & Zhuang, X. Three-dimensional super-resolution imaging by stochastic optical reconstruction microscopy. *Science-AAAS-Weekly Paper Edition* **319,** 810–813 (Feb. 2008).

43. O'Farrell, P. H. High resolution two-dimensional electrophoresis of proteins. *Journal of Biological Chemistry* (1975).

44. Shi, Q. Q. *et al.* Single-cell proteomic chip for profiling intracellular signaling pathways in single tumor cells. *Proceedings of the National Academy of Sciences of the United States of America* **109,** 419–424 (Jan. 2012).

45. Stack, E. C., Wang, C., Roman, K. A. & Hoyt, C. C. Multiplexed immunohistochemistry, imaging, and quantitation: A review, with an assessment of Tyramide signal amplification, multispectral imaging and multiplex analysis. *Methods* **70,** 46–58 (Nov. 2014).

46. Hsu, T. Y. T. *et al.* The spliceosome is a therapeutic vulnerability in MYC-driven cancer. *Nature* **525,** 384–388 (Sept. 2015).

47. Patton, J. G., Mayer, S. A., Tempst, P. & Nadal-Ginard, B. Characterization and molecular cloning of polypyrimidine tract-binding protein: a component of a complex necessary for pre-mRNA splicing. *Genes & Development* **5,** 1237–1251 (July 1991).

48. Patton, J. G., Porro, E. B., Galceran, J., Tempst, P. & Nadal-Ginard, B. Cloning and characterization of PSF, a novel pre-mRNA splicing factor. *Genes & Development* **7,** 393–406 (Mar. 1993).

49. Ke, Y. *et al.* Tau-Mediated Nuclear Depletion and Cytoplasmic Accumulation of SFPQ in Alzheimer's and Pick's Disease. *PLoS One* **7,** e35678 (Apr. 2012).

50. Ji, Q. *et al.* Long non-coding RNA MALAT1 promotes tumour growth and metastasis in colorectal cancer through binding to SFPQ and releasing oncogene PTBP2 from SFPQ/PTBP2 complex. *British Journal of Cancer* **111,** 736–748 (July 2014).

51. Meissner, M. *et al.* Differential nuclear localization and nuclear matrix association of the splicing factors PSF and PTB. *Journal of Cellular Biochemistry* **76,** 559–566 (Jan. 2000).

52. Barton, G. M. & Medzhitov, R. Toll-like receptor signaling pathways. *Science* **300,** 1524–1525 (June 2003).

53. Karin, M. & Greten, F. R. NF-κB: linking inflammation and immunity to cancer development and progression. *Nature Reviews Immunology* **5,** 749–759 (Sept. 2005).

54. Gerondakis, S., Fulford, T. S., Messina, N. L. & Grumont, R. J. NF-κB control of T cell development. *Nature Immunology* **15,** 15–25 (Dec. 2013).

55. Berod, A., Hartman, B. K. & Pujol, J. F. Importance of fixation in immunohistochemistry: use of formaldehyde solutions at variable pH for the localization of tyrosine hydroxylase. *Journal of Histochemistry & Cytochemistry* **29,** 844–850 (July 1981).

56. Hoetelmans, R. W. *et al.* Effects of acetone, methanol, or paraformaldehyde on cellular structure, visualized by reflection contrast microscopy and transmission and scanning electron microscopy. *Applied immunohistochemistry & molecular morphology : AIMM / official publication of the Society for Applied Immunohistochemistry* **9,** 346–351 (Dec. 2001).

57. Shibata, T., Tanaka, T., Shimizu, K., Hayakawa, S. & Kuroda, K. Immunofluorescence imaging of the influenza virus M1 protein is dependent on the fixation method. *Journal of Virological Methods* **156,** 162–165 (Jan. 2009).

58. Kim, J. J., Bong, K. W., Reátegui, E., Irimia, D. & Doyle, P. S. Porous microwells for geometry-selective, large-scale microparticle arrays. *Nature Materials* **16,** 139–146 (Sept. 2016).

Chapter 3

Detection of Isoforms Differing by a Single Charge Unit in Individual Cells

3.1 Abstract

To measure protein isoforms in individual mammalian cells, we report single-cell resolution isoelectric focusing (scIEF) and high-selectivity immunoprobing. Microfluidic design and photoactivatable materials establish the tunable pH gradients required by IEF and precisely control the transport and handling of each 17-pL cell lysate during analysis. The scIEF assay resolves protein isoforms with resolution down to a single-charge unit, including both endogenous cytoplasmic and nuclear proteins from individual mammalian cells.

3.2 Introduction

Questions linger regarding how genome and transcriptome variations manifest as functional proteomes, especially among populations of individual cells.[1, 2] Functional proteomes are dictated by dynamic protein expression, as well as chemical modifications and splice variants of the expressed proteins. These chemical modifications yield protein variants (proteoforms) with unique functions.[3] Nucleic acid measurements (for example, RNA-seq) fundamentally cannot measure specific proteoforms (that is, post-translational modifications and alternative splicing). However, direct measurement of proteins in single cells, predominantly by immunoassays,[4–6] is limited by both the availability and selectivity of immunoreagents (for example, antibodies).[7] Challenges in the generation of proteoform-specific antibodies limit our understanding of the roles proteoforms play. Surmounting this cytometry bottleneck requires the introduction of new tools optimized for proteoform analysis.[8]

Mass spectrometry is currently the workhorse technology for proteomic analysis. Bottom-up mass spectrometry digests proteins into peptides and identifies proteins and post-translational modifications from the mass spectra of the peptides.[9] However, owing to the digestion of proteins into peptides, it is challenging to determine how the modified peptides relate back to the intact proteins (for example, one proteoform with many modifications or multiple proteoforms with fewer modifications).[10] Top-down mass spectrometry can identify and measure specific proteoforms by using separations to reduce the sample complexity and avoid digestion of the proteins of interest.[11] While mass spectrometry is able to identify and quantify specific proteoforms, the analytical sensitivity is insufficient for single-cell proteoform cytometry.[11, 12]

As a complimentary approach to mass spectrometry, microfluidic separations facilitate the selective profiling of proteoforms in single cells. In recent work, polyacrylamide gel electrophoresis (PAGE) was combined with a subsequent immunoassay for single-cell western blotting.[13] Although western blotting is a high-selectivity protein assay, post-translational modifications and alternative splicing do not always yield resolvable molecular mass differences. Fortunately, even proteoforms of similar mass often exhibit isoelectric point (pI) differences that are readily detectable with another electrophoretic assay, namely, isoelectric focusing (IEF).[14] Capillary IEF followed by immunoblotting has resolved protein post-translational modifications in lysates pooled from as few as 25 cells.[15]

To separate proteins by pI, IEF employs protein electromigration along a stable pH gradient.[16] Proteins electromigrate until each species enters a region of the pH gradient in which the local pH is equal to the pI of that species; at that location, the proteoform has no net mobility. Electromigration therefore halts and the protein is focused. IEF has immense resolving power and selectivity; even single-charge differences among proteoforms are detectable.[17]

To extend the power of IEF from pooled lysates to individual cells, we designed a 3D microfluidic device that integrates all preparatory and analytical stages for single-cell IEF with in-gel immunoprobing (cell isolation, lysis, IEF, UV-actuated blotting, and probing). Microfluidic integration is essential to overcoming diffusion-based dilution of the lysate from a single cell. This dilution is a loss mechanism that is exacerbated by sample handling in multi-stage assays, including immunoblotting. Although proteins can have appreciable intracellular concentrations (ca. 20nm in a 30μm diameter cell),[18, 19] a diffusion time of 5s can reduce the maximum protein concentration by 90% (see Supporting Information). Microfluidic integration minimizes the time allowed for diffusion-driven dilution, thus making isoform detection by electrophoretic analysis of single-cell lysates possible.

3.3 Methods

Reagents and Materials

3-(Trimethoxysilyl)propyl methacrylate (98%), acetic acid (glacial, 99.7%, ACS grade), methanol (anhydrous, 99.8%), sodium hydroxide (NaOH, 97.0%, ACS grade), acrylamide / bis-acrylamide solution (29:1, electrophoresis grade), N,N,N',N' -tetramethylethylenediamine (TEMED, BioReagent, 99%), ammonium persulfate (APS, ACS reagent, $\geq$98.0%), 3- [(3- Cholamido-propyl)dimethylammonio] -1-propanesulfonate (CHAPS, $\geq$ 98%, electrophoresis grade), digitonin (Used as non-ionic detergent), TritonTM X-100 detergent (laboratory grade), sodium dodecyl sulfate (SDS, BioReagent, $\geq$ 98.5% (w/v), suitable for electrophoresis and molecular biology), β-mercaptoethanol, urea (BioReagent), thiourea (ACS reagent, $\geq$ 99.0%), Poly-buffer 74 (PB74), Polybuffer 96 (PB96), Immobilines, and fluorescent IEF markers were acquired from Sigma Aldrich (St. Louis, MO). The fluorescent pH markers used were pI 4.5 (1 mg mL^{-1} in 5mM HCl), pI 5.5 (3 mg mL^{-1} in 15 mM HCl),and pI 6.8 (1 mg mL^{-1} in 5mM HCl). The Immobilines used were acrylamido buffer pKa 3.6 (0.2 M in water) and acrylamido buffer pKa 9.3 (0.2 M in 1-propanol). Polybuffers can be used as a substitute for other carrier ampholytes such as Biolyte, Ampholine, Pharmalyte, and Servalyte, at a fraction of the cost.[20, 21]

UV photoinitiator VA-086 was purchased from Wako Chemicals (Richmond, VA). Trypsin: Ethylenediaminetetraacetic acid (EDTA) solution (0.05% trypsin and 0.53 mM EDTA) was acquired from Gemini Bio-Products (Sacramento, CA). 10x Phosphate-Buffered Saline (PBS) solution (pH 7.4, MCB grade) was obtained from Mediatech (Manassas, VA). Tris-buffered saline with Tween 20 (TBST) was bought from Santa Cruz Biotechnology (Santa Cruz, CA). Tris-HCL (pH 6.9) was purchased from Teknova (Holllister, CA). N-[3-[(3- ben-zoylphenyl)formamido]propyl] methacrylamide (BPMAC) monomer was custom synthesized by PharmAgra Laboratories (Brevard, NC).[22] Purified recombinant wild-type GFP from Aequorea victoria (wtGFP) was sourced from Clontech (632373, Mountain View, CA). Purified recombinant TurboGFP (tGFP) was sourced from Evrogen (FP552, Moscow, Russia). Primary antibodies used in this study include rabbit anti-TurboGFP (1:30, PA5-22688, Pierce Antibody Products, Rockford, IL), mouse anti-lamin A/C (1:5, mab636, Pierce Antibody Products), and rabbit anti-β-Tubulin (1:10, mab6046, Abcam, Cambridge, United Kingdom). The secondary antibodies used in this study were AlexaFluor 555-labeled donkey anti-mouse IgG (1:30, A-31570) and AlexaFluor 647-labeled donkey anti-rabbit IgG (1:30, A-31573) sourced from Life Technologies (Grand Island, NY).

Cells Lines and Cell Culture

U373 MG human glioblastoma cells provided by collaborators in the Kumar Laboratory at UC Berkeley were obtained from the American Type Culture Collection via the UC Berkeley Tissue Culture facility and were stably transduced with tGFP by lentiviral infection (multiplicity of infection = 10).[22] The tGFP expressing U373 MG (U373-tGFP) cells

were cultured in-house in high glucose DMEM (Life Technologies) supplemented with 1 mM sodium pyruvate (Life Technologies), 1x MEM non-essential amino acids (Life Technologies), 1% penicillin and streptomycin, and 10% fetal bovine serum (JR Scientific, Woodland, CA). Cells were grown at 37 °C with 5% CO2 in a humidified incubator. Prior to the experiment, cells were trypsinized, resuspended in 1x PBS, and kept on ice. The ATCC U373 MG cells have been found to share a common origin with U251 and SNB19 glioma cells. However, they have since diverged and are karyotypically distinct.[23]

Device Fabrication

The first component of the single-cell isoelectric focusing (scIEF) device is the bottom layer, which is a standard microscope slide, coated with a 40 μm thick film of large pore-size 6%T (3.3%C) polyacrylamide gel containing 5 mM BPMAC. Unlike western blotting, IEF does not require molecular sieving through the polyacrylamide gel matrix.[24, 25] In lieu of sieving, the thin polyacrylamide gel bottom layer functions as an anti-convective medium, contains the microwells for cell containment, and, in immunoprobing, acts as a scaffold on which protein peaks are immobilized (blotted). A row of 32 μm diameter microwells spaced 500 μm apart was molded into this thin polyacrylamide film using SU-8 wafers as molds and chemical polyacrylamide gel polymerization, as previously described.[13, 22] Importantly, the x-axis position of the microwells was moved to be closer to the pI of the proteins when faster focusing was desired or away from the pI of the proteins to avoid proteins focusing on the microwells (Table 3.1). wtGFP at a concentration of 10 $\mu g\,mL^{-1}$ and pH markers at 1:100 dilutions were included in the bottom layer precursor solution as pH markers when specified (Table 3.1). Covalent attachment of the polyacrylamide gel to plain glass microscope slides (VWR International, Radnor, PA) was achieved by acrylate-terminated silane monolayer formation using previously described methods.[13, 22, 26] Slides were used whole or cut to desired dimensions using a diamond scribe (Ted Pella Inc, Redding, CA) and Running and Nipping Pliers (Fletcher, East Berlin, CT). SU8 2025 photoresist (MicroChem, Westborough, MA) molds on silicon wafers (University Wafer, Boston, MA) were fabricated as previously described.[13, 26]

Table 3.1: scIEF experimental conditions. Microwell position along the x-axis was measured from the catholyte-side edge of the bottom gel. The focusing region was 9 mm wide along the focusing direction (x-axis) and a potential difference of 600 V was applied in all experiments.

data sets	pH range	well position (mm)	lysis time (s)	voltage application time (min)	lysis reagents	sample
1d, S2	4-9	4.50	60	5.5	native	U373-tGFP cells
1e, S6a	4-7	6.75	30	6.0	native	U373-tGFP cells
S3	4-7	2.25	30	6.0	native	U373-tGFP cells
2b, S5	4-9	N/A	N/A	10.0	native	*wt*GFP
S7	4-9	N/A	N/A	5.0	native	tGFP
2c	4-7	N/A	N/A	10.0	native	pH markers
3a, S6b	4-7	2.25	30	6.0	native	U373-tGFP cells
3b, S6c	4-7	2.25	30	6.0	denaturing	U373-tGFP cells
3e, S6d	4-7	2.25	30	6.0	denaturing	U373-tGFP cells

The second component of the scIEF device is the chemically functionalized lid. The heterogeneous gel lid is a chemically patterned 500 μm thick polyacrylamide gel layer that performs two functions: (i) delivery of lysis and IEF reagents to the bottom layer and (ii) serves as a template for the pH and electric potential gradients required for IEF. The free-standing 15%T (3.3%C) polyacrylamide gel lids were fabricated using a multistep photopolymerization method (Figure 3.1). Polyacrylamide gel precursor was loaded between glass surfaces rendered hydrophobic with Gel Slick (Lonza, Rockland, ME). Lid thickness was specified using 500 μm thick, 9 mm wide spacers obtained from C.B.S. Scientific (Del Mar, CA). The three distinct regions were formed using sequential photopatterning and precursor solution wash steps (Figure 3.2). The focusing region containing the carrier ampholytes and lysis reagents was flanked by gels containing Immobilines serving as the catholyte and anolyte boundaries. [27] The basic and acidic regions in the gel lid contained combinations of Immobilines to buffer at acidic and basic pH values.[27] Using patterned polyacrylamide gel regions containing Immobilines obviated the use of liquid buffers, which if introduced into the focusing region, would disrupt pH gradient formation. The width of the focusing region was specified using the spacers as molds. Because the carrier amphololytes and lysis reagents in the focusing region were not immobilized, the focusing region was polymerized shortly before running the assay, in order to avoid excessive diffusion of these reagents to the catholyte and anolyte regions. The focusing region in the gel contained 1:10 dilutions of PB74 and PB96 as the carrier ampholytes, and 3.6% (w/v) CHAPS, 1% (v/v) Triton x-100, and 0.0125% (w/v) digitonin as detergents for cell lysis and protein solubilization, as specified (Table 3.2). Chaotropes (7 M urea, 2 M thiourea) were added for scIEF with denaturing conditions (Table 3.1).[28, 29] UV excitation for gel photopolymerization was provided by an OAI Model 30 Collimated UV light source (San Jose, CA). 4 min exposure times at 20 mW cm-2 powers attenuated through a 390 nm longpass UV filter (Edmund Optics, Barrington, NJ) were used.
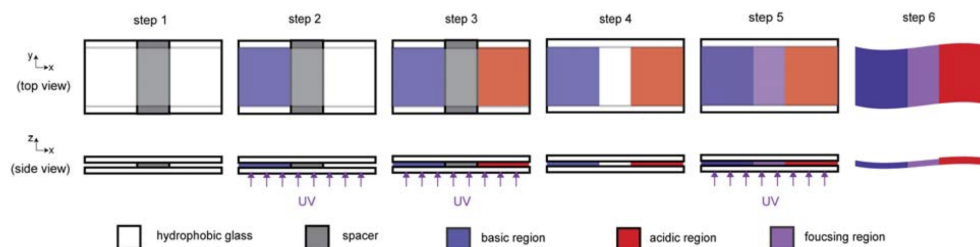
Figure 3.1: scIEF gel lid fabrication. Step 1: a 0.5 mm thick spacer that is the width of the focusing region is placed between two hydrophobic glass plates. The glass plates are sized such that they match the size of the gel lid. Step 2: the basic gel precursor is introduced between the glass plates on the basic boundary of the gel lid. The basic gel is polymerized with UV light. Step 3: the unpolymerized basic catholyte gel precursor is washed out and the acidic anolyte precursor is introduced to the other side and similarly photopolymerized. Step 4: the spacer is removed. Step 5: the focusing region precursor is introduced and polymerized. Step 6: the glass slides are removed leaving a free-standing gel structure.

Table 3.2: scIEF polyacrylamide gel precursor solution compositions. Carrier ampholyte and lysis reagent composition was varied for different experiments, as specified. Because ionic detergents such as SDS are incompatible with IEF, chaotropes were added to the focusing gel region for denaturing conditions in addition to the detergents used for native conditions. The anolyte region had pH < 3.3 and catholyte region had pH > 10.1. pH measurements were done with a Twin Compact pH Meter (Horiba Scientific, Edison, NJ).

	anolyte region gel lid	catholyte region gel lid	focusing region gel lid	bottom layer
gel composition	15%T (3.3%C) Immobilines: 13.6 mM pKa 3.6 6.4 mM pKa 9.3	15%T (3.3%C) Immobilines: 14.4 mM pKa 9.3 5.6 mM pKa 3.6	15%T (3.3%C)	6%T (3.3%C) 5 mM BPMAC
carrier ampholytes	-	-	PB74 1:10 (v/v) PB 96 1:10 (v/v)	-
detergents (native)	-	-	3.6% (w/v) CHAPS 1% (v/v) Triton x-100 0.0125% (w/v) digitonin	-
chaotropes (denaturing)			7 M urea 2 M thiourea	
initiators	0.2% (w/v) VA-086	0.2% (w/v) VA-086	0.2% (w/v) VA-086	0.08% (v/v) TEMED 0.08% (w/v) APS

Experimental Protocols

Cell setting into the microwell arrays on the bottom layer was performed by first creating a single cell suspension (106 cells mL^{-1}) in 1x PBS (phosphate-buffered saline).[13, 22] Bottom layers were dehydrated with a nitrogen stream and the cell suspension was pipetted directly

over the microwells on the bottom layer. Cells were settled in 4°C 1x PBS for 10 min and then slides were rinsed twice with a buffer containing carrier ampholytes but no detergents. After the application of the gel lid over the bottom layer, lysis was performed via diffusive introduction of detergents from the lid into the bottom layer for 30 to 60 s, prior to electric field application, as specified (Table 3.1). Focusing was performed in a custom 3D-printed acrylonitrile butadiene styrene (ABS) electrophoresis chamber (MakerBot, New York, NY). The lid was electrically addressed with graphite bar electrodes (McMaster Carr, Chicago, IL) embedded in the floor of the electrophoresis chamber. A potential difference of 600 V was then applied for IEF using a PowerPac high-voltage power supply (Bio-Rad, Hercules, CA). A glass slide was placed over the lid during electrophoresis to reduce evaporation. The duration of electric field application times varied depending on the experiment, as specified (Table 3.1). Following IEF separation, BPMAC-mediated protein photocapture to the gel matrix in the bottom layer was done using UV light exposure from a Hamamatsu LIGHTNING CURE LC5 unit (Bridgewater, NJ) through a Lumatec series 380 liquid light guide (Deisenhofen, Germany) with an inline UV filter (300- to 380-nm bandpass, XF1001, Omega Optical, Brattleboro, VT) suspended approximately 5 cm above the slide for 45 s with a power of approximately 400 mW cm-2 at the slide surface (320 400 nm UV meter; C6080-365, Hamamatsu), as previously described.[13, 22]

Immunoprobing

Probing was done using a variation on previously described techniques.[13, 22] The bottom layer was first placed face-down against glass, suspended by 80 μm thick spacers of Kapton tape (Dupont, Hayward, California). 40 μL of TBST solution containing primary antibodies was then introduced in the space between the gel and the glass. After a 2 hour incubation at room temperature, the bottom layer was washed in TBST for 1 hour (exchanging with fresh TBST once). Next, the bottom layer was incubated with TBST solution containing secondary antibodies for 1 hour at room temperature and washed using the approach described above. Finally, the bottom layer was washed with deionized water for 1 minute and gently dried with a nitrogen stream. Refer to the Reagents and Materials section for the antibody dilutions (v/v) used.

When primary antibodies were raised in the same host, probing of multiple targets was performed via stripping and reprobing, as previously described in other in-gel immunoassay workflows. [13, 22, 26, 30] After imaging, slides were stripped by incubation in harsh stripping buffer (62.5 mM Tris-HCl pH 6.8, 2.5% (w/v) SDS, and 1% (v/v) β-mercaptoethanol) at 50 °C overnight. After stripping, slides were washed in TBST for 20 minutes, dried, and then imaged to confirm all of the previous antibody had been removed (all lanes report a signal-to-noise ratio, SNR <3). Then, slides were rehydrated in TBST for 20 minutes in preparation for the next round of probing.

Imaging and Analysis

Imaging was conducted using an Olympus IX71 inverted fluorescence microscope (Shinjuku, Tokyo) equipped with an EMCCD camera iXon3 885 (Andor, Belfast, Northern Ireland), a motorized stage (Applied Scientific Instrumentation, Eugene, OR), an automated filter cube turret controlled by MetaMorph software (Molecular Devices, Sunnydale, CA), and an X-Cite Exacte mercury arc lamp illumination source coupled to an automated shutter and attenuation system (Lumen Dynamics, Mississauga, ON, Canada) through 4x (Olympus UPlanFl, NA 0.13) and 10x (Olympus UPlanFl, NA 0.3) objective lenses, as specified. UV channel imaging was performed with a custom UV-longpass filter cube (XF1001, excitation 300-380 nm; XF3097, emission > 410 nm) and green channel imaging was done using a filter cube optimized for GFP (XF100-3, excitation 445-495 nm, emission 508-583 nm) (Omega Optical).

Whole-device imaging was conducted using the Scan Slide function in MetaMorph at 4x magnification. Bottom layers were scanned using a GenePix 4300A fluorescence microarray scanner (Molecular Devices) after protein photocapture, immunoprobing, and wash steps using the 488 nm and 635 nm excitation lasers and the AF488 and the AF647 emission filters, as required.

For single cell experiments, profile plots from individual lanes were obtained from 500 μm high windows. Background subtraction was done using plots from a 20 μm high window in the space between lanes. SNR was calculated using the maximum signal of background subtracted plots divided by the standard deviation of the intensity of regions without band signal. For experiments with pH markers and purified wtGFP included in the bottom layer, profile plots and band parameters were obtained from 500 μm high windows in the center of the device. MATLAB (MathWorks, Natick, MA) and ImageJ (NIH, Bethesda, MD) scripts for Gaussian curve fitting and peak tracking written in-house were used to determine analyte band positions, widths, and other peak parameters.[31] Mass transport simulations were performed in COMSOL Multiphysics 4.2a (Burlington, MA) with parameters determined experimentally or obtained from literature (Figure 3.11). Endogenous protein pIs were estimated in the linear pH gradients by extrapolating from a linear fit of the tGFP peak centers. tGFP isoform pIs were obtained from microchannel IEF of U373-tGFP cell lysate (Figure 3.10). Two-way comparisons were performed with a two-sample t-test. The critical p-value was set at 0.05. Multiway comparisons were performed with analysis of variance and the Bonferroni correction for multiple comparisons

3.4 Results and Discussion

Design principles of the scIEF device

To control scIEF, we designed a multilayered polyacrylamide gel device capable of integrating all required chemistries without pumps or valves (Figure 3.2a). The device comprises a glass slide coated with a bottom gel layer for isolating single cells in microwells by gravity
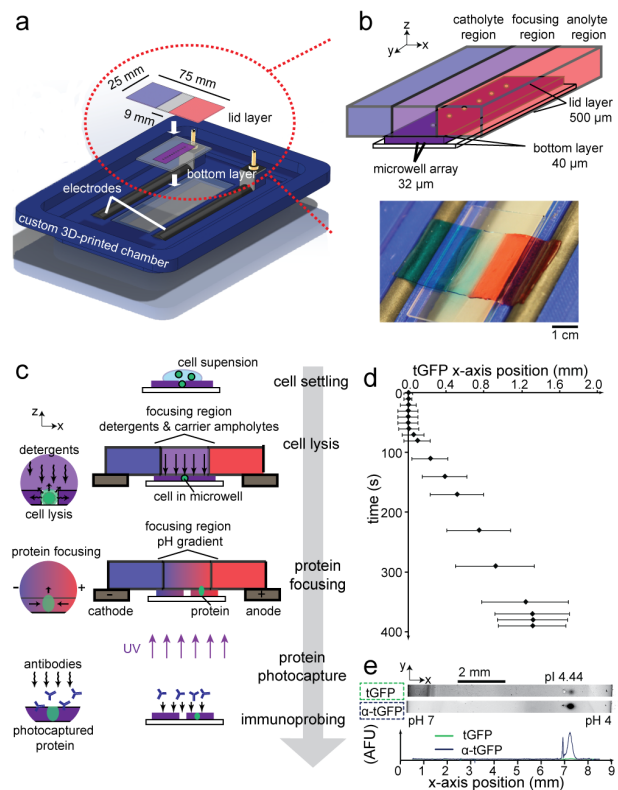
Figure 3.2: Direct measurement of proteins using scIEF. **(a)**Exploded view of the scIEF assay setup. **(b)**Isometric schematic of the multilayer scIEF microdevice and top-view photograph of the lid layer with catholyte and anolyte regions with blue and red dye, respectively. **(c)**scIEF workflow. **(d)**Time-course of tGFP fluorescence signal position during single-cell lysis and scIEF. Error bars indicate band width (4σ). pH range, 49; microwell position, 4.5mm from catholyte-side edge of the bottom gel. **(e)**Inverted grayscale fluorescence micrographs report blotting and subsequent immunoprobing (α-tGFP) from a single cell. pH range, 47; microwell position, 6.75mm from catholyte-side edge of the bottom gel. Traces are in arbitrary fluorescence units (AFU).

sedimentation and a lid gel layer patterned with chemistries to control cell lysis and (after the electric field application) the formation of pH gradients for scIEF (Figure 3.2b). The chemically patterned lid layer consists of three different regions, with 1) a central focusing region containing both the non-ionic detergent cell-lysis buffer and the mobile buffer species (carrier ampholytes) that form the pH gradient and 2) two flanking anolyte and catholyte regions created by copolymerizing weak acrylamido acids and bases in different stoichiometries into the polyacrylamide gel (that is, Immobilines; Supporting Information, Figure 3.1 and Table 3.2).[27]

Fluidic contact between the 500-μm thick lid layer and the 10-fold thinner bottom layer

diffusively imprints the chemical environment of the lid layer onto the bottom layer (Figure 3.2c). The free-standing lid layer is compliant (Figure 3.2b) and, as both the bottom layer and lid layer are fully hydrated when mated, a wetted layer at the interface ensures fluidic and electrical contact. Upon this first contact, cell lysis in each microwell is initiated by the diffusion-driven release of the mobile non-ionic lysis reagents from the lid layer into the bottom layer. To minimize evaporation during the assay, an additional glass slide is placed on top of the lid layer. At this stage, no electric potential is applied. We monitored human glioblastoma cells expressing TurboGFP (U373-tGFP) and observed the initial release of tGFP within 10s of lid application, with the fluorescence signal filling the 32 pL microwell volume within 20s (Figure 3.2d and Supporting Information, Figure 3.5). Electrodes mated to the flanking anolyte and catholyte regions initiate and sustain IEF, with the fluorescent tGFP peaks from each cell (signal-to-noise ratio (SNR) > 8) reaching a focused position approximately 310s later (Figure 3.2d and Supporting Information, Figure 3.5). We characterized the repeatability of the lid placement relative to the microwells and determined the coefficient of variance (CV) of the lid position to be about 15% (Supporting Information, Figure 3.6). Nevertheless, precise positioning of the lid will not affect the relative positions of the focused bands because the proteins will migrate to their pI regardless of the starting position of the microwell relative to the anolyte and catholyte boundaries.

Two additional design considerations constrain diffusive losses, making the long duration (relative to fast-acting diffusion) separation possible. First, diffusive losses are limited to two spatial dimensions owing to the IEF occurring along the x-axis (Supporting Information, Figure 3.11). Second, diffusive losses in the out-of-plane dimension are notably reduced by the presence of the dense hydrogel lid layer. During both lysis and focusing, simulations show that analyte diffusivity is considerably lower into the dense gel lid, compared to that into the free solution (Figure 3.3a and Supporting Information, Figure 3.11). Empirical results corroborate the reduced out-of-plane diffusive losses as approximately 15% of the total protein signal after a remarkable 600s of voltage application time (Figure 3.3b and Supporting Information, Figure 3.9). Note that the position of the microwells in the bottom layer can be optimized to reduce diffusive losses of specific proteins by reducing the electromigration time of a protein from the microwell to its pI.

Detection of isoforms of endogenous proteins from single cells

To detect endogenous isoforms, we designed a hydrogel device to support blotting of the scIEF separation and subsequent diffusive in-gel immunoprobing (Figure 3.2e and Supporting Information, Figure 3.7). By performing an immunoassay after a separation, a single antibody probe (for example, a pan-specific antibody) can detect and discern multiple, spatially separated isoforms. Our design uses a photo-active monomer (benzophenone methacrylamide) cross-linked into the bottom layer to covalently immobilize protein peaks after brief UV exposure.[13, 22] The characteristic timescale of the immobilization reaction is 5.5s.[32] Photocapture was performed with the applied electric field set to electrically floating conditions, as peak drift during photocapture confounds the pI location and reduces separation
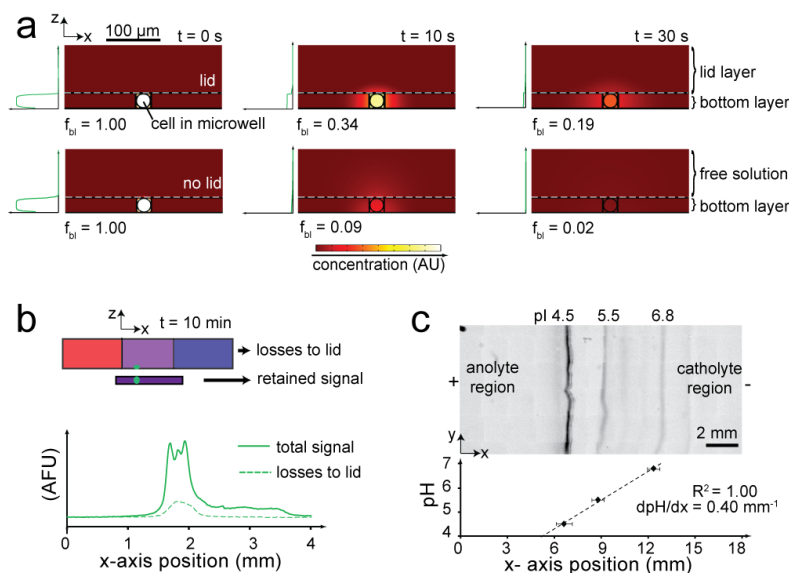
Figure 3.3: Control of diffusive and electrokinetic transport to establish robust, non-uniform chemistries for scIEF. **(a)**Concentration heat maps from a simulation show that protein diffusion out of the bottom layer is mitigated in hindered (with lid) versus unhindered (no lid, free solution) conditions. Plots indicate the maximum concentration along the z-axis; f_{bl}=fraction of the total protein in the bottom layer. **(b)** Fluorescence traces show tGFP transfer from the bottom layer to lid layer after 10min of scIEF. **(c)** Inverted grayscale fluorescence micrograph shows focused pH markers in a pH47 gradient. Dashed line is a linear fit; error bars are the peak widths (4σ).

resolution (Rs).[32] We estimate that diffusion-induced peak defocusing during the 5.5s of the immobilization reaction does not affect the pI location and reduces Rs by approximately 20%, as is consistent with our previous studies (see Supporting Information).[32] A longer (45s) UV exposure period was used to maximize the immobilization efficiency. We experimentally measured the capture efficiency of the proteins in our system to be 17.7 ± 1.5% (Supporting Information, Figure 3.8), which leads to an estimated lower limit of detection of circa 42000 molecules needed in the bottom layer before photocapture for detection by immunoprobing (see Supporting Information). Immunoprobing using primary and fluorescently labeled secondary antibodies reported a major tGFP band with an SNR of 51.87 ± 39.10 (n=9, Figure 3.2e and Supporting Information, Figure 3.7a). Importantly, covalent immobilization of the resolved proteins to the gel decouples time-dependent dilution considerations from all subsequent assay stages, archival storage, and multiple reprobing rounds.[13]

We next optimized scIEF resolving power to enhance the selectivity of isoform detection (Figure 3.4c). Adjusting the design of the chemically patterned lid layer imprints pH gradients of different length and steepness on the bottom layer, which determines the focusing time and Rs. Fluorescence flow cytometry and mass cytometry can measure up to approxi-

mately 12 and approximately 34 targets in a single cell, respectively,[33] but both techniques are unable to distinguish isoforms that lack highly selective antibodies. In contrast, in-gel immunoprobing assays with separations multiplex the product of the number of resolvable proteins (peak capacity,[34] ca. 17 for scIEF, see Supporting Information) with circa 4 spectrally distinct fluorescent dyes (labeled secondary antibodies) and 220 stripping/re-probing cycles (depending on the physicochemical properties of the target).[13, 22, 26, 30]

We investigated the capability of scIEF to concurrently measure endogenous cytoskeletal and nuclear targets (for proteins with known isoforms). We assayed tGFP (pI $\approx$ 4.5), β-tubulin (β-TUB, pI $\approx$ 5.5), and lamin A/C in individual glioblastoma cells (Figure 3.4). We used secondary antibodies, each labeled with a different fluorophore (AlexaFluor 555 and 647), to discriminate between the signal from mouse (lamin A/C) and rabbit (tGFP and β-TUB) primary antibodies, demonstrating the utility of spectral multiplexing. Using a four-color laser scanner, multiplexing can be further increased using commercially available dyes (for example, AlexaFluor). Both native and denaturing scIEF were studied, as the isoform state is sensitive to sample preparation conditions. Under native scIEF, tGFP and β-TUB were well-resolved with Rs of 1.91 ± 0.36 ($n_N = 9$ cells), yielded a conservative peak capacity of 9.0 ± 3.1 (based on the width of widest peak, β-TUB), and reported no isoforms. Expression of tGFP and β-TUB were not well-correlated (Pearson correlation, $\rho = 0.22$, p=0.60, Figure 3.4a and Supporting Information, FigureS6b).

Under denaturing scIEF (7M urea and 2M thiourea added to the lysis buffer), three tGFP isoforms ($R_S > 0.88$) and two β-TUB isoforms ($R_S = 2.54 \pm 0.46, n_D = 3$) were detected (Figure 3.4b and Supporting Information, Figure 3.7c). The tGFP isoforms arise from differential C-terminal cleavage by non-specific proteases [17] and differ by just a single charge unit. Interestingly, the native conditions yielded 86% higher total tGFP probing signal than the denaturing conditions, which is attributed to the sensitivity of the photocapture efficiency to the protein state or, possibly, to incomplete electromigration out of the microwell, as is under study (Figure 3.4c). Denaturing conditions resulted in well-resolved major β-TUB and tGFP peaks ($R_S = 1.77 \pm 0.59$) and a circa 3-fold higher peak capacity than native conditions ($28.08 \pm 6.68, n_D = 8$, Figure 3.4d). Using the pI of the tGFP isoforms (Supporting Information, Figure 3.10), we estimated the pI of the β-TUB isoforms to be 5.11 and 5.76. The acidic isoform of β-TUB had a total expression approximately 5-fold higher than that of the basic isoform ($p < 0.01$, Figure 3.4d). β-TUB isoforms have been implicated in resistance to tubulin-binding cancer therapeutics (namely, Taxol).[35]

To assess the relevance to nuclear proteins, which are difficult to assay using classical single-cell cytometry-based techniques without fractionation,[36] we assayed U373-tGFP cells for lamin A/C (Figure 3.4e and Supporting Information, Figure 3.7d). As expected, we detected lamin A/C in all glioblastoma cells. Because of its basic pI of 6.87.3,[37] the lamin A/C bands migrated toward the cathode side and focused to the left of the microwell. The fluorescent readout signals observed for this set of validation proteins were sufficient (SNR > 3) for the study of endogenous isoforms from single mammalian cells. The successful immunoprobing of lamin A/C (nuclear protein), tGFP (cytosolic protein), and β-TUB (cytoskeletal protein) demonstrates that the denaturing scIEF lysis buffer solubilizes proteins
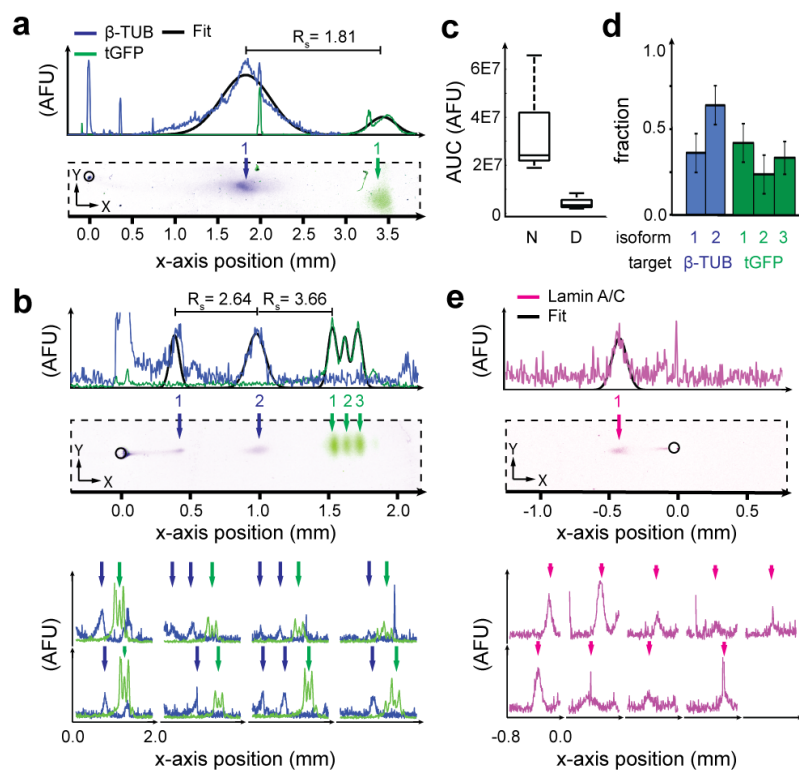
Figure 3.4: scIEF with immunoprobing resolves proteoforms in individual mammalian cells.
(a)False-color fluorescence micrographs and traces show scIEF detection by immunoprobing
of β-TUB and tGFP from individual cells. Microwells are outlined with a black circle,
located at 0mm. Arrows indicate protein peaks; plotted black outlines are the Gaussian
fits for identified peaks. (b)False-color fluorescence micrographs and traces show detection
of denatured β-TUB isoforms in 3 of 8 cells. (c)Median total tGFP probing fluorescence
(area under the curve, AUC) under native (N) and denaturing (D) conditions ($n_D = 8$,
$n_N = 9$, $p < 0.01$). (d) Relative isoform fractions ($n_{\beta-TUB} = 3$, $n_{tGFP} = 8$). (e)False-
color fluorescence micrographs and traces show detection of lamin A/C from individual cells
under denaturing conditions ($n_D = 9$). pH range, 47; microwell position, 6.75mm from the
catholyte-side edge of the bottom gel in all separations.

from the major cellular compartments. Future work will characterize and optimize the lysis buffers for more stringent applications such as histones and other high-affinity complexes.

The number of parallel scIEF separations that can be carried out on the same chip is dictated by the microwell spacing (Supporting Information, Figure 3.5) and device size (which together determine the number of microwells), as well as by the cell-settling efficiency of passive sedimentation. In this work, approximately 10 cells were analyzed per chip. The number of cells analyzed per device can be increased by fabricating larger devices or using active settling methods.[38] Future work will aim to increase the throughput of the scIEF device for more robust detection of rare events. Owing to the rapid separations, the overall throughput of the assay can be increased by running multiple separations in series and then immunoprobing several devices in parallel.

3.5 Conclusion

Direct detection of proteoforms in single cells is a crucial capability, as protein copy numbers (especially isoforms) from single mammalian cells are only sparsely reported and RNA copy number may not always correlate well with protein expression (or form).[39] The demonstrated capability of the scIEF assay to resolve isoforms of endogenous proteins from single cells provides a much-needed capability to elucidate the role of specific proteoforms in cancer progression, cardiovascular disease, and neurodegenerative disorders.[1, 40] The scIEF assay opens a separations-based avenue for measuring proteoforms, an important aspect of protein signaling that is difficult to observe with conventional cytometry tools.

3.6 Supplementary Information

pH Gradient Characterization

To initiate scIEF, the lid layer was placed directly on top of the bottom layer. The graphite anode and cathode interfaced directly with the immobile acidic and basic boundary regions, respectively (Figure 3.2c). Upon completion of IEF, the band position and width of focused fluorescent pH markers included in the bottom layer were used to quantify three key metrics of IEF performance: the pH gradient linearity, the peak capacity (n_c), and the minimum resolvable pI difference (ΔpI_{min}) (Figure 3.3c). The pH gradient was expected to be linear due to the specified carrier ampholyte mixture.[41, 42] Linearity was assessed through a linear best fit to the pH marker band positions along the separation axis, and yielded a $R^2 = 1.00 \pm 0.00$. Peak capacity quantifies the number of resolvable protein peaks for a given separation length [34] and is described by $n_c = L/(4\sigma)$, where L is the pH gradient length (along the focusing axis) and 4σ describes the band width. [16, 34] The minimum resolvable pI difference (ΔpI_{min}) measures the resolution of an IEF separation and is calculated using the expression $\Delta pI_{min} = 3 \left[DE^{-1} \frac{d(pH)}{dx} \frac{-du}{d(pH)}^{-1} \right]^{-0.5}$, where E is the magnitude of the applied

electric field, $\frac{d(pH)}{dx}$ is the slope of the pH gradient, and D and $\frac{-du}{d(pH)}$ are the diffusivity and the mobility slope of the focusing species, respectively.[43] For experiments in which we were aiming to resolve protein isoforms, we aimed to decrease ΔpI_{min} by using shallow (4-7 pH, 9 mm long) gradients. Using the pH marker band width and positions, these gradients had a peak capacity of 17.39 ± 2.42 and ΔpI_{min} of 0.13 ± 0.02 (Figure 3.3c). While pH gradients ranging from pH 4 to pH 9 enable analysis of a wide range of pIs, the steeper gradient results in worse pI resolution. Moreover, most proteins can still be focused between pH 4-7 since 70% of proteins have pIs below pH 7.[44] Careful consideration should be given to the pH gradient length and composition to optimize for separation time, detection sensitivity, and analytical performance in a given application.

Single-cell tGFP Focusing Characterization

IEF from single cells was characterized using real-time imaging (10x magnification) of tGFP expressed in U373-tGFP cells (Figure 3.2d; Figure 3.5). Cell lysis began at t = 10 s and the protein contents indicated by tGFP fluorescence were loaded upon application of a potential difference of 600 V at t = 60 s. During injection, ~4% stacking (measured as x-axis band width normalized by initial band width σ_x/σ_{x0}) was observed as the proteins entered the 6%T polyacrylamide gel from the free solution microwell (Figure 3.2d). Stacking was calculated by dividing band width at each time point by the initial band width of the signal from the microwell before cell lysis. Interestingly, in this system we did not observe enrichment in the x-axis upon IEF completion from the starting concentration in the cell; the initial band width (dictated by microwell size) was narrower than the size of the focused zones.

While focusing occurs along the separation axis (x-axis, current path), diffusion broadens the protein band in the direction transverse (y-axis) to the scIEF separation axis in the bottom layer plane. Consequently, we observed that the separation resolution (SR) in the y-axis between cells initially in microwells 500 μm apart decreased from 10.3 to 1.2 after 390 s (lysis + focusing) (Figure 3.5f). The spacing in the y-axis between the two bands was maintained with an average distance of ~495 μm with only ~1% variation demonstrating uniform migration (Figure 3.5g). With $S_R > 1$ upon completion of focusing, the 500 μm spacing was adequate to ensure no overlap between the signals of each lane, thus enabling us to perform multiple scIEF assays in parallel. With 600 V applied in devices with a 9 mm long, 4-9 pH focusing region, the maximum current of 2.38 mA was observed at 22 s after the start of focusing. The current dropped to 0.86 mA after 3 min and stabilized at 0.59 mA after 5 min.
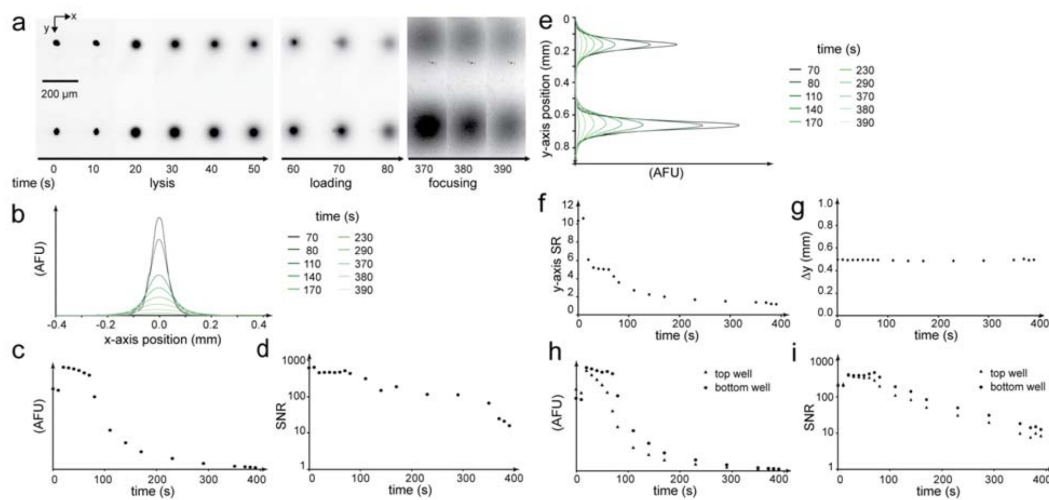
Figure 3.5: scIEF characterization using real-time imaging. **(a)** Montage of inverted fluorescence micrographs (contrast adjusted easy visualization) of scIEF from adjacent microwells expressing tGFP settled into two adjacent microwells. **(b)** Intensity profiles obtained from a horizontal x-axis window of the tGFP fluorescence signal of the bottom microwell during focusing. Plots of the moving protein band are aligned at the peak center. **(c-d)** Maximum intensity and SNR along the x-axis from the bottom microwell over time. **(e)** Intensity profiles obtained from a vertical y-axis window of the tGFP fluorescence signal of both microwells during focusing. **(f)** Separation resolution in the y-axis and the spacing between the peaks of the bands in the y-axis. **(g)** Difference in the center of both bands along the y-axis. **(h-i)** Maximum intensity and SNR along the y-axis from the bottom microwell over time. Data from the bottom microwell is shown in Figure 3.2d. Traces in arbitrary fluorescence units (AFU).

Lid Placement Reproducibility Characterization

To characterize the repeatability of the lid placement and thus the repeatability of the position of the pH gradient relative to the microwell location, we compared the peak center location of focused tGFP across three devices (Figure 3.6). Single U373-tGFP cells were assayed for tGFP in scIEF devices with a 9 mm long, pH 4-7 gradients. Focusing was performed for 6 minutes at 600 V. The native tGFP fluorescence was imaged after photocapture and the peak locations relative to the microwells was assessed. To assess the variance in the peak position across the different devices, we calculated the coefficient of variance, which is given as $CV = \sigma/\mu$ where σ standard deviation and μ is the mean. The tGFP peak center location was $x_{tGFP} = 3.10 \pm 0.46$ mm (n=3 devices, 9 cells), which gives a coefficient of variance of CV = 14.87% (Figure 3.6).
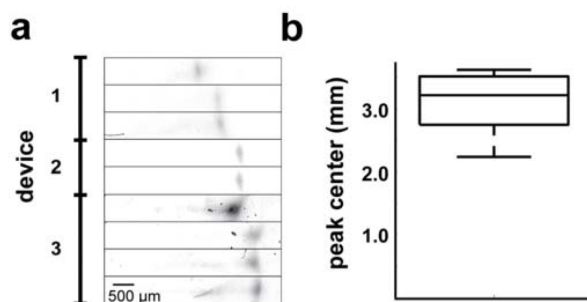
Figure 3.6: Characterization of lid placement repeatability. **(a)** Micrographs of the focused tGFP bands from single U373-tGFP cells from 3 separate devices. **(b)** The coefficient of variance of the tGFP peak location across the three devices was 14.87% (n = 3 devices, 9 cells).

Photocapture and Immunoprobing Characterization

UV photocapture resulted in irreversible photobleaching of a subset of the tGFP proteins resulting in a SNR of 4.67 ± 3.33 from single cells (n = 9). After immunoprobing, SNR was increased to 51.87 ± 39.10 (Figure 3.2e; Figure 3.7a). Multiplexed immunoprobing was performed to enable the readout of unlabeled and endogenous targets in native conditions (Figure 3.4a; Figure 3.7b). Denaturing conditions were used during scIEF to achieve resolution of protein isoforms (Figure 3.4b; Figure 3.7c) and immunoprobing of nuclear proteins (Figure 3.4e; Figure 3.7d). Owing to the short transport lengths for diffusive antibody introduction,[13] we were able to complete the scIEF assay on endogenous proteins in less than 7 hours. Moreover, not having to use the polyacrylamide gel for sieving allowed the use of low-density gels. The low-density gels facilitated diffusive antibody probing without needing to tune gel density for specific molecular weight separations, as is the case in single-cell western blotting.[13, 22, 30]
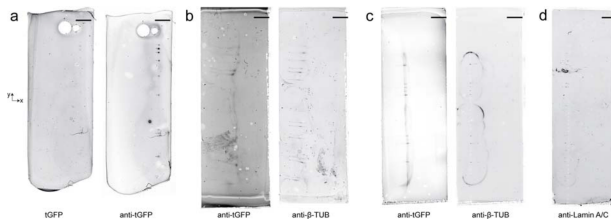
Figure 3.7: scIEF with immunoblotting slidescans of data shown in Figures 3.2, 3.3, and 3.4. Inverted fluorescence micrographs of slidescans of the bottom layer. **(a)** Photocaptured and immunoblotted tGFP signal after native scIEF. Data from these scans is displayed in Figure 3.2e. **(b)** Immunoblotted tGFP and β-TUB signal after native scIEF. Data from these scans is displayed in Figure 3.6a and Figure 3.4c. **(c)** Immunoblotted tGFP and β-TUB after denaturing scIEF. Data from these scans is displayed in Figure 3.6b, Figure 3.6c, and Figure 3.6d. **(d)** Lamin A/C signal after denaturing scIEF. Data from these scans is displayed in Figure 3.4e. All scale bars are 2 mm.

During photocapture, both electromigration and diffusional band broadening reduce resolution. Under an applied electric field, each protein peak will be immobilized while migrating along the scIEF separation axis. Such migration reduces certainty in pI and reduces scIEF separation resolution. To mitigate these confounding factors, we perform photocapture with no applied electric field (electrically floating). Under such conditions, the focused protein peak defocuses owing to diffusion. Importantly, during defocusing the peak maximum is stationary, which yields a robust determination of pI, such that only resolution losses must be considered. Using the characteristic timescale for protein photocapture (t $\sim$5.5 s),[32] the experimentally measured diffusivity for tGFP in 6%T (3.3%C) gels (D $\sim$31.3 $\frac{\mu m^2}{s}$, experimentally determined in the Diffusivity and Relative Mobility Measurements section), and the relationship

$$2Dt = x^2$$

for unconfined one-dimensional diffusion, we estimate a defocusing dispersion during photocapture that leads to a x $\sim$17 μm increase in peak width. Given the focused band width of tGFP ($\sim$90 μm, Figure 3.2d, Figure 3.5b), defocusing during photocapture results in $\sim$20% loss in separation resolution. Protein photocapture efficiency can vary depending on the buffer and denaturation state of the protein.[45] We measured the protein photocapture efficiency in the scIEF assay by comparing the total fluorescence of a photocaptured tGFP band before and after washing. To do so, we included 1 μM of purified tGFP in the bottom layer and focused for 5 min (Figure 3.8). After focusing, we illuminated the setup with UV for 45 s for protein photocapture. Note that a fraction of tGFP molecules are irreversibly photobleached during UV photocapture. We assumed that photobleaching occurred at the same rate in both captured and uncaptured protein populations. Photocapture was performed under focused conditions because the local buffer composition (carrier ampholytes) is different in focused and unfocused compositions. Following photocapture, we imaged the total tGFP

fluorescence in the bottom layer. Next, we washed the bottom layer in TBST overnight to allow protein that was not photocaptured to diffuse out of the bottom layer. Finally, we imaged the bottom layer after washing. In the before and after images, we calculated the area under the curve (AUC) of the focused band in 250 μm tall regions of interest (ROIs). We defined photocapture efficiency as $\eta = AUC_{after\,wash}/AUC_{before\,wash}$ where $AUC_{before\,wash}$ and $AUC_{after\,wash}$ are the AUC before and after washing in corresponding regions of interest, respectively. The photocapture efficiency of the scIEF assay is $\eta = 17.7 \pm 1.5\%$ (n = 30 ROIs). Interestingly, this value is higher than the 1.3-13% capture efficiencies previously observed in IEF buffers.[32] In the scIEF assay, however, we used a different carrier ampholyte and detergent mixture as well as a higher BPMAC concentration (5 mM compared to 3 mM). For IEF separations in gels the BPMAC concentration can be increased without adversely affecting the sieving properties of the gel, which is not the case for size-based separations.
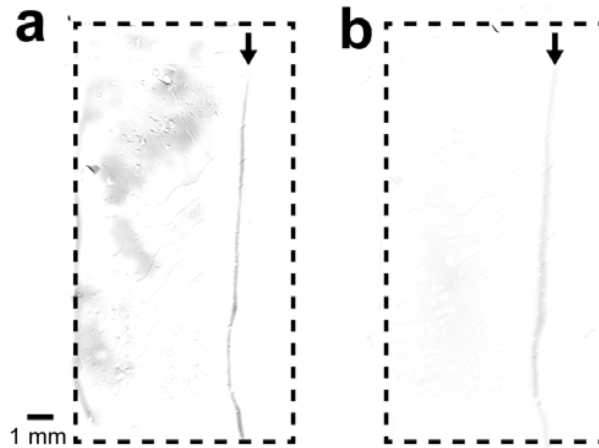

Figure 3.8: Quantification of photocapture efficiency. Micrographs of fluorescence of 1 μM tGFP fluorescence assayed with an scIEF device in native conditions (pH 4-9, 9 mm wide gradient, 5 minutes of focusing, 600 V) **(a)** before washing and **(b)** after washing. The dashed black lines indicate the extents of the bottom layer and the arrows indicated the focused tGFP. Photocapture efficiency was quantified as $\eta = AUC_{after\,wash}/AUC_{before\,wash}$ where $AUC_{before\,wash}$ and $AUC_{after\,wash}$ are the AUC before and after washing in corresponding regions of interest. Photocapture was determined to be $\eta = 17.7 \pm 1.5\%$ (n = 30 ROIs).

Using the experimentally measured protein photocapture efficiency of $\sim$17.7%, we can estimate the lower limit of detection of our system. In detailed characterization done in prior work, the lower limit of detection by in gel immunoprobing was estimated to be $\sim$27,000 molecules when the capture efficiency was 27.5%.[13] Therefore, to achieve the same number of captured proteins for immunoprobing detection $\sim$42,000 molecules are needed in the bottom layer prior to photocapture in the scIEF system when native conditions. As mentioned previously, buffer composition and the denaturation state of proteins can affect photocapture efficiency. Thus, future work should characterize in detail the optimal detergent and

carrier ampholyte compositions used in scIEF separations to maximize both photocapture and separation efficiencies.

Diffusive Protein Losses to Gel Lid during scIEF

Diffusive protein losses to the lid were estimated by including purified wtGFP at a concentration of 10 $\frac{\mu g}{ml}$ in the bottom layer gel precursor and performing IEF for 10 min. After 10 min, the scIEF setup was imaged (Figure 3.9a). The lid was then removed and imaged separately (Figure 3.9b), allowing the estimation of the protein that diffused into the gel lid from the bottom layer during IEF.
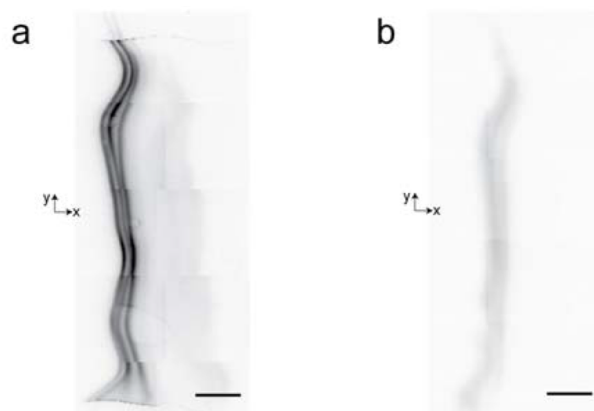

Figure 3.9: Protein losses to gel lid during IEF. **(a)** Inverted fluorescence micrograph of wtGFP signal in the IEF system (bottom layer and gel lid layer) during focusing (pH 4-9, 9 mm wide gradient, 600 V, native conditions). **(b)** Inverted fluorescence micrograph of wtGFP signal in the gel lid slide after stopping the electric field and removing gel lid from bottom layer. Data from these scans is shown Figure 3.3b. The signal in the gel lid was ~15% of the total signal in the full IEF system (lid + bottom layer) after 10 min of focusing. Scale bars are 1 mm.

Microfluidic Glass Device Fabrication and Operation

Various characterization studies and parameter estimations were done using microfluidic glass devices. Soda lime glass devices were designed, fabricated, functionalized with acrylate-terminated monolayers, and filled with photopolymerized polyacrylamide gel, as previously described.[46] Chip layouts containing a 70 μm wide and 10.4 mm long channel between ~2 mm diameter well reservoirs were designed in-house using AutoCAD 2011 (Autodesk Inc, San Rafael, CA). 20 μm deep features were fabricated on the glass chips using standard wet etching processing by Caliper Life Sciences (a PerkinElmer Company, Hopkinton, MA) using the designed chrome-glass photomask (Photo Sciences Inc., Torrance, CA). Fluid access well drilling and thermal bonding were done by Caliper.

Covalent attachment of the polyacrylamide gel to the channel walls was achieved by acrylate-terminated silane monolayer formation on the channel walls using previously described methods.[46] Channels were first washed with 1 M NaOH for 10 min, then rinsed with DI water, and then purged by vacuum. A degassed 2:3:5 (v/v/v) mixture of 3-(trimethoxysilyl)-propyl methacrylate, acetic acid, and DI water was then introduced into the channels for the silane monolayer formation. After 30 min, the channels were rinsed with methanol and DI water and then purged by vacuum. An analogous protocol was used to form the silane monolayers on glass slides.[13]

Gels were photopolymerized inside the glass channels using the same UV exposure conditions described in the main text for gel lid fabrication. UV exposure to the well reservoirs was blocked to prevent gel formation in the wells. Press-fit pipette tips were inserted into the wells to be used as 10 μl reservoirs. Continuous monitoring and control of voltages and currents for on-chip electrophoresis was achieved using a custom built, eight-channel high voltage power supply.[46] Following assay completion, gels can be removed from the glass chips allowing efficient recycling of glass chips by using an overnight incubation with a 2:1 perchloric acid and hydrogen peroxide solution heated to 75°C following appropriate safety precautions, as previously described.[46]

Cell Lysate Microfluidic IEF

IEF of cell lysate was performed in microfluidic channels (Figure 3.10) to determine the pI of tGFP. U373-tGFP cells were lysed via the addition of the native lysis detergent composition used for scIEF followed by vortexing (Analogue Vortex Mixer, VWR) and sonication (Aquasonic Model 50D, VWR). Extracts were then purified and exchanged to IEF buffer (1:10 PB74 and PB96, 3.6% (w/v) CHAPS) via centrifugation in Bio-Spin Columns with Bio-Gel P-30 (Bio-Rad) following manufacturer instructions.
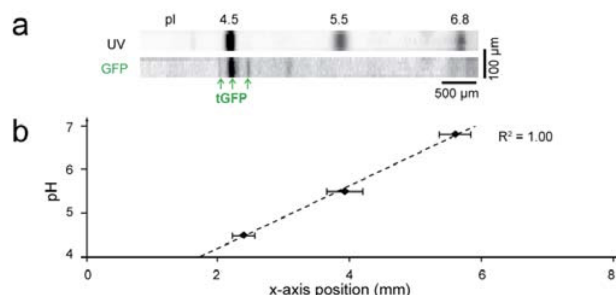
Figure 3.10: Cell extract microfluidic IEF. **(a)** Inverted fluorescence micrographs of 10x
magnification channels scans in the UV and GFP channels. The aspect ratio was distorted
for visualization of the focused bands. **(b)** Plot of the calculated position of the focused
pH markers. The error bars indicate band width (4σ) and the dotted line indicates the
extrapolated position of the linear fit of the pH gradient. The mean value $\pm$ standard
deviation of the pI for the isoforms were determined using 3 technical replicates. The pH
gradients were linear with $R^2 = 1.00 \pm 0.00$.

6%T (3.3%C) gels containing IEF buffer and 1:100 dilution of pH markers were photopoly-
merized inside the channels of the microfluidic glass devices. Sample solution containing IEF
buffer, 1:100 (v/v) dilutions of pH markers (pH 4.5, 5.5, 6.8), and a 1:20 (v/v) dilution of
the purified cell extract was electrophoretically loaded from both wells into the device for
30 s by applying a potential difference of 600 V between reservoirs.[47] After electrophoretic
loading, the electric field application was stopped and the solutions in the terminal wells
were replaced with 1x Cathode Buffer (20 mM arginine, 20 mM lysine) and 1x Anode Buffer
(7 mM phosphoric acid), both acquired from Bio-Rad. A 600 V potential difference was then
reapplied for the focusing step.

Profile plots of the focused bands were obtained from windows equal to channel width
using ImageJ. The position of the pH gradient was determined by linear regression of the
position of the fluorescent pH markers. The pI of the tGFP isoforms was estimated using
the linear fit of the pH gradient. The pI values of 4.32 ± 0.01, 4.44 ± 0.01, and 4.62 ± 0.00
for the three tGFP isoforms match the pattern for single charge differences resulting from
differential C-terminal cleavage by non-specific proteases.[17] For comparison, the isoforms
of wtGFP have pI values of 4.88, 5.00, and 5.19.[27]

Diffusivity and Relative Mobility Measurements

The diffusivities of the reagents used in the focusing region of the scIEF are given in Ta-
ble 3.3. The diffusivities D of the reagents were estimated using the Stokes-Einstein relation
given as $D = (kBT)/(\pi\eta a)$ where kB is the Boltzmann constant, T is the temperature,
η is the dynamic viscosity, and a is the hydrodynamic radius. The hydrodynamic radii of
the Polybuffers and pH markers were estimated by $a = 0.595\,(m_w)^0.427$ where m_w is the
molecular weight of the solute as specified by the manufacturer.[32] The hydrodynamic radii

of the CHAPS and digitonin micelles were obtained from literature.[48, 49] The diffusivity
of Triton X-100, urea, and thiourea were obtained from the literature.[50–52] Characteristic
times of diffusion were estimated as $t = x^2/2D$ where x is the diffusion length and D is
the diffusivity of the solute. The effect of the gel matrix on the diffusivity and partitioning
coefficients of small molecules is negligible.[53, 54] According to our estimations, the reagents
in the lysis buffer required 0.1 to 12 s to diffuse into the bottom layer where the species
remained at 92% of their initial concentration (Table 3.3), owing to the larger thickness of
the lid compared to the thin bottom layer (500 μm vs. 40 μm).

Table 3.3: Free solution diffusivities of reagents used in the focusing region of scIEF.

reagent	diffusivity ($\mu m^2 s^{-1}$)	$t_{40\mu m}$ (s)	$t_{500\mu m}$ (s)
CHAPS	133.86	5.97	933.53
Triton X-100	80.00	10.00	1562.50
digitonin	52.50	11.95	1867.50
Polybuffers (200 - 1000 Da)	7157.20	0.11-0.22	17.46-34.72
urea	903.66	1.77	276.66
thiourea	1314.00	1.22	190.26
pH markers (285 Da)	6152.68	0.13	20.32

Measurements of the diffusivity of tGFP in free solution, 6%T (3.3%C), and 15%T
(3.3%C) gels were done in microfluidic glass devices. Gels were photopolymerized inside
the devices using the same procedure used for the cell lysate IEF. The same sample solution
containing cell extract was electrophoretically loaded at 600 V for 20 s from the negative
terminal. After loading, the solution in the loading well was replaced with 1x Cathode Buffer
and a potential of 600 V was reapplied to load a band of tGFP into the channel. The electric
field application was halted and the protein band was imaged at 10x magnification for 200 s
with 20 s intervals. Profile plots were obtained from windows equal to channel width using
ImageJ. Measured band widths (4σ) were used to determine the diffusivity D of tGFP using
the relationship $2Dt = \sigma^2$ for unconfined one-dimensional diffusion from a point source. The
measured tGFP diffusivity in free solution, 6%T (3.3%C) gels, and 15%T (3.3%C) gels were
169.1 ± 94.1, 31.3 ± 5.2, and 4.2 ± 1.1 $\mu m^2 s^{-1}$, respectively.

The position of the band during loading was tracked across a distance of $\sim$525 μm during
the loading using ImageJ scripts written in house to calculate the relative mobility difference
of tGFP at the two gel densities. A custom, in-house written ImageJ script was used to
track peak position during migration.[31] tGFP mobility was 46.3 ± 1.1% lower in 15%T gels
compared to 6%T gels. The molecular weight of tGFP is reported to be 26-27 kDa.[55] The
mean $\pm$ standard deviation values are reported for 3 replicates in each condition.

Chemical Partitioning Coefficient Measurements

Partitioning measurements were performed using 2.5 cm^2 (500 μm thick) pads of polyacry-
lamide. For the free solution to gel measurements, the appropriate gel composition was

polymerized on a glass slide using the fabrication procedure shown in Figure 3.1. The gel
was then allowed to equilibrate in a 1 μM solution of tGFP on a shaker overnight. After
incubation the glass slide was removed and a second glass slide was placed on top, ensuring
that the free solution of tGFP next to the gel pad was also 500 μm thick. The gel and
free solution were then imaged using a widefield epifluorescence microscope focused on the
bottom of the gel pad (4x/NA 0.13 objective). The chemical partitioning coefficient K was
defined using the following equation: $K = \left[tGFP_{low\,free\,volume}\right] / \left[tGFP_{high\,free\,volume}\right]$.[54]

The 15%T polyacrylamide gel to 6%T polyacrylamide gel partitioning measurement was
performed in a similar manner. 6%T polyacrylamide gel and 15%T polyacrylamide gel pads
(1 cm x 2.5 cm x 500 μm) were fabricated on separated glass slides. The 6%T polyacrylamide
gel pad was incubated in 1 μm tGFP. Then the 6%T polyacrylamide gel and 15%T poly-
acrylamide gel pads were placed face-to-face. The edges of the sandwich were sealed with
paraffin wax to prevent evaporation. The sandwich was allowed to equilibrate for 4 days
then each polyacrylamide gel pad was imaged separately. We measured K_{6-FS}, the parti-
tioning coefficient of the 6%T polyacrylamide gel to free solution to be 0.51 ± 0.13. This
was 13.7% higher than our previously measured value for EGFP in 8%T polyacrylamide gel
($K = 0.44 \pm 0.05$).[13] A higher partitioning coefficient for a lower %T gel is expected due to
the increased free volume in the polymer matrix.[54] Correspondingly, K_{6-FS} was higher than
that for 15%T to free solution, K_{15-FS}, which was estimated to be 0.24 ± 0.04. Surprisingly,
K_{15-6}, the partitioning coefficient of the 15%T polyacrylamide gel to 6%T polyacrylamide
gel, was lower than both the 6%T polyacrylamide gel and 15%T polyacrylamide gel to free
solution partitioning coefficients (0.10 ± 0.04). Nevertheless, the simulations in which we
used these parameters were not sensitive to variations within this range in the partitioning
coefficients.

COMSOL Simulations of Protein Losses During scIEF

Simulations were done in COMSOL Multiphysics 4.2a (Burlington, MA). Diffusivities and
partitioning coefficients were experimentally determined or obtained from literature. Mass
transport simulations were performed to estimate protein losses during lysis and electromi-
gration in the scIEF setup reported in this work and in typical single cell western blotting
setups (Figure 3.11).[13, 22] During lysis and electromigration, losses occur over time via
diffusion and chemical partitioning between the different gel and free solution phases. For
diffusion in three dimensions, a 2D axisymmetric model was used, and for diffusion in two
dimension, a 2D model was used (Table 3.4). The gel lid was 500 μm high, the bottom layer
was 30 μm high, and the microwell was 30 μm wide. The maximum and minimum mesh
element sizes were 30 and 0.3 μm, respectively. The time steps for lysis and electromigration
simulations were 1 s and 5 s, respectively. Initial conditions before lysis were modeled as an
initial uniform starting concentration of tGFP in a 28 μm diameter cell inside the microwell.
The used diffusivities and partitioning coefficients of tGFP in different gel densities were
experimentally estimated. The configurations used for the different simulations are specified
in Table 3.4. Losses were estimated by tracking the concentration over time. The concen-

tration used was determined by integrating the protein concentration along a z-axis cutline
through the center of the microwell on the bottom layer. This concentration represents the
maximum concentration of protein in the bottom layer that would be measured by wide-field
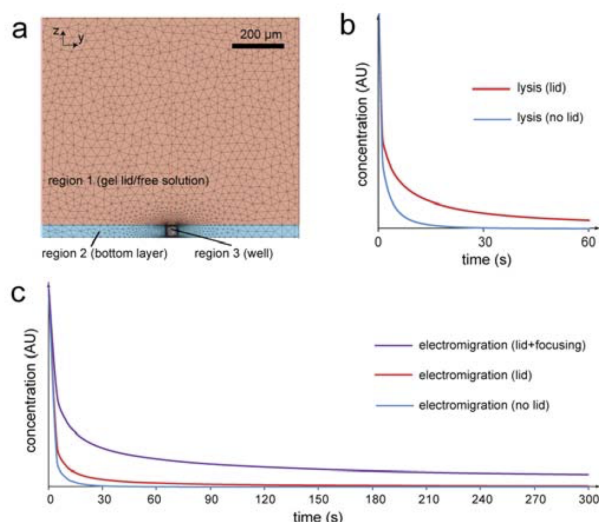microscopy.

Figure 3.11: COMSOL Simulations of protein losses. **(a)** Device geometry and mesh. The
configurations for the different conditions are specified in Table 3.4. **(b)** Retained protein
in the bottom layer during lysis. **(c)** Retained protein in the bottom layer during electromi-
gration. Retained protein was calculated by integrating the concentration along a vertical
cutline placed along the center of region 3

Table 3.4: Simulation configurations.

simulation	platform	geometry	region 1	region 2	region 3
lysis (lid)	*sc*IEF	2D axisymmetric	15%T	6%T	free solution
lysis (no lid)	*sc*WB	2D axisymmetric	free solution	6%T	free solution
electromigration (lid)	*sc*IEF	2D axisymmetric	15%T	6%T	6%T
electromigration (lid+focusing)	*sc*IEF	2D	15%T	6%T	6%T
electromigration (no lid)	*sc*WB	2D axisymmetric	free solution	6%T	6%T

For simplicity, the initial conditions used for the electromigration simulations were the
same as those used for the lysis simulations. Thus, proteins started from a uniform starting
concentration instead of the Gaussian-like zone present at the end of focusing. As an addi-
tional simplification, the differential electromigration of protein in the different gel densities

was ignored. During scIEF, proteins that diffuse off the bottom layer into the gel lid experience IEF and focus at the same position as on the bottom layer, while in single-cell western blotting, proteins that diffuse into the free solution bath do not focus. Proteins have a lower mobility at higher %T polyacrylamide gel, but in this study we assumed that during focusing the position of the protein bands on the bottom layer and gel lid coincide, justified by the rapid focusing times in our setup, our estimated mobility differences, and experimental observations (Figure 3.9). Given that no focusing occurs in single-cell western blotting, these simulations underestimate the losses during electromigration for single-cell western blotting. The detailed effects of protein molecular weight on losses during the focusing dynamics will be explored in future studies. A third simplification is that the gel lid is 500 μm in height vs. the ∼10 mm height of the free solution bath, thus providing a smaller volume reservoir for dilution. However, the diffusion time for tGFP across 500 μm of 15%T gel is ∼17 hours, so we considered the contribution from this difference negligible.

The goal of the simulations was to estimate the diffusive protein losses during the scIEF assay and gain insight into the mechanisms that mitigate these diffusive losses in the scIEF setup that enable longer separations (¿5 min) compared to single-cell western blotting (< 1 min). There are two major differences regarding the protein losses in the setup developed here for scIEF and the setup typically used for single cell western blotting demonstrated previously. First, the use of the 15%T gel lid used in scIEF compared to the free solution bath used in single-cell western blotting for lysis reagent delivery and electrical actuation leads to loss mitigation by reducing diffusion in the z-axis. With the gel lid (scIEF), integrated concentration decreased by 90% after 20 s, while without the gel lid, integrated concentration decreased by 90% after 5 s (Figure 3.11b). During electromigration, losses are further mitigated due to focusing, which eliminates diffusive losses along the x-axis. By restricting diffusion to two dimensions, integrated concentrated decreased by 90% after 115 s (Figure 3.11c). Thus, while the gel lid does help mitigate losses during lysis and electromigration, focusing, or the reduction of diffusion in three dimensions to two, is the primary reason for the reduction in protein losses in scIEF compared to single-cell western blotting.

We performed a sensitivity analysis to determine whether dense gels mitigated losses due to partitioning or due to proteins having a lower diffusivity in these regions. We varied the partitioning coefficient K_{15-6} and measured changes in the resulting integrated concentration at the different times. Changing K_{15-6} from the measured value of 0.1 to 0.24 and 0.51 in the scIEF simulations resulted in average changes of integrated concentration of < 0.02 in the tested conditions (Figure 3.11). Thus, the losses are not very sensitive to changes in the partitioning coefficient and any variations in our experimentally determined partitioning coefficients are not impactful. These results indicate that diffusive losses in the system are mitigated mostly due to the lower diffusivity in high-density gel regions and not due to the partitioning behavior that happens at the interfaces which determines equilibrium concentrations.

References

1. Alfaro, J. A., Sinha, A., Kislinger, T. & Boutros, P. C. Onco-proteogenomics: cancer proteomics joins forces with genomics. *Nature Methods* **11,** 1107–1113 (Oct. 2014).

2. Myhre, S. *et al.* Influence of DNA copy number and mRNA levels on the expression of breast cancer related proteins. *Molecular oncology* **7,** 704–718 (June 2013).

3. Smith, L. M. & Kelleher, N. L. Proteoform: a single term describing protein complexity. *Nature Methods* **10,** 186–187 (Mar. 2013).

4. Zunder, E. R., Lujan, E., Goltsev, Y., Wernig, M. & Nolan, G. P. A Continuous Molecular Roadmap to iPSC Reprogramming through Progression Analysis of Single-Cell Mass Cytometry. *Stem Cell* **16,** 323–337 (Mar. 2015).

5. Bendall, S. C., Nolan, G. P., Roederer, M. & Chattopadhyay, P. K. A deep profiler's guide to cytometry. *Trends in Immunology* **33,** 323–332 (July 2012).

6. Wei, W. *et al.* Microchip platforms for multiplex single-cell functional proteomics with applications to immunology and cancer research. *Genome medicine* **5,** 75 (Aug. 2013).

7. Stadler, C. *et al.* Immunofluorescence and fluorescent-protein tagging show high correlation for protein localization in mammalian cells. *Nature Methods* **10,** 315–323 (Feb. 2013).

8. Hattori, T. *et al.* Recombinant antibodies to histone post-translational modifications. *Nature Methods* **10,** 992–995 (Oct. 2013).

9. Pandey, A. & Mann, M. Proteomics to study genes and genomes. *Nature* **405,** 837–846 (June 2000).

10. Kelleher, N. L., Thomas, P. M., Ntai, I., Compton, P. D. & LeDuc, R. D. Deep and quantitative top-down proteomics in clinical and translational research. *Expert Review of Proteomics* **11,** 649–651 (Oct. 2014).

11. Toby, T. K., Fornelli, L. & Kelleher, N. L. Progress in Top-Down Proteomics and the Analysis of Proteoforms. *Annual Review of Analytical Chemistry* **9,** 499–519 (June 2016).

12. Lesur, A. & Domon, B. Advances in high-resolution accurate mass spectrometry application to targeted proteomics. *PROTEOMICS* **15,** 880–890 (Feb. 2015).

13. Hughes, A. J. *et al.* Single-cell western blotting. *Nature Methods* **11,** 749–755 (June 2014).

14. Tran, J. C. *et al.* Mapping intact protein isoforms in discovery mode using top-down proteomics. *Nature* **480,** 254–258 (Oct. 2011).

15. O'Neill, R. A. *et al.* Isoelectric focusing technology quantifies protein signaling in 25 cells. *Proceedings of the National Academy of Sciences of the United States of America* **103,** 16153–16158 (Oct. 2006).

16. Righetti, P. G. *Isoelectric focusing: theory, methodology and application* (Elsevier, 2000).

17. Hughes, A. J., Tentori, A. M. & Herr, A. E. Bistable Isoelectric Point Photoswitching in Green Fluorescent Proteins Observed by Dynamic Immunoprobed Isoelectric Focusing. *Journal of the American Chemical Society* **134,** 17582–17591 (Oct. 2012).

18. Li, J. J., Bickel, P. J. & Biggin, M. D. System wide analyses have underestimated protein abundances and the importance of transcription in mammals. *PeerJ* **2,** e270 (2014).

19. Schwanhäusser, B. B. *et al.* Global quantification of mammalian gene expression control. *Nature* **473,** 337–342 (May 2011).

20. Pekkala-Flagan, A. & Comings, D. E. Substitution of polybuffer for ampholytes in isoelectric focusing. *Analytical Biochemistry* **122,** 295–297 (May 1982).

21. Rabilloud, T., Barzaghi, B. & Righetti, P. G. Use of polybuffer as carrier ampholytes in mixed-bed Immobiline gels for isoelectric focusing. *Journal of biochemical and biophysical methods* **16,** 237–241 (June 1988).

22. Kang, C.-C., Lin, J.-M. G., Xu, Z., Kumar, S. & Herr, A. E. Single-Cell Western Blotting after Whole-Cell Imaging to Assess Cancer Chemotherapeutic Response. *Analytical Chemistry* **86,** 10429–10436 (Oct. 2014).

23. Stepanenko, A. A. & Kavsan, V. M. Karyotypically distinct U251, U373, and SNB19 glioma cell lines are of the same origin but have different drug treatment sensitivities. *Gene* **540,** 263–265 (May 2014).

24. Righetti, P. & Drysdale, J. W. Isoelectric focusing in polyacrylamide gels. *Biochimica et biophysica acta* **236,** 17–28 (Apr. 1971).

25. Wenisch, E., de Besi, P. & Righetti, P. G. Conventional isoelectric focusing and immobilized pH gradients in 'macroporous' polyacrylamide gels. *ELECTROPHORESIS* **14,** 583–590 (Jan. 1993).

26. Kang, C.-C., Yamauchi, K. A., Vlassakis, J. & Sinkala, E. Single cell-resolution western blotting. *Nature Protocols* (2016).

27. Tentori, A. M., Hughes, A. J. & Herr, A. E. Microchamber Integration Unifies Distinct Separation Modes for Two-Dimensional Electrophoresis. *Analytical Chemistry* **85,** 4538–4545 (May 2013).

28. Ul, N. Isoelectric points and conformation of proteins. *Biochimica et Biophysica Acta (BBA) - Protein Structure* **229,** 567–581 (1971).

29. Bennion, B. J. & Daggett, V. The molecular basis for the chemical denaturation of proteins by urea. *Proceedings of the National Academy of Sciences of the United States of America* **100,** 5142–5147 (Apr. 2003).

30. Duncombe, T. A., Kang, C.-C., Maity, S. & Ward, T. M. Hydrogel Pore-Size Modulation for Enhanced Single-Cell Western Blotting. *Advanced . . .* (2016).

31. Hou, C. & Herr, A. E. Ultrashort Separation Length Homogeneous Electrophoretic Immunoassays Using On-Chip Discontinuous Polyacrylamide Gels. *Analytical Chemistry* **82,** 3343–3351 (Apr. 2010).

32. Hughes, A. J., Lin, R. K., Peehl, D. M. & Herr, A. E. Microfluidic integration for automated targeted proteomic assays. *Proceedings of the National Academy of Sciences of the United States of America* **109,** 5972–5977 (2012).

33. Bodenmiller, B. *et al.* Multiplexed mass cytometry profiling of cellular states perturbed by small-molecule regulators. *Nature Biotechnology* **30,** 857–866 (Aug. 2012).

34. Horvath, C. G. & Lipsky, S. R. Peak capacity in chromatography. *Analytical Chemistry* (1967).

35. Verdier-Pinard, P. *et al.* Analysis of Tubulin Isotypes and Mutations from Taxol-Resistant Cells by Combined Isoelectrofocusing and Mass Spectrometry †. *Biochemistry (Washington)* **42,** 5349–5357 (May 2003).

36. Forment, J. V. & Jackson, S. P. A flow cytometry-based method to simplify the analysis and quantification of protein association to chromatin in mammalian cells. *Nature Protocols* **10,** 1297–1307 (Sept. 2015).

37. Lebel, S., Lampron, C., Royal, A. & Raymond, Y. Lamins A and C appear during retinoic acid-induced differentiation of mouse embryonal carcinoma cells. *Journal of Cell Biology* **105,** 1099–1104 (Sept. 1987).

38. Nilsson, J., Evander, M., Hammarström, B. & Laurell, T. Review of cell and particle trapping in microfluidic systems. *Analytica chimica acta* **649,** 141–157 (Sept. 2009).

39. Vogel, C. & Marcotte, E. M. Insights into the regulation of protein abundance from proteomic and transcriptomic analyses. *Nature Reviews Genetics* **13,** 227–232 (Mar. 2012).

40. Gregorich, Z. R. & Ge, Y. Top-down proteomics in health and disease: Challenges and opportunities. *PROTEOMICS* **14,** 1195–1210 (May 2014).

41. Svensson, H. Ampholytes in Natural pH Gradients. I. The Differential Equation of Solute Concentrations at a Steady State and its Solution for Simple Cases. *Acta Chemica Scandinavica* (1961).

42. Svensson, H. Isoelectric fractionation, analysis, and characterization of ampholytes in natural pH gradients. II. Buffering capacity and conductance of isoionic ampholytes. *Acta chem scand* (1962).

43. Giddings, J. C. *et al. Unified separation science* (Wiley New York etc, 1991).

44. Gianazza, E. & Righetti, P. G. Size and charge distribution of macromolecules in living systems. *Journal of Chromatography A* (1980).

45. Hughes, A. J. & Herr, A. E. Microfluidic Western blotting. . . . *of the National Academy of Sciences* (2012).

46. He, M. & Herr, A. E. Automated microfluidic protein immunoblotting. *Nature Protocols* **5,** 1844–1856 (Oct. 2010).

47. Tentori, A. M. & Herr, A. E. Performance implications of chemical mobilization after microchannel IEF. *ELECTROPHORESIS* **35,** 1453–1460 (Apr. 2014).

48. Bamber, L., Harding, M., Butler, P. J. G. & Kunji, E. R. S. Yeast mitochondrial ADP/ATP carriers are monomeric in detergents. *Proceedings of the National Academy of Sciences of the United States of America* **103,** 16224–16229 (Oct. 2006).

49. Lipfert, J., Columbus, L., Chu, V. B., Lesley, S. A. & Doniach, S. Size and Shape of Detergent Micelles Determined by Small-Angle X-ray Scattering. *The Journal of Physical Chemistry B* **111,** 12427–12438 (Nov. 2007).

50. Leaist, D. G. A moving-boundary technique for the measurement of diffusion in liquids. triton X-100 in water. *Journal of solution chemistry* (1991).

51. Sorell, L. S. & Myerson, A. S. Diffusivity of urea in concentrated, saturated and super-saturated solutions. *AIChE Journal* (1982).

52. Ludlum, D. B., Warner, R. C. & Smith, H. W. The diffusion of thiourea in water at 25 deg. C. *The Journal of Physical Chemistry* (1962).

53. Amsden, B. Solute Diffusion within Hydrogels. Mechanisms and Models. *Macromolecules* **31,** 8382–8395 (Nov. 1998).

54. Tong, J. & Anderson, J. L. Partitioning and Diffusion of Proteins and. *Biophysical journal* **70,** 1505–1513 (Mar. 1996).

55. Evdokimov, A. G. *et al.* Structural basis for the fast maturation of Arthropoda green fluorescent protein. *EMBO reports* **7,** 1006–1012 (Aug. 2006).

Chapter 4

pH Gradient Array Patterning with Hydrogel-Immobilized Buffers

This work was performed in collaboration with Augusto M. Tentori

4.1 Introduction

Isoelectric focusing (IEF) is a prominent separation technique and remains an active area of fundamental research. [1–3] IEF separates analytes by isoelectric point (pI), making the assay useful for detection of protein post-translational modifications. [4, 5] IEF separation occurs when an electric field is applied along the axis of a stable pH gradient, commonly formed by polyprotic amphoteric buffers called carrier ampholytes6. Post-translational modifications such as ubiquitination and phosphorylation, truncation are of functional biological importance and might also serve as biomarkers for disease. These post-translational modifications typically result in charge changes to the modified proteins, but result only in small molecular mass changes making IEF separations preferable to size-based separations. While a powerful separation mode, traditional bulk IEF suffers from long assay times and requires complex chemistries6.

Due to favorable scaling, microchip and micro-capillary IEF have reduced separation times. [2, 6, 7] Owing to the high surface area to volume ratio, microscale IEF devices can quickly dissipate heat generated by joule heating and thus can utilize high electric fields (100-1000 V/cm). [2, 5, 6] The high electric fields give rise to shorter mm-scale separation lengths and have reduced separation times down to minutes. [2, 6, 7] While featuring short assay times, microfludic IEF assays have been traditionally constrained to microfluidic chips or capillaries, leading to poor sample accessibility and limited throughput.

Semi-open capillary IEF chips have been fabricated to enable post-separation access for mass spectrometry detection. [8, 9] Following IEF, the devices are opened and deposited with matrix for MALDI mass spectrometry. Throughput is increased via parallel separation channels. However, the scalabilty of this design is limited because each separation lane

must be individually addressed with electrodes and buffer reservoirs, greatly increasing the complexity of assembly as throughput increases.

Recently, we have introduced an open IEF device (i.e. not enclosed in a channel or capillary) that combines the benefits of microfluidic scaling (i.e. sensitivity and rapid separations) with the benefits of traditional slab IEF (i.e. sample accessibility). [10] The Open IEF device comprises a hydrogel lid patterned with the reagents required for isoelectric focusing and a bottom layer that contains the sample and a polyacrylamide scaffold for photocapturing the separated analytes after the separation. The chemically-patterned hydrogel lid is removed following the separation, allowing full access to the analytes captured in the bottom layer for downstream analysis (e.g. immunoprobing). This approach enabled the resolution of isoforms of endogenous proteins from single cells. In addition to high separation performance, the hydrogel lid offers the potential for tailoring separations parameters (i.e. pH slope and separation axis length) to test specific biological hypotheses. However, only one gradient shape was demonstrated due to the challenge of building and aligning molds required to fabricate the multi-domain hydrogel lid.

To enable a wide range of pH gradient shapes in the open IEF device, we introduce a new method for facile fabrication of tunable pH gradients. First, we characterize both the separation performance and the stability of the pH gradients realized in the open IEF device. Second, we perform simulations to understand the effect of the device geometry and heterogeneous material properties on electric field throughout the device. Third, we demonstrate and characterize a photopolymerization method leveraging self-indexed photomasks, eliminating time-consuming and challenging aligning steps. Finally, using the self-indexed photomasks, we realize the first reported back-to-back pH gradients that enable higher device density through shorter gradients and 2D array geometries.

4.2 Materials and methods

Reagents and Materials

Acrylamide/bis-acrylamide solution (29:1, electrophoresis grade), , ammonium persulfate (APS, ACS reagent, 98.0%), 3-[(3-Cholamidopropyl)dimethylammonio] -1- propanesulfonate (CHAPS, ≥98%, electrophoresis grade), N, N, N',N'- tetramethylethylenediamine (TEMED, bioreagent, ~99%) Polybuffer 74 (P9652), Polybuffer 96 (P9777), and fluorescent IEF markers were acquired from Sigma Aldrich (St. Louis, MO). Polybuffers can used as a substitute for other carrier ampholytes such as Biolyte, Ampholine, Pharmalyte, and Servalyte, at a fraction of the cost [10, 11]. UV photoinitiator VA-086 was purchased from Wako Chemicals (Richmond, VA). Acrylamido buffer pKa 3.6 (01716) and pKa 9.3 (01738) were obtained from Sigma Aldrich. Purified recombinant wild-type GFP from Aequorea victoria (wtGFP) was sourced from Clontech (632373, Mountain View, CA).

Device Fabrication

Covalent attachment of the polyacrylamide gel to plain glass microscope slides (VWR International, Radnor, PA) was achieved by acrylate-terminated silane monolayer formation using previously described methods [12-14]. Slides were used whole or cut to desired dimensions using a diamond scribe (Ted Pella Inc, Redding, CA) and Running and Nipping Pliers (Fletcher, East Berlin, CT).

SU8 2025 photoresist (Micro-Chem, Santa Clara, CA) molds on silicon wafers (University Wafer, Boston, MA) were fabricated as previously described [14]. The base layer consisted of 40 μm thick 6%T (3.3%C) gel films and were fabricated using SU-8 wafers as molds and chemical polyacrylamide gel polymerization, as previously described1113. 1:100 dilutions of pH markers were included in the base layer precursor when specified.

The free-standing 15%T (3.3%C) polyacrylamide gel lids were fabricated using a multistep photopolymerization method. The basic and acidic regions in the gel lid contained combinations of Immobilines used to buffer at acidic and basic pH values [8]. Using patterned polyacrylamide gel regions containing Immobilines obviated the use of liquid buffers which if introduced into the focusing region would disrupt pH gradient formation. The focusing region in the gel contained 1:10 dilutions of PB74 and PB96 as the carrier ampholytes and 3.6% (w/v) CHAPS as specified (Table 4.1). Because these reagents are not immobilized, the focusing region was polymerized shortly before running the assay, in order to avoid excessive diffusion of these reagents to the acidic and basic regions. Polyacrylamide gel precursor was loaded between glass surfaces rendered hydrophobic with Gel Slick (Lonza, Rockland, Maine) spaced with. 500 μm thick, 9 mm wide spacers (C.B.S Scientific, Del Mar, CA). For gel polymerization a multistep photopolymerization process was used. First, an adherent polyimide film (Kapton tape, Dupont, Hayward, California) was placed on the back of a glass plate rendered hydrophobic. Then the outline of all of the photopatterning regions was scored using a laser cutter (Full Spectrum Engineering, Las Vegas, Nevada). The polyimide film blocks ultraviolet light and thus acted as a photomasks at each exposure step for the specified regions. UV excitation was provided by an OAI Model 30 Collimated UV light source (San Jose, CA). 4 min exposure times at 20 mW cm^{-2} powers attenuated through a 390 nm longpass UV filter (Edmund Optics, Barrington, NJ) were used. All pH measurements were done with a Twin Compact pH Meter (Horiba Scientific, Edison, NJ).

Table 4.1: Gel precursor solution compositions. Carrier ampholyte and lysis reagent composition was varied for different experiments, as specified. Base layer can include 1:100 (v/v) dilutions of pH markers and 10 μg/ml of wtGFP, as specified.

	Acidic region gel lid	Basic region gel lid	Focusing region gel lid	Bottom layer
Gel	15%T (3.3%C) 13.6 mM Immobiline II pK 3.6 6.4 mM Immobiline II pK 9.3 (pH < 3.3)	15%T (3.3%C) 14.4 mM Immobiline II pK 9.3 5.6 mM Immobiline II pK 3.6 (pH > 10.1)	15%T (3.3%C)	6%T (3.3%C) 5 mM BPMAC
Carrier ampholytes	-	-	Polybuffer 74 1:10 Polybuffer 96 1:10	-
Detergents (native)	-	-	3.6% (w/v) CHAPS 1% (v/v) Triton x-100 0.0125% (w/v) digitonin	-
Initiator	0.2% (w/v) VA-086	0.2% (w/v) VA-086	0.2% (w/v) VA-086	0.08% (v/v) TEMED 0.08% (w/v) APS

Device Operation and Experimental Protocols

The gel lid was applied to the base layer for 30 60 s, prior to electric field application, as specified. Focusing was performed in a custom 3D-printed ABS electrophoresis chamber (MakerBot, New York, NY). The lid was electrically addressed with graphite bar electrodes (McMaster Carr, Chicago Illinois) embedded in the floor of the electrophoresis chamber. A potential difference of 600 V was then applied for IEF using a PowerPac high-voltage power supply (Bio-Rad). Run conditions for each data set can be found in Table 4.2.

Table 4.2: Experimental conditions.

Data sets	Axis length [mm]	pH range	Well position	Lysis time [min]	Electric field application time [min]	Lysis reagents	pH markers in bottom layer
1B-G	9	4-9	center	.	10	native	*wt*GFP, 4.5, 5.5, 6.8, 8.1
1H	9	4-9	.	0.5	20	native	4.5, 5.5, 6.8, 8.1
4A	3	4-7	.	.	10	native	4.5, 5.5, 6.8
4B,C	3	4-7	.	.	10	native	4.5, 5.5, 6.8, 8.1

Imaging, Image Processing, and Data Analysis

Imaging was conducted using an Olympus IX71 inverted fluorescence microscope (Shinjuku, Tokyo) equipped with an EMCCD camera iXon3 885 (Andor, Belfast, Northern Ireland), a motorized stage (Applied Scientific Instrumentation, Eugene, OR), an automated filter cube turret controlled by MetaMorph software (Molecular Devices, Sunnydale, CA), and an X-Cite Exacte mercury arc lamp illumination source coupled to an automated shutter

and attenuation system (Lumen Dynamics, Mississauga, ON, Canada) through 4x (Olympus UPlanFl, NA 0.13). UV channel imaging was performed with a custom UV-longpass filter cube (XF1001, excitation 300-380 nm; XF3097, emission > 410 nm) and green channel imaging was done using a filter cube optimized for GFP (XF100-3, excitation 445-495 nm, emission 508-583 nm) (Omega Optical). Whole-device imaging was conducted using the Scan Slide function in MetaMorph. MATLAB (MathWorks, Natick, MA) and ImageJ (NIH, Bethesda, MD) scripts for Gaussian curve fitting and peak tracking written in-house were used to determine analyte band positions, widths, and other peak parameters.

Simulations

Electrical potential simulations were performed in COMSOL Multiphysics 4.2a (Burlington, MA). Conductivities were experimentally determined or obtained from literature.

4.3 Results and discussion

Design principles of the open IEF device

We designed the open IEF device to maximize control of the IEF separation parameters while minimizing fabrication complexity. In isoelectric focusing, the peak width of focused analytes is an essential metric, as it is related to both resolution and peak capacity (multiplexing) of the assay. The band width 4σ is predicted by $4\sigma = 4\left[DE^{-1}\left(\frac{dpH}{dx}\right)^{-1}\left(\frac{-d\mu}{dpH}\right)^{-1}\right]^{0.5}$, where D is the diffusivity, E is the magnitude of electric field, $\frac{dpH}{dx}$ is the slope of the pH gradient, and $\frac{du}{dpH}$ is the mobility slope.[11] Since D and dudpH are largely related to the analyte, as assay designers, we can optimize E and $\frac{dpH}{dx}$ to maximize resolution and multiplexing. Therefore we sought to design a device with independent and facile control over E and dpHdx.

In a departure from traditional IEF devices, the electrodes are independent from the boundaries of the separation axis, decoupling E and $\frac{dpH}{dx}$. To achieve this, the open IEF device features a chemically patterned lid (Figure 4.1A) that sets the boundaries of the separation axis via the immobilized pH boundaries (Immobilines) and the electrical path length via the electrode spacing. The range of the pH in the pH gradient is also set independently by patterning the separation region of the lid with the appropriate set of carrier ampholytes. Thus, the open IEF device provides the assay designer with independent control over the assay parameters that determine separation performance.
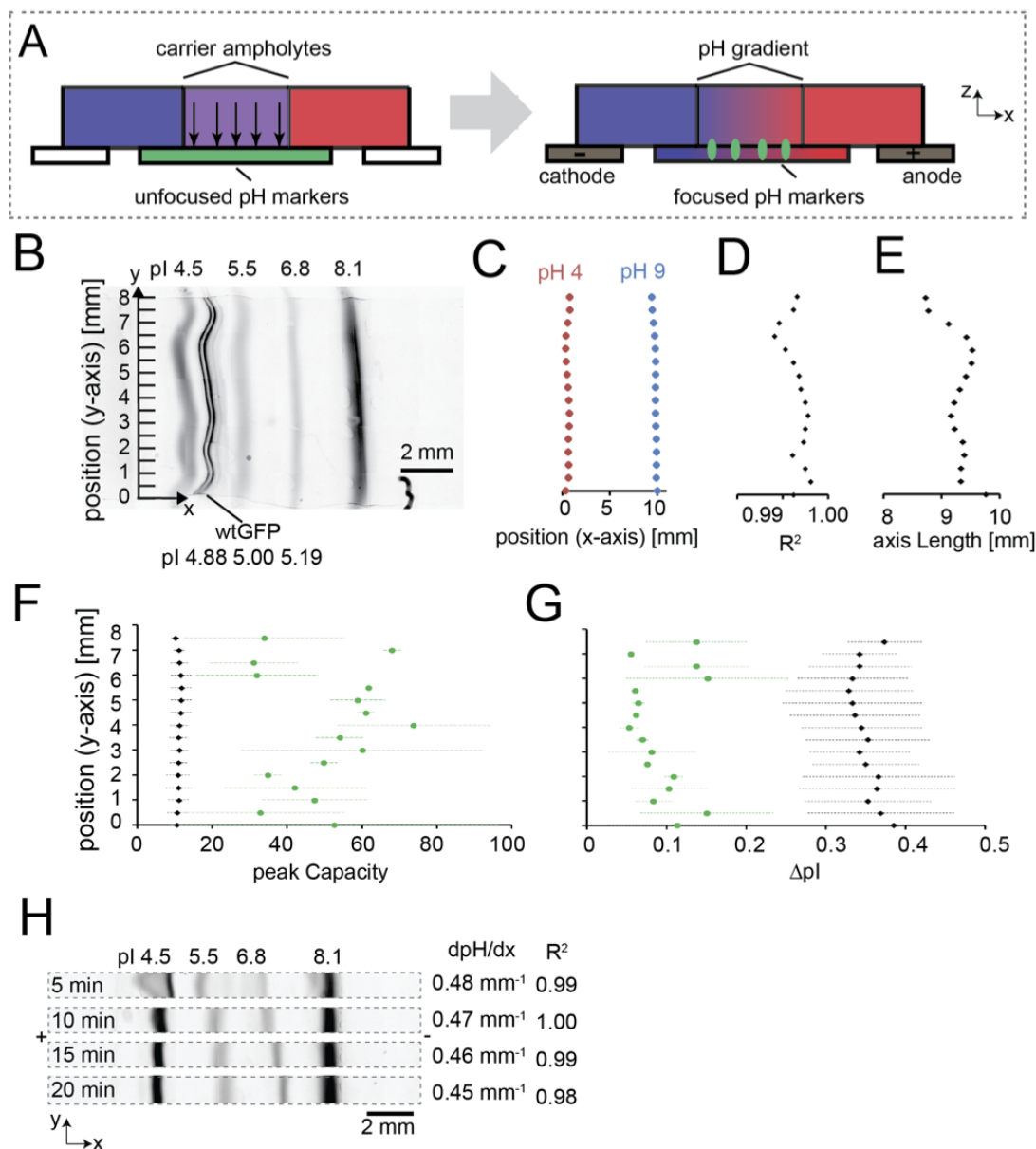
Figure 4.1: Gel lid-based pH gradients are uniform over a large area. The base layer (25x8 mm) contained the fluorescent pH markers and wtGFP and the patterned lid was 50x25 mm with a 9 mm wide focusing region. (B) Inverted UV fluorescence micrograph of a 4x scan of the IEF array system taken at 10 min from start of electric field application. The gradient was analyzed at 500 μm window intervals in the y-axis, corresponding to individual IEF sample lanes. (C) Extrapolated ends of the pH gradient (pH 4 and pH 9). (D) Linearity of the pH gradient indicated by R2. (E) pH gradient axis length. (F) Peak capacity measured using pH marker or wtGFP isoform widths. (G) ΔpI measured using either pH marker or wtGFP isoform widths. Error bars represent the standard deviation resulting from averaging the 4 different pH marker band widths and the 3 wtGFP isoform band widths. (H) Inverted grayscale fluorescence micrographs show stability of focused, fluorescent pH markers (9 mm long pH 4-9 gradient).

Further, the open IEF device design improves scalability by forming arrays of IEF separation lanes addressed by single pair of electrodes and no buffer reservoirs. Using immobilized buffers obviates the need for fluid buffer reservoirs.[12] Additionally, we hypothesize and demonstrate in this manuscript that this approach can be generalized to allow 2D arrays of IEF separations.

Patterning of pH gradients for isoelectric focusing

To ensure consistent separation performance across the device, we quantified two key metrics of the IEF array performance, the linearity and the uniformity of the pH gradients, over the large device footprint. The pH gradients are expected to be linear due to the specified carrier ampholyte mixture, but nonlinear pH gradients can also be formed using other carrier ampholyte mixtures. To determine the linearity of the pH gradient over the base layer extending 8 mm, we included well-characterized pH markers (4 commercial markers, $\sim$285 Da and wtGFP, $\sim$27 kDa) in the precursor solution of the base layer (Figure 4.1). We performed focusing by applying 600V across the lid. Using epifluorescence imaging of the pH markers, we extrapolate the location of the pH gradient extents and determined the average length of the pH gradient was 9290.33 ± 262.15 μm across all the individual 500 μm IEF lanes (Figure 4.1B). The extrapolated position of pH 4 was at an average position of 482.31 ± 150.45 μm and pH 9 had an average position of 9772.63 ± 162.98 μm (Figure 4.1C). Linearity was assessed through a linear best fit the pH markers along the separation axis, and yielded a $R^2 = 1.000.00$ across the 9 mm wide focusing region.

To quantify the multiplexing capability of the open IEF device, we next characterized the expected peak capacity. The expected peak capacity of the system quantifies the number of resolvable protein peaks for a given separation length and is described by $n_c = \frac{L}{4\sigma}$, where L is the pH gradient length and 4σ describes the band width.[11] We measured an average $n_c = 11.14 \pm 0.46$ using the four pH marker band widths. However, when n_c is calculated using the more relevant GFP isoform peak widths and not peak widths of the high diffusivity pH makers (small peptides), the n_c rises to 49.62 ± 13.86 (Figure 4.1F). The scIEF achieves similar peak capacity to in-chip immobilized pH gradient IEF devices ($n_c = 78$)[6] and in-chip carrier ampholyte devices ($n_c = 110 \pm 22$).[7] By virtue of being an open microfluidics device amenable to rapid prototyping (Figure 4.3), the scIEF assay separation axis can be easily lengthened for separations requiring a higher peak capacity and better resolution, at the expense of longer separation times.

In order to quantify the resolving power of the open IEF device, we measured the minimum resolvable pI difference, $\Delta pI_{min} = 4\sigma \frac{d(pH)}{dx}$ where $\frac{d(pH)}{dx}$ is the slope of the pH gradient.[11] Using the GFP isoform peaks, we observed an average minimum resolvable pI difference, $\Delta pI_{min} = 0.09 \pm 0.03$ pH units (Figure 4.1G). This measured resolution is similar to other microfluidic IEF assays with in-chip immobilized pH gradients7 and carrier ampholyte devices8 reporting $\Delta pI_{min} = 0.040$ and $\Delta pI_{min} = 0.15$, respectively. In considering both the resolving power and information capacity, the scIEF achieves comparable perfor-

mance to that of on chip IEF with the added benefit of being an open microfluidic device (i.e. high sample accessibility).

Lastly to determine the upper bound for maximum assay time, we consider the stability of the slope of the pH gradient in this large footprint as a function of focusing time. Over a 20 min Open IEF assay, we observed $<7\%$ changes the slope of the pH gradient stability (Figure 4.1H). By monitoring the position of the pH markers at 5 min intervals, we measured cathodic drifts of 20.78 ± 3.24 μm/min, which is comparable to previously reported values of $\sim$10 μm/min for confined microchamber IEF and $\sim$70 μm/min for single channel IEF.[12] Thus, we observed that the pH gradient was stable in all lanes over the course of 20 min, which is $\sim$4x longer than required for wtGFP focusing.

The multilayer construction of the scIEF assay generates rapid and stable pH gradients suitable for high performance IEF. Further, by nature of being an open microfluidics device, provides full access to the sample for immunoprobing following separation11.

Effect of heterogeneous materials on electric field magnitude

Next, we sought to characterize the electric field in the bottom layer, as the magnitude of the electric field is inherently linked to the achievable separation resolution in isoelectric focusing. Due to the heterogeneous, 3D construction of the lid layer, we used a finite element model implemented in COMSOL to predict the magnitude of the electric field in the separation region of the bottom layer from the voltage applied across the device.

First, to understand the effects of geometry, we simulated a device with uniform conductivity. The angle of the electric field direction was calculated using the magnitude of the x- and z-axis components. Small ($< 2^o$) variations in electric field direction were present in the first 100 μm of the focusing region on the bottom layer. Variations in the magnitude of the x-component of the electric field were present only in the initial 500 μm on the focusing region of the bottom layer. No differences in the magnitude of the electric field were measured along the height (z-axis) of the bottom layer. Thus, the multilayer geometry of the device does not introduce non-uniformity to the electric field in the bottom layer of the device.
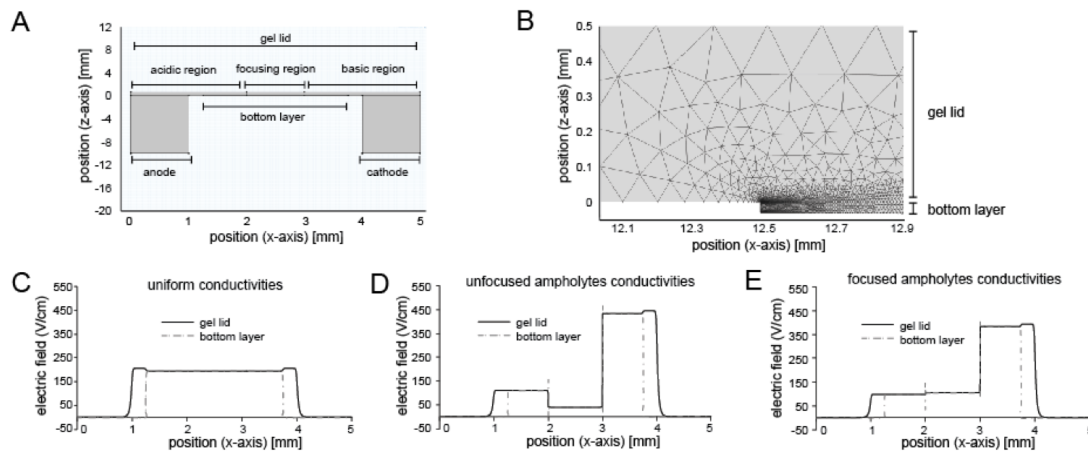
Figure 4.2: COMSOL simulations of the electric field in scIEF geometry. (A) Device geometry. (B) Zoom of bottom layer and mesh. (C) Electric field in uniform conductivities. (D) Electric field in unfocused carrier ampholytes conductivities. (E) Electric field in focused carrier ampholytes conductivities. The magnitude of the x component of the electric field along the center of the lid (250 μm) and along the center (-15 μm) of the bottom layer for all 3 conditions.

Due to the heterogeneous electrical properties of each patterned region, we performed simulations to predict effect of the material conductivities on the electric field in the focusing region of the bottom layer. To simulate the electric field at the beginning of focusing, we performed a simulation using the conductivities we measured for the Immobilines in the boundary regions and the unfocused carrier ampholytes (Table 4.2). At the beginning of focusing, we found the electric field magnitude in the focusing region to be 44.7 V cm^{-1} or 22.4% of the electric field magnitude for uniform conductivities. To simulate the electric field after formation of the stable pH gradient, we performed a simulation using the conductivities we measured for the Immobilines in the boundary regions and the focused carrier ampholytes (Table 4.3). For the focused case, we found the electric field magnitude in the focusing region to be 111.3 V cm^{-1} or 55.7% of the electric field magnitude for uniform conductivities. In both cases, the reduced electric field magnitude in the focusing region was due to the higher conductivity of the carrier ampholytes relative to the Immobilies.

Table 4.3: Measured reagent conductivities. Mean values and standard deviations reported for 3 technical replicates.

Sample	Gel	Conductivity [$\mu S\,m^{-1}$]
Water	6%T	860.1 ± 314.8
Acidic gel	15%T	7013.4 ± 1592.2
Basic gel	15%T	1891.9 ± 790.1
Focusing gel (unfocused)	6%T	34328.8 ± 2193.6
Focusing gel (focused)	6%T	4304.0 ± 1436.7
Focusing gel (unfocused)	15%T	19519.7 ± 3297.9
Focusing gel (focused)	15%T	6845.0 ± 681.7

Taken together, even with the heterogenous, multilayer architecture, the device produces homogeneous and well-aligned electric fields in the focusing region in the bottom layer. However, there is a ramp in the magnitude of the electric field from 44.7 to 111.3 V cm^{-1} during focusing due to the change in the conductivity of the carrier ampholytes as they reach their isoelectric point. Future work will focus on tuning the boundary region and carrier ampholyte conductivities to maximize the electric field in the focusing region. Further, we will investigate time-varying voltage programs to account for the change in carrier ampholyte conductivity during focusing.

Design of a method for self-indexed photopatterning

The slope of the pH gradient and thus the length of the separation axis is an essential parameter in tuning the separation performance of an isoelectric focusing assay. Therefore it is important to develop methods to fabricate lids with tunable separation regions. Photopatterning is a powerful tool for controlling the spatial organization of polymers.[13–15] However, creating precise heterogeneous structures, as is required in this design, is challenging due to the need for aligning subsequent photomasks. Thus, we developed a strategy for fabricating self-indexing masks that enable multi-step photopolymerization without alignment steps.

In this photopatterning method, the photomask is created in a single step. By fabricating the photomask in a single step, it is self-aligned, obviating the need for any tedious alignment steps. A layer of UV-blocking Kapton tape is adhered to the back of the polymerization substrate (a borosilicate glass slide) and scored with a laser cutter (Figure 4.3A, step 1). Since all of the features are cut in this initial step, they are indexed relative to each other. After mask fabrication, the regions of the mask corresponding with the first polymerization step are removed (Figure 4.3A, step 2). Then a glass plate that has been rendered hydrophobic is placed on top of the polymerization substrate, suspended by spacers that dictate the feature thickness. Then the precursor is introduced into the airgap between the two glass plates and polymerized. After polymerization, the excess precursor is removed, the next photomask region is removed, and the next precursor solution is introduced and polymerized (Figure 4.3A, step 3). This process is repeated until all polymerization steps have been

completed (Figure 4.3A, step 4). Finally, the completed hydrogel is removed from the glass plates and is ready for use.
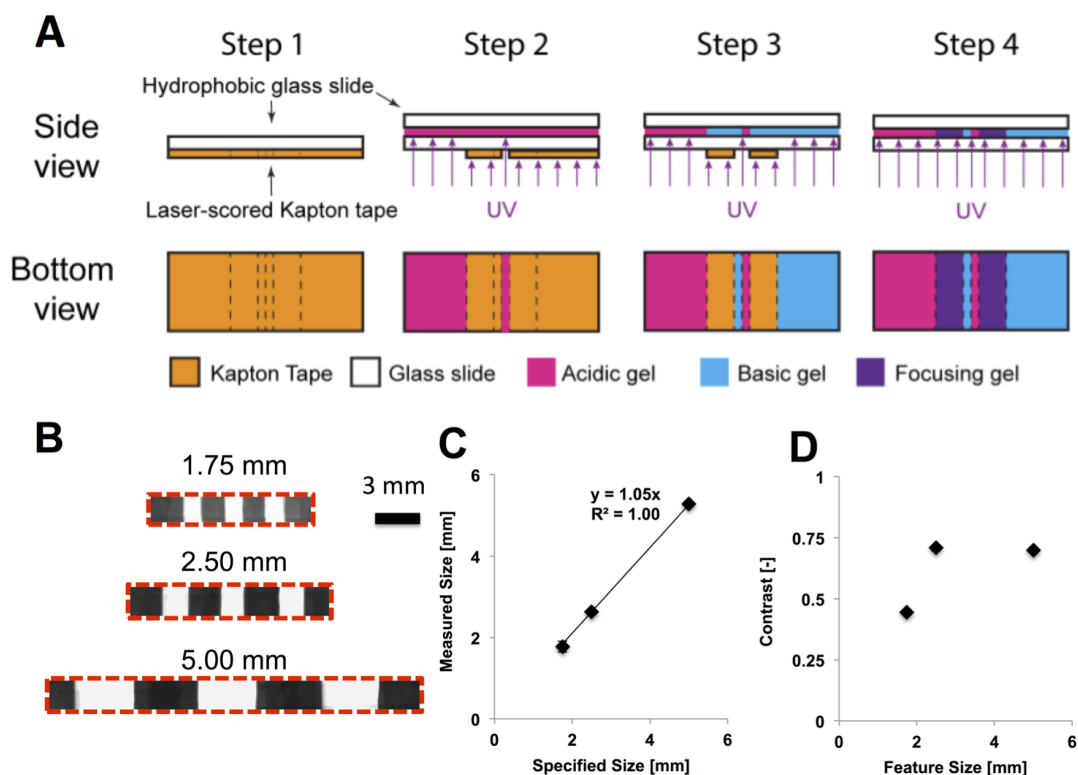

Figure 4.3: Self-indexed photomask for alignment-free multistage photopolymerization. (A) Photo-patterning method for gel lid fabrication. Step 1: A hydrophobic glass plate is backed with UV-blocking Kapton tape. The outlines of the patterned regions are scored with a laser cutter. Step 2: a second glass plate is placed over the first glass plate, separated by two 0.5 mm spacers. The regions of the Kapton tape corresponding with the acidic gel are removed. The acidic gel precursor is introduced between the glass plates and photopolymerized. Step 3: the remaining acidic gel precursor is washed away and the Kapton tape corresponding with the basic gel regions is removed. The basic gel precursor is introduced between the glass plates and photopolymerized. Step 4: the remaining basic gel precursor is washed away and the Kapton tape corresponding with the focusing gel regions is removed. The focusing gel precursor is introduced between the glass plates and photopolymerized. (B) Fluorescent micrographs of hydrogels fabricated with discrete fluorescent regions using the self-indexed photomask. (C) High correlation of the measured fluorescent region size with the photomask feature size. (D) High Michaelson contrast for all feature sizes shows low contamination between regions.

To demonstrate the self-indexed photomasks for generating hydrogel regions with dis-

crete chemistries, as required by the lid layer, we created hydrogels with alternating regions of polyacrylamide with and without fluorescent rhodamine methacrylate (Figure 4.3B). We fabricated hydrogels with 1.75, 2.5, and 5 mm wide fluorescent regions. We measured the size of the fluorescent regions with the size of the photomask using an inverted epifluorescent microscope. We found a good correlation ($R^2 = 1.00$) with a slope of 1.05, indicating the photopolymerized regions are slightly larger than the photomask (Figure 4.3C). We hypothesize this is due to broadening of the polymerization zone due to diffusion of free radicals during polymerization.[16] To quantify the cross-talk between adjacent pattern regions, we assessed the Michaelson contrast for each region (Figure 4.3D). The Michelson contrast C is defined as $C = \frac{I_{max} - I_{min}}{I_{max} + I_{min}}$ where $C > 0.1$ is considered to be resolved.[17] We found the region for all tested feature sizes to be well-resolved ($C > 0.4$).

The high correlation of the measured zone width and the mask feature size and high contrast suggest that resolution will be limited by the resolution of the laser cutter. Using a photopatterning approach enables the fabrication of lids with more complex geometries. For example, we can use geometry to modulate the overall electrical resistance of a region of the lid gel to create a uniform electric field despite the heterogeneous conductivities of the different materials.

Fabrication of back-to-back pH gradients

Using the chemically patterned lid to control the location and steepness of the IEF gradient opens the design potential to create an array of pH gradients, each with unique properties. Designing and generating arrays of pH gradients each with a different slope (by varying length or pH range) is valuable for assay optimization. Additionally, we introduce a novel approach to form back-to-back pH gradients with a single pair of electrodes and no buffer reservoir to increase the throughput of a single assay. Back-to-back gradients increase the device density and thus throughput of the traditionally throughput-limited IEF assay.

One approach to increase device density is to reduce the separation axis. To this end, we fabricated a device with a 3 mm long, pH 4-7 gradient (Figure 4.4A). As expected the gradient was linear ($R^2 = 1.00 \pm 0.00$). However, reducing the axis length decreases the separation performance of the assay. The shallower 4-7 pH, 9 mm long had peak capacity of 17 ± 2.41 and $\Delta pI_{min} = 0.13 \pm 0.02$. Confining the shallow 4-7 pH gradient to a 3 mm length results in peak capacity of 5.84 ± 1.74 and $\Delta pI_{min} = 0.41 \pm 0.15$. The decreases in peak capacity and the increase in pI are consistent with theory, as peak capacity scales with L and pImin scales with (dPh / dx)0.5.
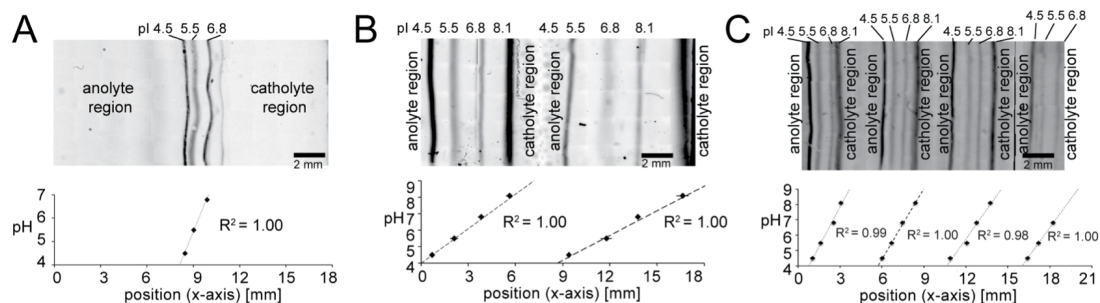
Figure 4.4: Photopatterning enables customizable pH gradients. Inverted UV fluorescence micrograph fluorescent pH markers in the IEF array system with different pH gradients. Plots show the position of the pH markers obtained from a 500 μm high window at the center of the image. Dotted line is the linear fit and the error bars indicate the band width . (A) 3 mm long pH 4-7 gradient (B) 2 back-to-back 9 mm 4-9 pH gradients formed using alternating acidic, basic, and focusing regions. (C) 4 back-to-back 3 mm 4-9 pH gradients formed using alternating acidic, basic, and focusing regions.

We hypothesized that by creating immobile pH boundaries, we would be able to construct back-to-back pH gradients, increasing the throughput of the opIEF device through 2D arrays of IEF separation lanes. We demonstrated a pair of back-to-back pH gradients ranging from pH 4 to pH 9 where the pH gradients had lengths of $8571.4 \pm 2020.3\mu m$ (Figure 4.4B). For this paired design, we measured $n_{c1} = 9.05 \pm 2.72$ and $n_{c2} = 13.48 \pm 8.20$. We further observed a $\Delta pI_{min}0.44 \pm 0.11$ and 0.38 ± 0.22, comparable to the individual pH gradient (Figure 4.4B). Building on the successful pH gradient pair design, we next designed a linear array of 4 back-to-back pH gradients (Figure 4.4C). The four gradients ranged from pH 4 to pH 9 and had an average length of $3491.70 \pm 439.48\mu m$, as well as $n_c = 4.33 \pm 1.18$ and $\Delta pI_{min} = 0.930.27$. The lower peak capacity and lower resolution compared to the shallower 4-9 pH gradients in 9 mm focusing regions matches what is expected from theory. The back-to-back pH gradients provide an extra tool for balancing separation performance and throughput in IEF assays.

The two approaches demonstrated to increase device density highlight the utility of self-indexed photomasks for rapidly generating heterogeneous hydrogel structures. In particular, the back-to-back pH gradients are to our knowledge the first in kind, paving the way to high-density 2D arrays of IEF devices.

4.4 Conclusion

We report deep characterization of the separation performance achievable with the scWB assay and a simple method for creating multi-domain hydrogels using self-indexed pho-tomasks. We demonstrated highly tunable pH gradients and to our knowledge, the first

reported back-to-back pH gradients for IEF. The back-to-back pH gradients enable 2D arrays of IEF separation lanes, paving the way for higher throughput IEF assays. In addition to applications in creating tunable IEF assays, the self-indexed photopatterning approach outlined here has broad applications in tissue engineering and drug delivery.

References

1. Hughes, A. J., Tentori, A. M. & Herr, A. E. Bistable Isoelectric Point Photoswitching in Green Fluorescent Proteins Observed by Dynamic Immunoprobed Isoelectric Focusing. *Journal of the American Chemical Society* **134,** 17582–17591 (Oct. 2012).

2. O'Neill, R. A. *et al.* Isoelectric focusing technology quantifies protein signaling in 25 cells. *Proceedings of the National Academy of Sciences of the United States of America* **103,** 16153–16158 (Oct. 2006).

3. Han, B. *et al.* Microchip free flow isoelectric focusing for protein prefractionation using monolith with immobilized pH gradient. *Journal of separation science* **32,** 1211–1215 (Apr. 2009).

4. Bjellqvist, B. *et al.* Isoelectric focusing in immobilized pH gradients: principle, methodology and some applications. *Journal of biochemical and biophysical methods* **6,** 317–339 (Sept. 1982).

5. Tia, S. Q., Brown, K., Chen, D. & Herr, A. E. Protein Post-Translational Modification Analyses Using On-Chip Immunoprobed Isoelectric Focusing. *Analytical Chemistry,* 130215131424005 (Feb. 2013).

6. Sommer, G. J., Singh, A. K. & Hatch, A. V. On-chip isoelectric focusing using photopolymerized immobilized pH gradients. *Analytical Chemistry* **80,** 3327–3333 (May 2008).

7. Hughes, A. J., Lin, R. K., Peehl, D. M. & Herr, A. E. Microfluidic integration for automated targeted proteomic assays. *Proceedings of the National Academy of Sciences of the United States of America* **109,** 5972–5977 (2012).

8. Mok, M. L. S., Hua, L., Phua, J. B. C., Wee, M. K. T. & Sze, N. S. K. Capillary isoelectric focusing in pseudo-closed channel coupled to matrix assisted laser desorption/ionizatuion mass spectrometry for protein analysis. *The Analyst* **129,** 109–110 (Feb. 2004).

9. Guo, X. *et al.* UV embossed polymeric chip for protein separation and identification based on capillary isoelectric focusing and MALDI-TOF-MS. *Analytical Chemistry* **78,** 3249–3256 (May 2006).

10. Tentori, A. M., Yamauchi, K. A. & Herr, A. E. Detection of Isoforms Differing by a Single Charge Unit in Individual Cells. *Angewandte Chemie International Edition* **55,** 12431–12435 (Sept. 2016).

11. Giddings, J. C. *et al. Unified separation science* (Wiley New York etc, 1991).

12. Tentori, A. M., Hughes, A. J. & Herr, A. E. Microchamber Integration Unifies Distinct Separation Modes for Two-Dimensional Electrophoresis. *Analytical Chemistry* **85,** 4538–4545 (May 2013).

13. Duncombe, T. A. & Herr, A. E. Photopatterned free-standing polyacrylamide gels for microfluidic protein electrophoresis. *Lab on a Chip* **13,** 2115–2123 (June 2013).

14. Cho, K. *et al.* Multi-Compartmental Hydrogel Microparticles Fabricated by Combination of Sequential Electrospinning and Photopatterning. *Angewandte Chemie,* n/a–n/a (July 2015).

15. Cornwell, D. J., Okesola, B. O. & Smith, D. K. Multidomain Hybrid Hydrogels: Spatially Resolved Photopatterned Synthetic Nanomaterials Combining Polymer and Low-Molecular-Weight Gelators. *Angewandte Chemie International Edition,* n/a–n/a (Aug. 2014).

16. Park, S. *et al.* Controlling uniformity of photopolymerized microscopic hydrogels. *Lab on a Chip* (2014).

17. Kukkonen, H., Rovamo, J., Tiippana, K. & Näsänen, R. Michelson contrast, RMS contrast and energy of various spatial stimuli at threshold. *Vision Research* **33,** 1431–1436 (July 1993).

Chapter 5

Development of image processing tools for rapid quantification of arrayed separation data

This work was performed in collaboration with Julea Vlassakis.

5.1 Introduction

Separations are an important tool for selectively measuring biomolecules. Separations enhance selectivity by spatially separating molecules by a physical (e.g. size) or chemical (e.g. isoelectric point) property. [1–3] Additionally, separations are used to simplify complex mixtures for analysis with mass spectrometry.[2] To facilitate analysis of these separations, signal and image processing tools are needed to identify and quantify the separated analytes.

Analysis tools have largely focused on 1D separation data because separations are traditionally performed in 1D geometries such as capillaries or individual separation lanes. Researchers have used techniques such as deconvolution to rapidly analyze many 1D separations in series. [4–6] Impressively, Shackman et al. have analyzed 1300 separations in 5 minutes. [4] However, owing to the advancement of microfabrication technology, separations have been performed in devices with 1D and 2D arrays of separation lanes. Therefore, new image processing tools are needed to analyze arrayed separation data.

The Herr Lab has previously developed scripts for analyzing arrayed single-cell western blotting (scWB) data. [7, 8] However, it is challenging to modify or add functionality to these scripts because there are over 20 dependencies and the data is not stored in a standardized format. Also, analyzing scWB datasets is time consuming because the scripts require many manual interventions. Therefore, we sought to develop a new set analysis scripts with a simpler interface.

Here we present a set of MATLAB scripts for analyzing images of arrayed separations. Through a functional decomposition, we reduce the number of required scripts from 20 down

to 4. Further, we defined a data structure for facile data access and maniputing. We also designed the functions to maximize reproducibility. While the analysis scripts described here were designed to analyze scWB data, they are well-suited for analyzing other arrayed separations such as single-cell isoelectric focusing or comet assays. [9, 10]

5.2 Results and Discussion

Design Approach

In order to reduce analysis time and enhance reproducibility, we sought to develop a suite of scripts to automate the analysis of single-cell western blotting data. Single-cell western blotting data comprises a fluorescent micrograph of hundreds-to-thousands of separation lanes in a rectangular array. Each separation lane contains zero to several fluorescent protein bands, which can each be parameterized by their peak height a, their peak center $\bar{x}$ and their peak width 4σ. In developing the scWB analysis scripts, we were guided by three key design principles: (1) minimize the number of scripts and amount of user input, (2) create a standardized interface for interacting with the data, and (3) support complete replication of data.

Towards the goal of minimizing the number of scripts and the amount of user input, we used functional decomposition to identify the key actions the script must take in order to complete the analysis (Figure 5.1). Our overall task was to generalize standard single lane peak analysis to an arbitrary rectangular array of separation lanes. We discretized the task into four subtasks: (1) image segmentation, (2) intensity profile generation, (3) curve fitting, and (4) quality control. Through this funcational decomposition, we were able to reduce the number of dependencies from over 20 down to only 4.
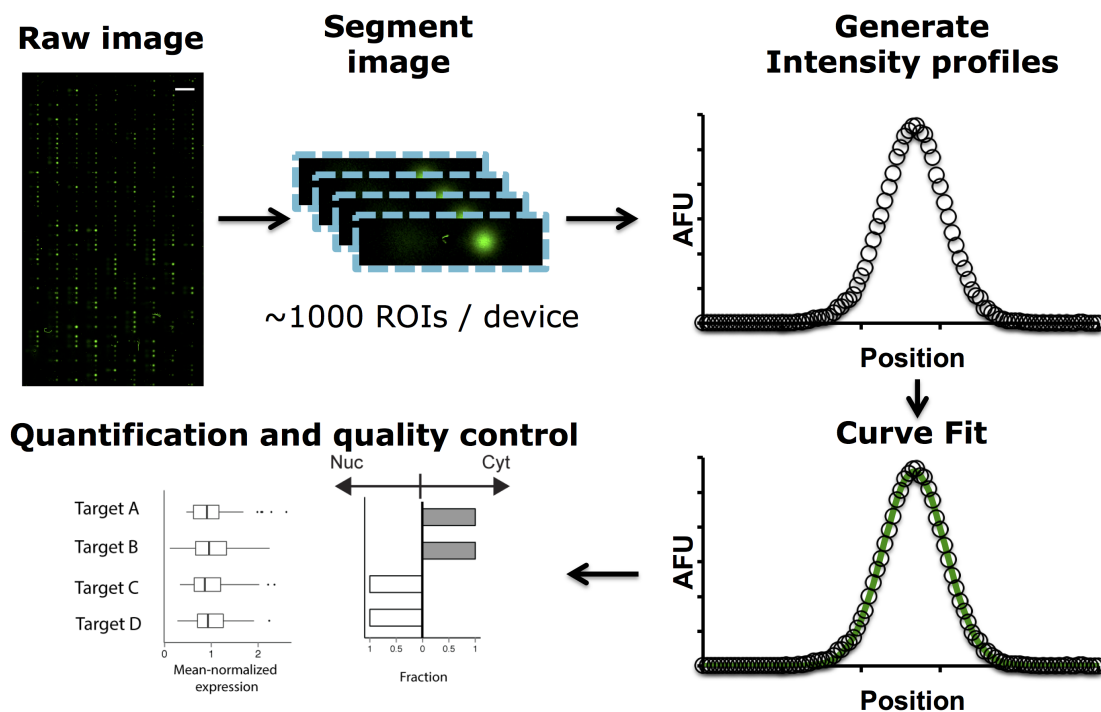
Figure 5.1: Functional decomposition of arrayed separation image analysis. The task of analyzing images of arrayed separation data was discretized into four subtasks: (1) image segmentation, (2) intensity profile generation, (3) curve fitting, and (4) quality control.

We created a standardized interface for interacting with the data by defining a data structure to hold all of the data and parameters associated with a single analysis. Defining a data structure ensures consistent methods for accessing the data for further processing, which both reduces the complexity in performing the analysis and also lowers the barriers to writing scripts to add new functionality or analyses.

To support the complete replication of data, we designed the scripts to save all user-defined and automatically-determined parameters in the output data structure. By saving all parameters, users can completely review the steps required to produce the output and subsequently reproduce it. Further we made all generated variables immutable to prevent key information from being lost.

Data structure

In order to create a standardized interface for the data, we defined a data structure to hold the data from the analysis. The data structure must be able to store multiple types and shapes of data and also the data should be accesible using human-readable field names. It is necessary to store many different data types because the scWB analysis generates data types ranging from 2D arrays (e.g. images) to strings (e.g. file names). Further, having data

accessible with human-readable field names improves usability. In MATLAB, there are two data structures that allow storage of multiple data types: cell arrays and structures. We chose to use a structure, as it offers human-readable field names while cell array elements are addressed via indices.

We implemented the structure such that the data and parameters from each step of the analysis are saved in a unique field. Doing so ensure reproducibility by allowing the user to completely recapitulate the analysis. By saving the data in standardized, human-readable field names, we have made it simple to write scripts for processing these data.

In the future, implementing the data structure as a class may provide added security and functionality. For example, we could design the class to hold the data in private variables and only allow access to them through methods. These methods could have checks built in to prevent overwriting of data (to ensure it is immutable) and further checks on the quality of the data (e.g. is it of the correct type and shape?). Further, we could add methods to automate processing and slicing the data. For example, we could have a method to automatically output all ROI images for lanes that passed the analysis quality control. Ultimately, we opted against this approach, as using structures provides more flexibility during the early development. However, now that the basic functionality has been created, it could be advantageous to implement a custom class to store and process the scWB data.

Image segmentation

The first step in the analysis is to segment the full image of the scWB device into individual separation lanes in preparation for analyzing each separation lane in series. Since the microwells in the scWB device are arranged in a rectangular array, we must rotate the image such that the separation lanes are aligned with the horizontal axis of the image and define the bounds of the microwell array. We determine both the angle of rotation and bounds of the array through a graphical user interface (GUI) in three clicks (Figure 5.2A and B). The user simply selects the upper-right-hand well, the lower-right-hand well, and the upper-left-hand well. The script calculates the angle of rotation from the angle of the line defined by the the upper- and lower-right hand wells from vertical. The bounds of the array are defined by the rectangle with the three selected points as corners (the fourth corner is extrapolated from these three points).
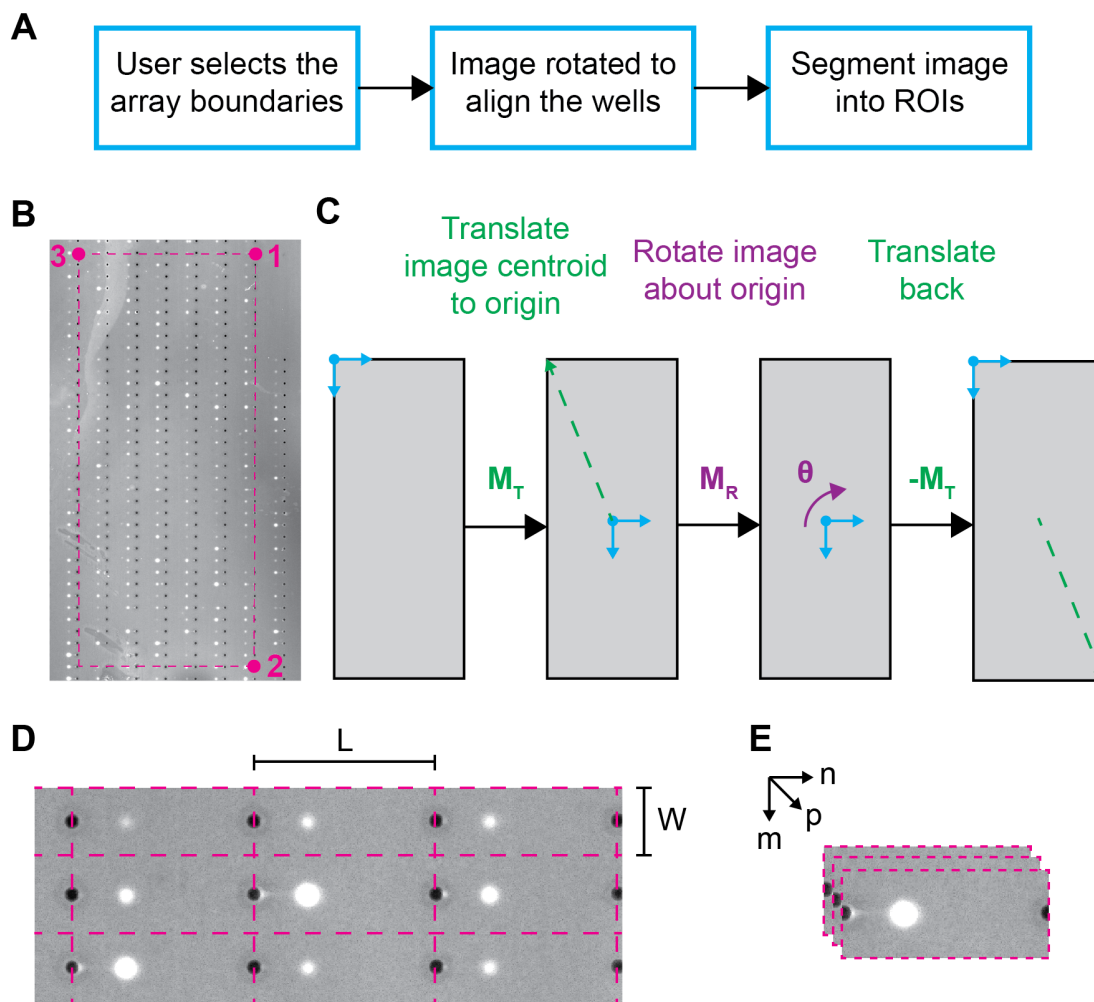
Figure 5.2: Image segmentation to extract individual lanes from images of arrayed separations. (**A**) The image segmentation function automatically rotates, aligns, and segments the image after the user defines the boundaries of the array. (**B**) The user defines the boundaries of the array with three clicks: the upper-right-hand corner, the lower-right-hand corner, and the upper-left-hand corner. The function calculates the angle of rotation from the angle of the line defined by the upper- and lower-right-hand corners of the array. (**C**) The function transforms the boundaries of the array onto the rotated image. (**D**) After the image has been rotated and aligned and the boundaries of the array are defined, the image is automatically segmented into lanes defined by the separation length l and lane width w. (**E**) The segmented lanes are stored in a $w \times l \times n$ array where n is the number of separation lanes.

Following image rotation, the points defining the corners of the rectangular array must be transformed onto the rotated image (Figure 5.2C). To do so, the same transformation used by the built-in MATLAB image rotation function imrotate() is performed on each

point. Briefly, a translation is applied to shift the centroid of the image to the origin, which is located in the upper-left-hand corner of the image. Then the points are rotated at the specfied angle about the origin. Finally, the opposite translation is applied so the origin is again in the upper-left-hand-corner of the image. Now that the image and bounds of the rectangular array of separation lanes has been rotated, the image is segmented into regions of interest with user-specified length l and width w (Figure 5.2D). The result regions of interest are stored in a w x l x n array where n is the number of regions of interest (Figure 5.2E). Thus, each region of interest can be easily accessed by indexing the third dimension.

Intensity profile generation

To generate 1D intensity profiles from 2D images of separation lanes, we performed background subtraction and integrated the fluorescent intensity along the axis perpendicular to the separation axis (Figure 5.3). First, we use a local background subtraction scheme to remove background signal that may not be uniform along the separation axis. Briefly, for each position along the separation axis x_i the background signal is calculated from gutter regions at the same position x_i, but outside of the separation lane. Following background subtraction, the background subtracted image is converted to a 1D intensity profile by integrating along the y-axis.
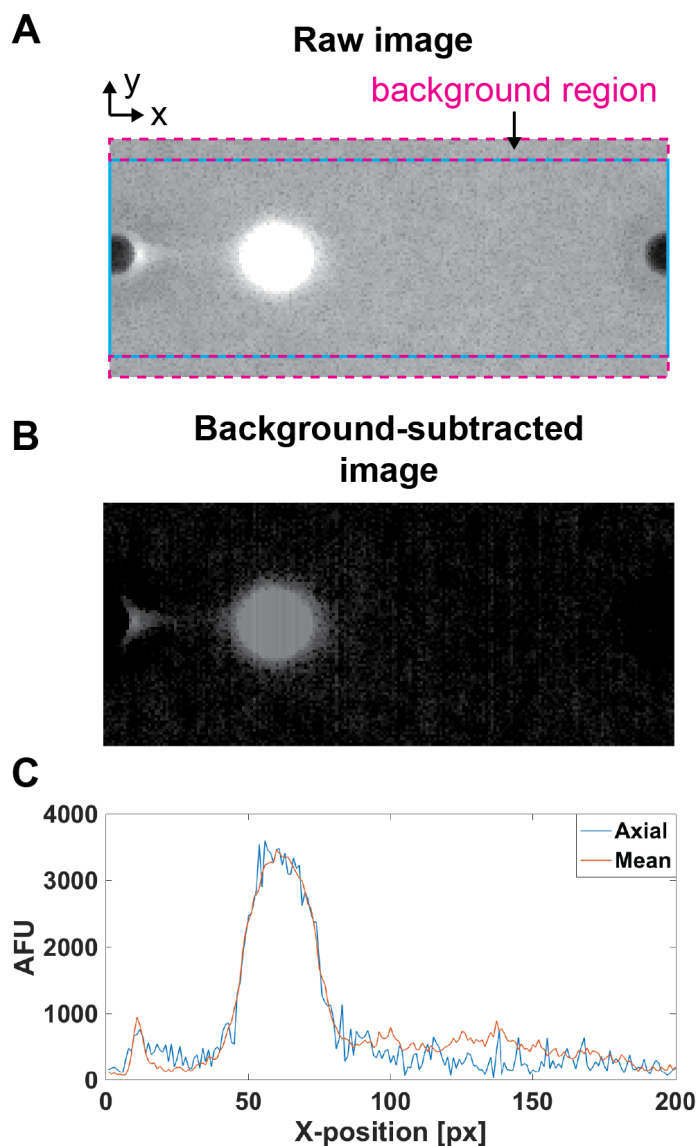
Figure 5.3: Background subtraction and intensity profile generation. (**A**) Fluorescent micrograph of an unprocessed separation lane. For each position (x_i, y_j) in the separation lane (blue box), the background level will be calculated from the background regions on the periphery of the separation lane (magenta box) at position x_i and subtracted. (**B**) A background subtrated separation lane. (**C**) The 1D intensity profile is generated by integrating the fluorescence along the y-axis

Curve fitting

We quantified each separation peak by performing a Gaussian fit to each 1D intensity profile.
Since band broadening is a result of diffusion, we expect each peak to take on a Gaussian
profile [3, 8]. To aid in the fitting process, we created a GUI to allow the user to define
constraints for the fit parameters. We minimized the number of user interactions by deter-
mining all of the constraining the fit parameters from just the estimated bounds of the peak
x_1 and x_2. First, we constrained the peak center $\bar{x}$ to $x_1 < \bar{x} < x_2$. Next, we constrain the
peak width parameter σ to $0 < \sigma < (x_2 - x_1)$. Finally, we constrain the amplitude a using
the maximum y-value in the intensity profiles y_{max} and the relationship $0 < a < y_{max}$. We
implemented the curve fitting routine in a for loop that allows a fitting of a user-defined
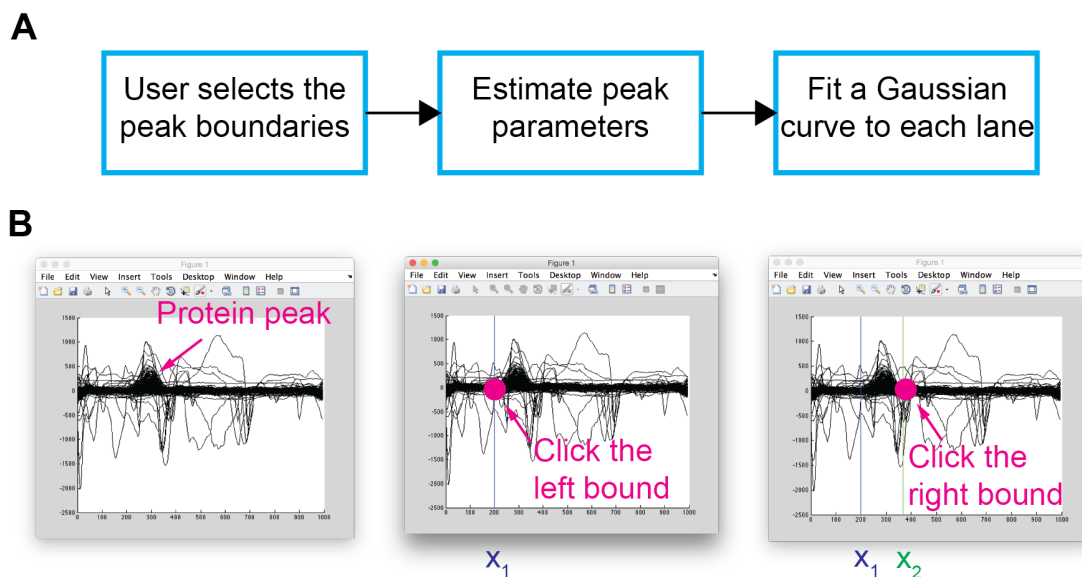number of peaks per separation lane.

Figure 5.4: A GUI guides the user in fitting Gaussian curves to each protein peak. **(A)**
Gaussian curve fitting is aided by parameter constraints estimated from user-selected peak
bounds **(B)** The user selects the peak bounds x_1 and x_2 through a GUI.

Quality control

Finally, we provided a GUI for performing quality control. Since a standard scWB device
may contain 1000s of separation lanes we chose to implement automated filtering to reduce
the number of lanes that require manual inspection (Figure 5.5). To filter out lanes that do
not contain peaks or contain artifacts, we filter out lanes with poor Gaussian fits (i.e. R^2
value). The R^2 threshold is user definable, but the default criterion is $R^2 > 0.7$ [8]. After
filtering by R^2 value, we created a GUI to display the intensity profiles that pass the R^2

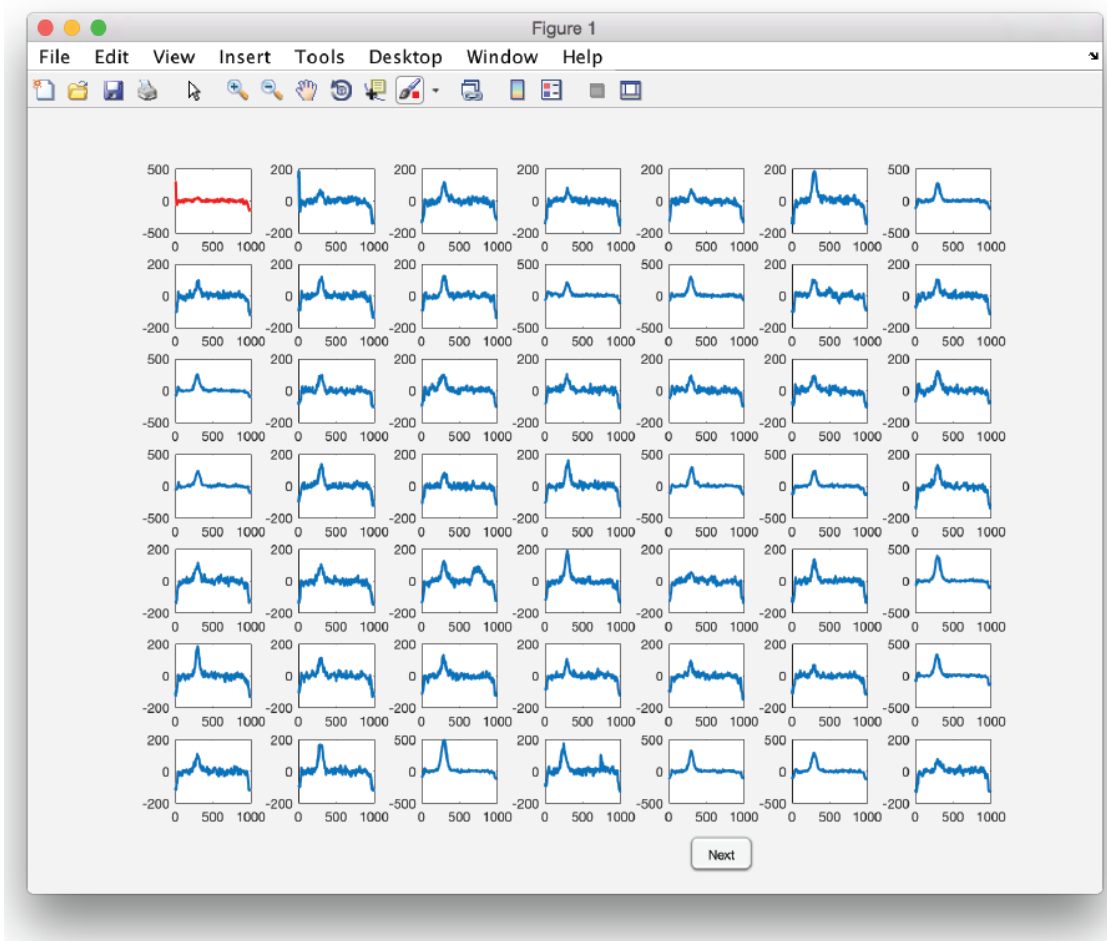threshold in grids that the user can then select the intensity profiles that do not pass quality control.

Figure 5.5: The users perform quality control of the separation lanes that pass the R^2 threshold by selecting the intensity profiles with artifacts. The selected intensity profiles are highlighed in red.

User testing

Following the development of the scWB analysis scripts and internal testing we tested the analysis scripts at scWB module of the Cold Spring Harbor Laboratories Single-cell Analysis short course. The students were experienced researchers from a diverse set of fields including biology, statistics, and engineering. Thus, they ranged in experience with programming and the command line. The overarching feedback we received is that the GUI and data structure made using the scripts straight forward. However, some students commented that the quality

control step is succeptible to user-specific bias due to the manual selection of artifacts. Thus we were currently investigating using machine learning to develop a classifer to automatically identify separation lanes containing artifacts.

Highlighting the flexibility of the modular analysis scripts, we were able to rapidly adapt the scWB analysis scripts to analyze the 1D arrays of separation lanes from the single-cell isoelectric focusing (scIEF) assay. [10] Since the analysis of intensity profiles is unchanged, we simply had to adapt the image segmentation to support 1D arrays of separation lanes. We did not have to re-validate the analysis downstream of the image segmentation (the first step), saving development time and effort. The modular design that resulted from our functional decomposition enables rapid and flexible development of new capabilities for the analysis of arrayed separation data.

5.3   Conclusions

Here, we have developed a suite of analysis scripts for analyzing arrays of microscale separations. By discretize the task by function, we reduced the number of dependencies from 20 down to 4. Further, by automating image rotation and alignment, we reduced the amount of user interaction and the analysis time to approximately 5 minutes per image containing 7000 microwells. [7] While we demonstrated the scripts analyzing single-cell western blotting and isoelectric focusing data, these scripts could also be used to analyze other arrayed separations, such as the comet assay. [9, 11] Future work will focus on developing pipeliness for the analysis of the quantified separations and classifiers for automated quality control.

References

1. Bjellqvist, B. *et al.* Isoelectric focusing in immobilized pH gradients: principle, methodology and some applications. *Journal of biochemical and biophysical methods* **6,** 317–339 (Sept. 1982).

2. Lee, K. H. Proteomics: a technology-driven and technology-limited discovery science. *Trends in Biotechnology* **19,** 217–222 (June 2001).

3. Giddings, J. C. *et al. Unified separation science* (Wiley New York etc, 1991).

4. Shackman, J. G., Watson, C. J. & Kennedy, R. T. High-throughput automated post-processing of separation data. *Journal of Chromatography A* **1040,** 273–282 (June 2004).

5. Caballero, R. D., García-Alvarez-Coque, M. C. & Baeza-Baeza, J. J. Parabolic-Lorentzian modified Gaussian model for describing and deconvolving chromatographic peaks. *Journal of Chromatography A* **954,** 59–76 (Apr. 2002).

6. Li, J. Comparison of the capability of peak functions in describing real chromatographic peaks. *Journal of Chromatography A* **952,** 63–70 (Apr. 2002).

7. Hughes, A. J. *et al.* Single-cell western blotting. *Nature Methods* **11,** 749–755 (June 2014).

8. Kang, C.-C., Yamauchi, K. A., Vlassakis, J. & Sinkala, E. Single cell-resolution western blotting. *Nature Protocols* (2016).

9. Wood, D. K., Weingeist, D. M. & Bhatia, S. N. *Single cell trapping and DNA damage analysis using microwell arrays* in *Proceedings of the National Academy of Sciences of the United States of America* (2010).

10. Tentori, A. M., Yamauchi, K. A. & Herr, A. E. Detection of Isoforms Differing by a Single Charge Unit in Individual Cells. *Angewandte Chemie International Edition* **55,** 12431–12435 (Sept. 2016).

11. Gutzkow, K. B. *et al.* High-throughput comet assay using 96 minigels. *Mutagenesis* **28,** 333–340 (Apr. 2013).

Chapter 6

Polymerization of polyacrylamide in PDMS microchannels

6.1   Introduction

New device geometries have enabled new funcationality in microscale separations. For example, 2D geometries have given rise to both discrete [1] and continuous [2] two-dimensional separations. Also, fabrication of many 1D channels in parallel has enabled high throughput western blotting. [3] Glass chips are commonly used due to their optical properties and well-characterized surface properties. [1–4] Unfortunately prototyping new geometries in glass chips can take days due to the required etching processes, [4] thus presenting a bottleneck in developing new microscale separation technologies.

Polydimethylsiloxane (PDMS) has become a popular rapid-prototyping material for microfluidics devices [5, 6]. Using soft-lithography methods, PDMS devices can be cast with micron resolution in a matter of hours [6]. However, PDMS is highly permeable to oxygen and thus not well-suited for radical polymzerization because oxygen inhibits radial polymerization. [7] The Doyle Lab has leveraged the oxygen inhibition to prevent sticking of fabricated particles to the walls of their device. [7–9] Additionally, the Ren lab has used high powered (100W) ultraviolet light (UV) sources to overcome the oxygen inhibition and polymerize polyacrylamide in PDMS microchannels. [10] However, this required a high-powered UV source and required rastering the source over the microchannel (30 minutes per device), thus providing a challenge for scaling up devices.

Here we report the development of a method for polymerizing polyacrylamide in PDMS microchannels for rapid prototyping of device geometries for microscale electrophoretic separations. To reduce oxygen inhibition, we introduce benzophenone into the PDMS. The benzophenone form radicals during polymerzation which scavenge the diffusing oxygen, thus preventing oxygen from inhibiting polymerization. We characterize the sieving performance of the resulting polyacrylamide by separating fluorescently-labeled proteins and analyzing their electrophoretic mobilities. Additionally, we demonstrate separations in a reversibly-

bonded PDMS device, enabling downstream sample access.

6.2 Results and Discussion

Benzophenone modification for grafting of polyacrylamide to PDMS

In reducing inhibition of radical polymerization by oxygen, there are two primary approaches: (1) reduction of the flux of oxygen into the channel and (2) increase the rate of radical generation. [7] Given the diffusivity of oxygen in PDMS, we would have to degas the walls of the device for hours. Thus we aimed to reduce the flux in other ways. Previously, benzophenone has been used to graft linear acrylamide to PDMS microchannels. [11, 12] In doing so, the benzophenone in the PDMS walls scavenges oxygen as it diffuses towards the microchannel. Further this grafts the polyacrylamide to the PDMS walls. However, this has not been demonstrated with polyacrylamide-filled channels, as would be required for polyacrylamide gel electrophoresis (PAGE) separations. [12] We hypothesized that benzophenone treatment to PDMS walls would enable the fabrication of polyacrylamide-filled PDMS microchannels.
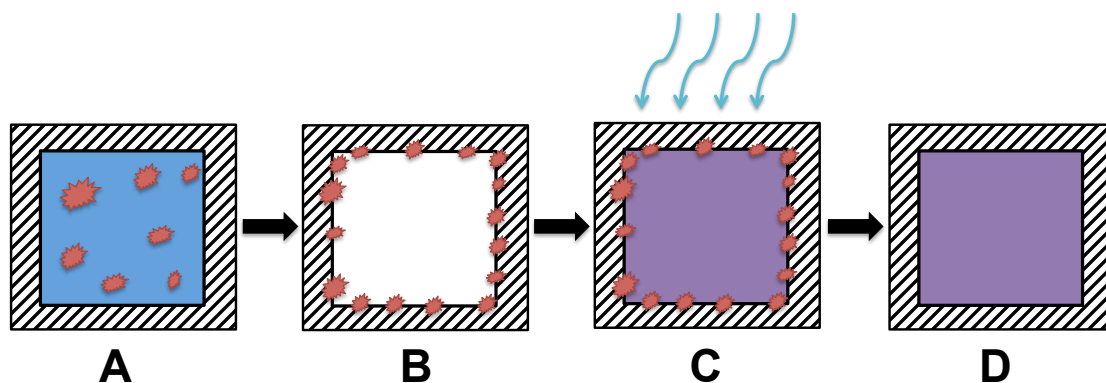

Figure 6.1: Schematic of the proposed protocol for photopolymerizing PA in a benzophenone-modified PDMS channel. **(A)** 10% benzophenone in acetone is incubated in the channel 10 minutes, **(B)** the channel is dried, **(C)** the polyacrylamide with VA-086 photoinitiator is loaded in the gel and polymerized with an ultraviolet light source, **(D)** the unpolymerized PA is rinsed from the channel.

To test this hypothesis we first fabricated polyacrylamide films on PDMS and tested for bonding of the polyacrylmide to the PDMS. Building from the work of Simmons *et al.*, we performed a screen of grafting protocols with the conditions in Table 6.1. [13] We prepared a solution of 10% (w/v) benzophenone in acetone and incubated it on top of a 1 cm tall PDMS slab (9:1 base:crosslinker). After incubating the slab in the benzophenone solution for 10 minutes, we washed the slab and introduced the polyacrylamide precursor (8%T, 3.3%C,

0.1% VA-086). We observed polymerization after 10 minutes of UV exposure ($12\frac{mW}{cm^2}$) and no polymerization in the negative control group (no benzophenone treatment).

Table 6.1: Conditions and results for benzophenon-functionalized PDMS. The benzophenone was introduced to the slab for 10 minutes in a 10% solution in acetone.

Group	Benzophenone	UV Exposure Time	Polymerization
1	No	10 mins.	No
2	Yes	5 mins.	Partial
3	Yes	10 mins.	Yes
4	Yes	15 mins.	Yes

Next, to demonstrate the benzophone functionalization would enable a fully-filled poly-acryalmide channel in PDMS, we constructed a microchannel with PDMS comprising all four walls (Figure 6.2). First, we fabricated an SU8 mold to form 90 μ wide and 40 μm tall microchannels. Then we cast the PDMS (9:1 base:crosslinker) on the mold and cured it overnight at 60 ^{o}C. After curing, we cut the devices off of the mold, punched holes for the wells with a dermal punch and plasma bonded the device to a PDMS slab. Then we introduced the 10% benzophenone in acetone solution and incubated for 10 minutes. We then removed the benzophenone solution and washed thoroughly with methanol an water. Finally, we introduced our polyacrylamide precursor and polymerized with a UV lamp (8 mins. 12 $\frac{mW}{cm^2}$). We co-polymerized a fluorescent methacrylate so that we could visualize the regions containing polyacrlamide with an epifluorescent microscope (Figures 6.3. Following polymeriztion, we cut the PDMS device and imaged *en face* with an inverted epifluorescent microscope. We observed fluorescent signal throughout the cross-section of the microchannel after washing the sectioned device in phosphate-buffered saline for 1 hour, confirming we had achieved polymerization of polyacrylamide throughout the cross-section of the microchannel.
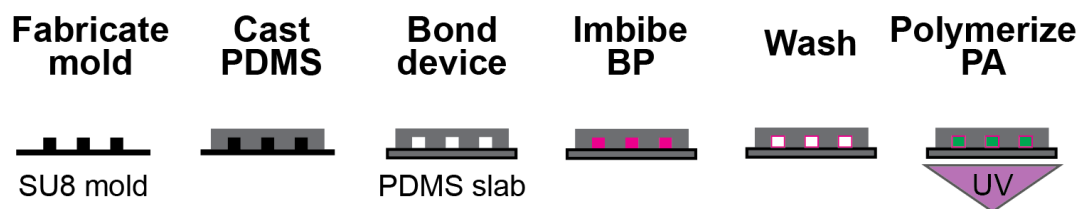
Figure 6.2: Schematic of the fabrication protocol for polymerization of polyacrylamide in benzophenone-modified PDMS microchannels. First, an SU8 mold is fabricated on a silicon substrate. Then the PDMS is cast on the mold and cured. After curing, the device is removed from the mold, the wells are formed with a dermal punch, and plasma bonded to a PDMS slab. 10% benzophone in aceton is then introduced in the channels and incubated for 10 minutes. Following the incubation of benzophenone, the channels are washed thoroughly with water and methanol. Finally, the polyacrylamide precursor is introduced and polymerized with ultraviolet light.
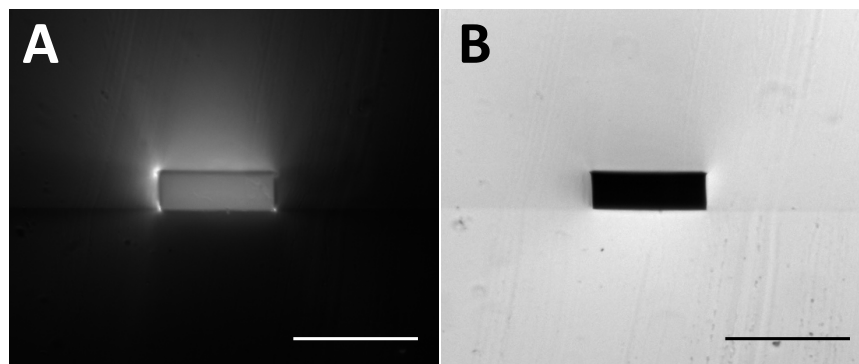

Figure 6.3: Micrographs of a cross-section of polymerized a rhodamine-labled polyacrylamide in a benzophenone-functionalized channel in (A) epiflourescence and (B) bright field (B). The fluorescent signal throughout the cross-section of the channel demonstrates that the benzophone is able to overcome oxygen inhibition to enable polymerization of polyacrylamide in PDMS microchannels. The scale bars are 100 μm long.

Polyacrylamide gel electrophoresis in PDMS microchannels

Since we had successfully fabricated PDMS channels filled with polyacrylamide, we hypothesized we could fabricate PDMS microdevices with a glass bottom (Figure 6.4A). We opted to fabricate the device with a glass bottom because PDMS is autofluorescent. First, we fabricated PDMS devices comprising a single microchannel (90 μm wide, 40 μm tall) using standard soft lithography (Figure 6.4B). Then we plasma bonded the PDMS device to a glass

slide. Following plasma bonding, we functionalized the glass slide for binding polyacrylamide by incubating the microchannel with 3-(trimethoxysilyl) propyl methacrylate. [4, 14] Next, we functionalized the microchannel with benzophenone, as described in the section above. After washing the channel, we introduced the 8%T 3.3%C polyacrylamide precursor (0.1% VA-086) and photopolymerized for 8 minutes (10 $\frac{mW}{cm^2}$).
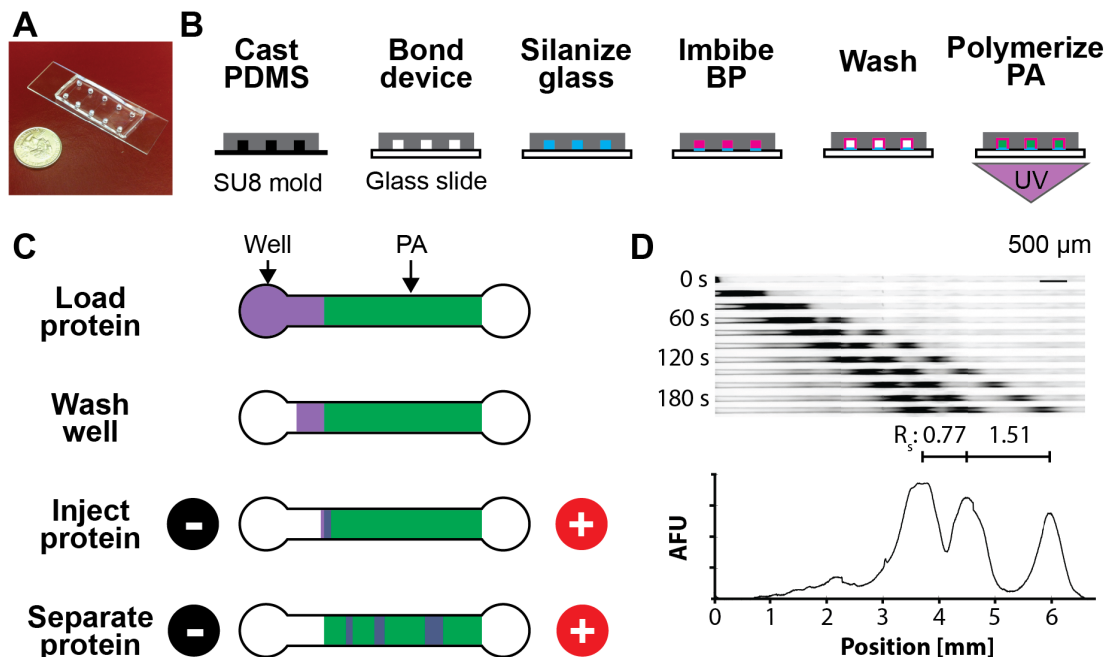

Figure 6.4: Polyacrylamide gel electrophoresis in a permanently-bonded PDMS microchannel device. (**A**) Photograph of the assembled device. (**B**) First, an SU8 mold is fabricated on a silicon substrate. Then the PDMS is cast on the mold and cured. After curing, the device is removed from the mold, the wells are formed with a dermal punch, and plasma bonded to glass slide. The glass is then silanized by incubating the channels in silane solution. 10% benzophone in aceton is then introduced in the channels and incubated for 10 minutes. Following the incubation of benzophenone, the channels are washed thoroughly with water and methanol. Finally, the polyacrylamide precursor is introduced and polymerized with ultraviolet light. (**C**) After device fabrication, the protein sample is loaded into the well. After the protein is loaded, the well is washed out and exchanged for buffer. The electric field is applied and the protein is injected into the polyacrylamide gel and separated. (**D**) (top) Montage of inverted micrographs of a fluorescently-labeled BSA-OVA-TI ladder being separated. (bottom) The intensity profile corresponding with the final timepoint. OVA and TI are baseline resolved ($R_s = 1.51$) and BSA and OVA are nearly resolved ($R_s = 0.77$).

To test the sieving properties of the polyacrylamide gel, we separated a fluorescently-

labeled protein ladder compressing bovine serum albumin (BSA), ovalbumin (OVA), and trypsin inhibitor (TI) with polyacrylamide gel electrophoresis (Figure 6.4C). To perform the PAGE assay, we first pipetted our protein ladder into the loading well. We then applied an electric field to load the sample into the separation channel. After loading the channel we exchanged the sample in the loading well for 1x tris-glycine. Finally, we separated the injected plug of proteins by applying an electric field ($E = 200\frac{V}{cm}$) and observed the separation with timelapse epifluorescent microscopy (Figure 6.4D). We quantified the separation performance with separation resolution $R_s = \frac{x_1 - x_2}{0.5(4\sigma_1 + 4\sigma_2)}$ where x_n is the peak ceneter of band n and $4\sigma_n$ is the band width of band n. After 200 s of separation, we observed baseline separation of the the OVA and TI ($R_s = 1.51$) and near resolution of the OVA and BSA ($R_s = 0.77$).

We hypothesized that since PDMS can be reversibly bonded to glass, [15] it would also be possible to perform PAGE in a reversibly-bonded PDMS microchannel. To test this hypothesis, we fabricated devices in a similar manner to the plasma-bonded devices. First, we created the PDMS microchannels using SU8 soft lithography (Figure 6.5A). After casting the devices, we removed dust from the PDMS and glass surfaces with Scotch tape. Next, we placed the cleaned SU8 device on the glass slide, reversibly bonding the device. Finally, we functionalized the channel with benzophenone and polymerized the polyacrylamide as done in Figure 6.4. Note that we did not silanize the glass surface so that the polyacrylamide did not cross-link to the glass.

As with the plasma-bonded device, we quantifed the separation performance of the reversibly-bonded device by performing PAGE on a fluorescently-labeled BSA-OVA-TI ladder (Figure 6.5B). After only 60 s (70% faster than the plasma-bonded device), we observed baseline resolution of OVA and TI ($R_s = 1.56$) and near resolution of BSA and OVA ($R_s = 0.87$). To further understand the difference in the resuling polyacrylamide gel between the plasma bonded and reversibly-bonded devices, we quantified the electrophoretic mobilty for each of the protein species and found the mobilities of proteins in the reversibly-bonded device to be one order of magnitude greater (Figure 6.5C, $p < 0.05$, multiway anova, bonferroni correction). The higher mobility in the reversibly-bonded devices suggests the polyacrylamide matrix has larger pores. We hypothesize the difference in pore sizes is due to differential polymerization behavior when the polyacrylamide is not grafted to the glass surface. Polymers grafted to a surface tend exhibit different average molecular weights and polydispersity than those polymerized in free solution. [16] As expected, when we removed the PDMS layer, the polyacrylamide was retained in the PDMS microchannel, thus providing facile post-separation access to the sample.
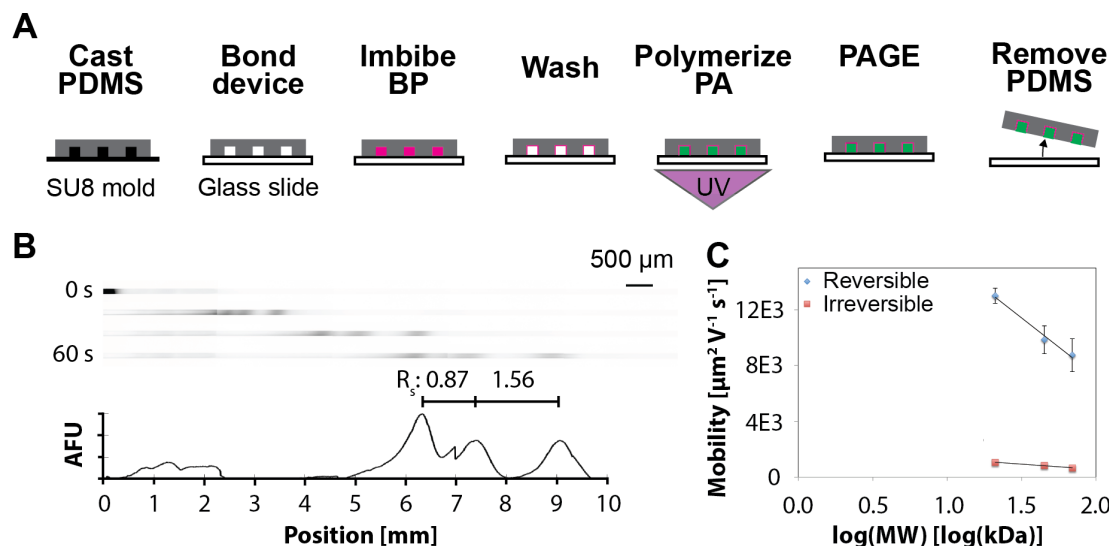
Figure 6.5: Polyacrylamide gel electroporesis in a reversibly-bonded PDMS microchannel. (**A**) First, an SU8 mold is fabricated on a silicon substrate. Then the PDMS is cast on the mold and cured. After curing, the device is removed from the mold, the wells are formed with a dermal punch, and placed on top of a clean glass slide. 10% benzophone in aceton is then introduced in the channels and incubated for 10 minutes. Following the incubation of benzophenone, the channels are washed thoroughly with water and methanol. Finally, the polyacrylamide precursor is introduced and polymerized with ultraviolet light. (**B**) Inverted micrographs of a fluorescently-labeled BSA-OVA-TI protein ladder analyzed by PAGE. The intensity profile corresponds with the last time point. The OVA and TI were full resolved ($R_s = 1.56$) (**C**) The proteins analyzed in the reversibly bonded device exhibited a greater electrophoretic mobility, suggesting the polyacrylamide in the reversibly-bonded devices has larger pores than then permanently-bonded devices. Error bars are $\pm$ 1 SD

We have demonstrated PAGE in PDMS microchannels using benzophenone to prevent oxygen. Leveraging the bonding of PDMS to glass, we have performed PAGE separations in reversibly-bonded microchannels. Using reversibly-bonded channels could potentially enable post-separation sample access for in-gel immunoprobing [3] or ionization for mass spectrometry [17, 18].

Sized-based separation of proteins in PDMS microchannels

Next, we sought to demonstrate protein sizing in PDMS microchannels. Separating proteins by their molecular weight can be used to identify off-target signal and protein isoforms. Protein sizing is achieved by coating all proteins in the anionic detergent sodium dodecyl sulfate (SDS), ensuring all proteins have the same mass-to-charge ratio. Thus all differences in electrophoretic mobility are based on the size of the protein, which emperically has been shown to have a linear relationship between $log(mass)$ and electrophoretic mobility. [19] To

enhance separation resolution, we implemented transient isotachophoresis (tITP). [20] tITP
uses a discontinous buffer system to preconcentrate the sample as it is injected (Figure 6.6).
During injection, the ITP stack reaches a pore discontinuity (i.e. the free solution-gel in-
terface) and the trailing electrolyte overtakes the sample, switching from an ITP mode to a
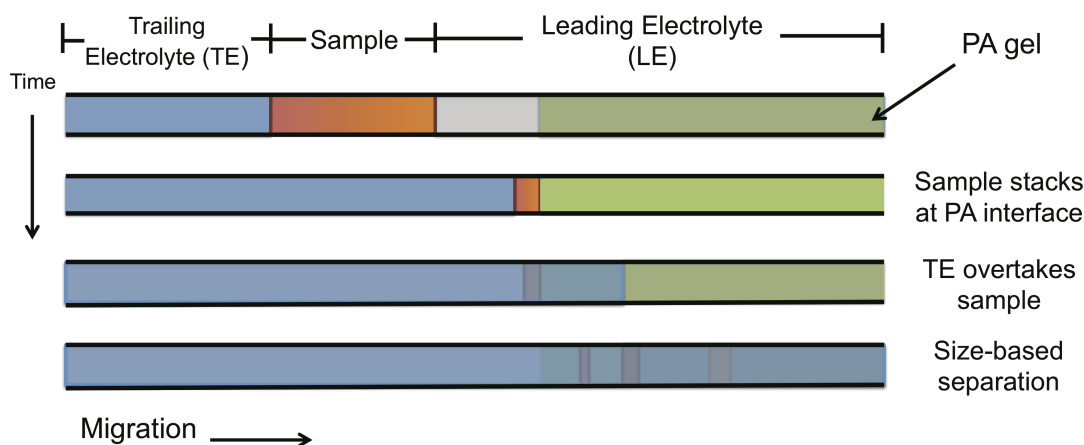size-based separation.

Figure 6.6: Schematic of transient isotachophoresis.

To characterize the sizing performance of the permanently-bonded PDMS microchan-
nels, we implemented a previously-reported tITP buffer system comprising a tris-HCl lead-
ing electrolyte and a tris-glycine trailing electrolyte. [3] We quantified separation and sizing
performance using a fluorescently-labeled BSA-OVA-TI protein ladder. First we fabricated
the device as in Figure 6.4B and loaded the protein ladder. Following electrophoretic in-
jection of the protein ladder into the free solution region of the microchannel, we removed
the protein ladder from the well and exchanged it for the trailing electrolyte (tris-glycine).
We then initiated the separation in constant current mode and observed the separation with
an epifluorescent microscope. After just 16 s, we fully separated all three protein ($R_s > 1$,
Figure 6.7). Further, we achieved the expected log-linear relationship between molecular
mass and migration distance (Figure 6.7). This separation performance is consistent with
previously-reported glass microchip separations, which resolved OVA and TI in a 3 mm
separation lane in under 60 s. [3] However, it should be noted that the polyacrylamide in
the glass chip separation included benzophenone to capture the proteins post-separation.
[3]. Interestingly, other PDMS-based microfluidic SDS-PAGE devices that did not use a
benzophenone treatment to reduce oxygen inhibition required a 25 mm long lane and a 2D
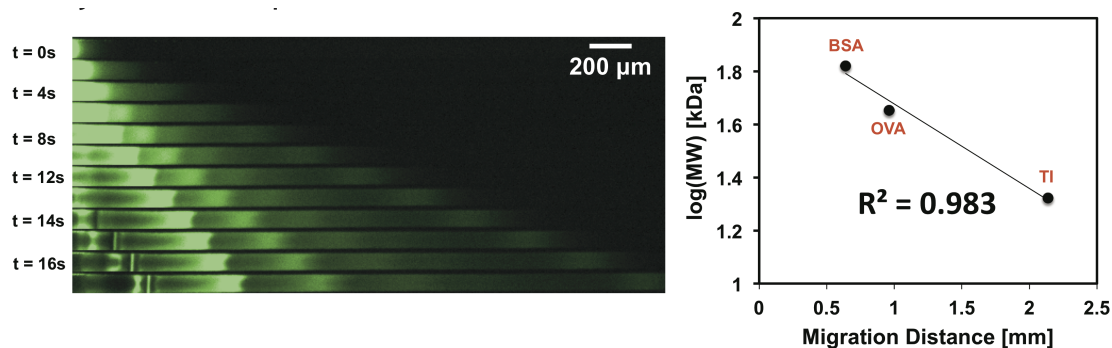separation to resolve a BSA-OVA-TI ladder. [10]

Figure 6.7: Protein sizing in PDMS microchannels. **(A)**A false-colored montage of a BSA-OVA-TI protein ladder SDS-PAGE separation in a PDMS microchannel. **(B)** Separated proteins exhibit the expected log-linear relationship bewtween molecular mass and electrophoretic mobility, enabling protein sizing.

6.3   Conclusion

Prototyping new device geometries is essential to adding new functionality to and improving the performance of microscale separations. However, since most devices are fabricated in glass, prototyping cycles take days due to long fabrication times. [4] Here we have presented a method for fabricating polyacrylamide gel electrophoresis devices in PDMS, which is amenable to rapid prototyping. We demonstrated PAGE separations in both permanently- and reversibly-bonded devices. The reversibly-bonded devices offer the advantage of sample access post-separation, potentially avoiding the challenges associated with introducing antibodies for immunoprobing along the separation axis. [3, 21] Further, we demonstrated protein sizing with tITP to preconcentrate the sample. Future work could implement alternative buffer systems optimized for low-molecular weight proteins, potentially further improving the separation performance. [21]

One potentially interesting application of fabricating polyacrylamide gels in PDMS microchannels is the ability to integrate the separation lane with the existing library of microfluidics devices. [5, 6] For example, one could design a chip with integrated sample preparation, separation, and quantification. By integrating all of the steps, losses could be reduced or accounted for, potentially enabling enabling absolute quantification of proteins from complex biological matrices.

Rapid fabrication and testing cycles are essential to developing and optimizing new designs. The method presented here reduces the fabrication cycle from days to hours, enabling faster prototyping. Additionally, integration with other types of microfluidic devices may enable new applications of high performance polyacrylamide-base separations.

References

1. Li, Y., Buch, J. S., Rosenberger, F., DeVoe, D. L. & Lee, C. S. Integration of Isoelectric Focusing with Parallel Sodium Dodecyl Sulfate Gel Electrophoresis for Multidimensional Protein Separations in a Plastic Microfludic Network. *Analytical Chemistry* **76,** 742–748 (Feb. 2004).

2. Tentori, A. M., Hughes, A. J. & Herr, A. E. Microchamber Integration Unifies Distinct Separation Modes for Two-Dimensional Electrophoresis. *Analytical Chemistry* **85,** 4538–4545 (May 2013).

3. Hughes, A. J. & Herr, A. E. Microfluidic Western blotting. . . . *of the National Academy of Sciences* (2012).

4. He, M. & Herr, A. E. Automated microfluidic protein immunoblotting. *Nature Protocols* **5,** 1844–1856 (Oct. 2010).

5. Nge, P. N., Rogers, C. I. & Woolley, A. T. Advances in Microfluidic Materials, Functions, Integration, and Applications. *Chemical Reviews,* 130214084124000 (Feb. 2013).

6. Sia, S. K. & Whitesides, G. M. Microfluidic devices fabricated in Poly(dimethylsiloxane) for biological studies. *ELECTROPHORESIS* **24,** 3563–3576 (Nov. 2003).

7. Dendukuri, D. *et al.* Modeling of Oxygen-Inhibited Free Radical Photopolymerization in a PDMS Microfluidic Device. *Macromolecules* **41,** 8547–8556 (Nov. 2008).

8. Appleyard, D. C., Chapin, S. C., Srinivas, R. L. & Doyle, P. S. Bar-coded hydrogel microparticles for protein detection: synthesis, assay and scanning. *Nature Protocols* **6,** 1761–1774 (Oct. 2011).

9. Choi, N. W. *et al.* Multiplexed Detection of mRNA Using Porosity-Tuned Hydrogel Microparticles. *Analytical Chemistry* **84,** 9370–9378 (Nov. 2012).

10. Shameli, S. M. & Ren, C. L. Microfluidic Two-Dimensional Separation of Proteins Combining Temperature Gradient Focusing and Sodium Dodecyl Sulfate-Polyacrylamide Gel Electrophoresis. *Analytical Chemistry* **87,** 3593–3597 (Apr. 2015).

11. Schneider, M. H., Tran, Y. & Tabeling, P. Benzophenone Absorption and Diffusion in Poly(dimethylsiloxane) and Its Role in Graft Photo-polymerization for Surface Modification. *Langmuir* **27,** 1232–1240 (Feb. 2011).

12. Schneider, M. H., Willaime, H., Tran, Y., Rezgui, F. & Tabeling, P. Wettability Patterning by UV-Initiated Graft Polymerization of Poly(acrylic acid) in Closed Microfluidic Systems of Complex Geometry. *Analytical Chemistry* **82,** 8848–8855 (Nov. 2010).

13. Simmons, C. S., Ribeiro, A. J. S. & Pruitt, B. L. Formation of composite polyacrylamide and silicone substrates for independent control of stiffness and strain. *Lab on a Chip* **13,** 646 (2013).

14. Hou, C. & Herr, A. E. Ultrashort Separation Length Homogeneous Electrophoretic Immunoassays Using On-Chip Discontinuous Polyacrylamide Gels. *Analytical Chemistry* **82,** 3343–3351 (Apr. 2010).

15. Chen, Q., Li, G., Nie, Y., Yao, S. & Zhao, J. Investigation and improvement of reversible microfluidic devices based on glass–PDMS–glass sandwich configuration. *Microfluidics and Nanofluidics* **16,** 83–90 (June 2013).

16. Chengjun Kang, R. C. N. D. S. The influence of surface grafting on the growth rate of polymer chains. *Polymer Chemistry* **7,** 302–309 (Dec. 2015).

17. Gharahdaghi, F., Weinberg, C. R., Meagher, D. A., Imai, B. S. & Mische, S. M. Mass spectrometric identification of proteins from silver-stained polyacrylamide gel: A method for the removal of silver ions to enhance sensitivity. *ELECTROPHORESIS* **20,** 601–605 (Mar. 1999).

18. Shevchenko, A., Wilm, M., Vorm, O. & Mann, M. Mass spectrometric sequencing of proteins silver-stained polyacrylamide gels. *Analytical Chemistry* **68,** 850–858 (Mar. 1996).

19. Giddings, J. C. *et al. Unified separation science* (Wiley New York etc, 1991).

20. Ornstein, L. & Davis, B. J. Disc electrophoresis. II. Method and application to human serum protein. *Ann NY Acad Sci* **121,** 404–427 (1964).

21. Gerver, R. E. & Herr, A. E. Microfluidic Western Blotting of Low-Molecular-Mass Proteins. *Analytical Chemistry* **86,** 10625–10632 (Nov. 2014).

Chapter 7

Conclusions and future directions

In this dissertation, we sought to develop tools to address the critical need for high selectivity single-cell protein analysis tools. We identified two key challenges in making high selectivity protein measurements in single cells: (1) chemical fixation induced artifacts in protein localization and (2) low antibody specificity. To address the first challenge, we developed a microscale subcellular fraction assay. We created a platform for assaying specific proteoforms without proteoform-specific antibodies by designing and characterizing the first reported single-cell isoelectric focusing assay.

An over arching theme in this work is the integration of multistage assays through fabrication. By integrating the sample preparation, separation, and detection into the same device, we obviated the need for lossy transfer steps, which enhances the sensitivity of our assay. In the case of the single-cell isoelectric focusing platform, we used precise patterning of chemistries to generate linear and stable pH gradients over a large area. Doing so, allowed for isoelectric focusing to be simultaneously performed over 50 microwells. Further, the development of new fabrication methods (e.g. self-indexed multistage photomasks) enabled us to integrate features without complex alignment steps.

Since IEF separation performance is closely linked to the shape of the pH gradient, future work should focus on developing scIEF devices with more robust pH gradients (e.g. reduced cathodic drift). One method to generate more robust pH gradients for IEF is through immobilized pH gradients (IPGs). [1] IPGs use weak acids and bases covalently linked into the polyacrylamide matrix (Immobilines) to generate pH gradients free of cathodic drift. [1] IPGs have been implemented in microchip electrophoresis, but have not yet been demonstrated for scIEF. [2] Since linear pH gradients can be generated with two opposing linear gradients in Immobilines concentration [1], we hypothesize IPGs suitable for scIEF could be fabricated using a microfluidic gradient generator. [3, 4] Immobilized pH gradients for the scIEF platform will further improve the robustness of the pH gradients.

One intriguing area of future development is the mapping of protein measurements back to the original cellular microenvironment. Current tools require the dissociation of cells from the niche and thus it is impossible to know the precise context from which the cell originated. Developing tools that allow researchers to map downstream biochemical analyses back to

specific microenvironments or ideally locations in a tissue will strengthen our understanding of the role that microenvironment plays in cellular function.

Given that the platforms developed in this dissertation are all endpoint measurements, a yet unmet analytical measurement gap is the longitudinal measurement of proteins. While fluorescent fusion proteins can be used for longitudinal measurements of protein localization and expression, they are limited by low multiplexing (1-2 targets) and tagging-induced mislocalization. [5, 6] I hypothesize that molecular recording could be used record transient events that can then be read out by the types of selective single-cell protein separations developed in this dissertation. In a similar manner to how synthetic scaffolds have been used to study phosphorylation in cellular signaling [7] or DNA probes that have been used to record transient protein-protein interactions [8], probes that can be altered upon detection of a protein target of interest may be designed. The probes for different targets could be designed be separable by size or charge, giving rise to high degrees of multiplexing. Since the probes could be designed with the separation in mind, the multiplexing could approach the theoretical peak capacity. Molecular recording with a separation-based readout may enable highly-multiplexed, longitudinal measurements of protein expression.

As our measurement tools become more sophisticated, so can the questions we ask. Single cell analysis has advanced enough to allow quantitative measurement of DNA, RNA, or protein from single cells. The rise of "multi-omic" single-cell analysis tools and more tailored statistical methods will enhance our understanding of how cells transduce signals and make decisions. These insights will undoubtedly help us to better understand ourselves and will lead to discoveries that improve our quality of life.

References

1. Bjellqvist, B. *et al.* Isoelectric focusing in immobilized pH gradients: principle, methodology and some applications. *Journal of biochemical and biophysical methods* **6,** 317–339 (Sept. 1982).

2. Sommer, G. J., Singh, A. K. & Hatch, A. V. On-chip isoelectric focusing using photopolymerized immobilized pH gradients. *Analytical Chemistry* **80,** 3327–3333 (May 2008).

3. Gao, Y., Sun, J., Lin, W.-H., Webb, D. J. & Li, D. A compact microfluidic gradient generator using passive pumping. *Microfluidics and Nanofluidics* **12,** 887–895 (Dec. 2011).

4. Burdick, J. A., Khademhosseini, A. & Langer, R. Fabrication of Gradient Hydrogels Using a Microfluidics/Photopolymerization Process. *Langmuir* **20,** 5153–5156 (June 2004).

5. Schnell, U. U., Dijk, F. F., Sjollema, K. A. K. & Giepmans, B. N. G. B. Immunolabeling artifacts and the need for live-cell imaging. *Nature Methods* **9,** 152–158 (Jan. 2012).

6. Stadler, C. *et al.* Immunofluorescence and fluorescent-protein tagging show high correlation for protein localization in mammalian cells. *Nature Methods* **10,** 315–323 (Feb. 2013).

7. Gordley, R. M. *et al.* Engineering dynamical control of cell fate switching using synthetic phospho-regulons. *Proceedings of the National Academy of Sciences of the United States of America* **113,** 13528–13533 (Nov. 2016).

8. You, M. *et al.* DNA probes for monitoring dynamic and transient molecular encounters on live cell membranes. *Nature Nanotechnology* **12,** 453–459 (Mar. 2017).